Universidad de Concepción

Dirección de Postgrado

Facultad de Ciencias Químicas

Programa Doctorado en Ciencias Geológicas

Control geológico en el tamaño y recurrencia de grandes terremotos de subducción en Chile

(Geological control on the size and recurrence of great megathrust earthquakes in Chile)

Tesis para optar al grado de Doctor en Ciencias Geológicas

JOAQUÍN IGNACIO JULVE LILLO

CONCEPCIÓN-CHILE

2024

Profesor Guía: Dr. Marcos Moreno Switt

Profesor Co-guía: Dr. Andrés Tassara Oddo

Dpto. de Ciencias de la Tierra, Facultad de Ciencias Químicas

Universidad de Concepción

Agradecimientos

El resultado de este trabajo no hubiese sido posible sin el apoyo incondicional de mi familia. El camino hacia el desarrollo exitoso de este proyecto de tesis no estuvo exento de altos y bajos, tanto académicos como personales. Por esta razón, las incontables veces en que mis padres y hermano estuvieron junto a mí para brindarme apoyo fueron fundamentales para empujar mi trabajo hacia buen puerto, situación por la que estaré eternamente dichoso.

Por otra parte, quisiera agradecer al financiamiento otorgado por el Núcleo Milenio CYCLO y el Proyecto Anillo Precursor, con los cuales fue posible desarrollar campañas de terreno relacionadas con temas afines a este proyecto de investigación, y por cierto para poder publicar mi trabajo en congresos nacionales e internacionales y en importantes revistas científicas.

Agradezco particularmente la ayuda del Dr. Sylvain Barbot (University of Southern California) por su apoyo y enseñanza en la implementación de modelos numéricos aplicados al margen de subducción chileno. Su ayuda fue fundamental para desarrollar exitosamente mi proyecto de tesis y para entender las geociencias desde otra perspectiva. Además, la integración de estas nuevas metodologías a problemas aplicables en Chile ocurrió gracias a la plena confianza y apoyo de mi profesor guía Dr. Marcos Moreno, quien me otorgó la posibilidad de expandir mi conocimiento y adentrarme en el mundo del ciclo sísmico en zonas de subducción. Su criterio y punto de vista fueron muy importantes para encausar mi trabajo y aprovechar todo su potencial. También agradezco a mi profesor co-guía Dr. Andrés Tassara, quien siempre tuvo la disposición y cercanía no solo para aconsejarme acerca del desarrollo de mi proyecto, sino que también para otorgar su sabia opinión en momentos complejos.

Por otra parte, quiero agradecer a la sección 4.1 del Centro de Investigación en Geociencias de Alemania (GFZ), dirigida por el Dr. Claudio Faccenna. Los meses que estuve ahí significaron un enorme crecimiento no sólo como científico, sino que también como persona. Fue una experiencia inolvidable en la que pude reencontrarme

con la geología y me permitió aplicar diferentes conceptos a mi trabajo de investigación. La visión de cada uno de los investigadores y estudiantes de la sección fueron un aporte muy valioso en el desarrollo de este trabajo, y la forma en que se desarrolla la ciencia en ese instituto es algo que sin dudas aplicaré en mi futuro como investigador.

Finalmente agradezco a todos los colaboradores que aportaron dando su punto de vista ya sea metodológico o teórico respecto de lo desarrollado en esta investigación, el Dr. Rodolfo Araya, Dr. Jorge Crempien, Dr. Nicole Catalán y PhD(c) Valeria Becerra-Carreño, y de forma especial, a todas mis amigas y amigos que con su compañía me levantaron en los momentos difíciles y rieron conmigo en las pocas ocasiones de ocio que este doctorado me pudo ofrecer.

Joaquín Julve, 5 de agosto de 2024

Resumen

Las zonas de subducción son límites de placas convergentes caracterizadas por la subducción de una placa menos boyante bajo un cuerpo continental (u oceánico) más ligero. Este proceso define una gigantesca falla de corrimiento llamada *megathrust*, que alberga la mayoría de la sismicidad mundial. La predicción de la sismicidad en esta interfaz ha sido objeto de debate durante décadas, principalmente porque los factores que controlan los procesos geodinámicos que culminan en un terremoto están ocultos por una gruesa capa de roca, lo que hace que el acceso directo a la interfaz entre ambas placas sea actualmente imposible.

En las últimas décadas, se han realizado esfuerzos significativos para relacionar la deformación superficial observada mediante conjuntos de datos GNSS e InSAR con las rupturas del *megathrust* que han sido registradas por la sismología moderna. Varios estudios han asociado señales específicas de deformación con etapas particulares del ciclo sísmico –que es un proceso centenario o decenal de nucleación de terremotos– asumiendo que algunas regiones de la interfaz de la placa permanecen acopladas, almacenando estrés y produciendo un déficit de deslizamiento que eventualmente se libera durante un terremoto. Sin embargo, a partir de la utilización de sofisticados modelos numéricos y cinemáticos, trabajos recientes han demostrado que el proceso completo de acumulación y liberación de estrés es más complejo de lo que se pensaba anteriormente, involucrando deformación postsísmica explicada por procesos viscoelásticos o poroelásticos.

Por otra parte, observaciones geológicas indican que el *megathrust* es una amplia zona de falla que involucra deformación métrica a kilométrica, donde diversas litologías interactúan para desarrollar diferentes mecanismos de deslizamiento, desde desplazamiento asísmicos hasta deslizamientos lentos y eventos sísmicos. Estos mecanismos también han sido registrados procesando series temporales de GNSS en diferentes zonas de subducción en todo el mundo. Las señales de estos mecanismos de deslizamiento están impresas en la estructura de la roca de afloramientos de paleo zonas de subducción, revelando que la sismicidad del *megathrust* involucra

interacciones fluido-roca siguiendo episodios de *brittle-creep* y *pressure-solution creep*. Estas interacciones generan microestructuras características dentro de la zona dañada, aumentando la complejidad del sistema y, en última instancia, desencadenando un terremoto.

En este marco, este trabajo desentraña el papel de los parámetros clave que afectan el ciclo sísmico de los terremotos en el megathrust. Utilizando modelos numéricos cuasi-dinámicos restringidos por información geológica y geofísica, estudiamos el ciclo sísmico a lo largo de la zona de subducción chilena. Nuestros primeros resultados indican que la estructura geológica, manifestada en la distribución de los parámetros de fricción a lo largo del megathrust, puede explicar la sismicidad, los tiempos de recurrencia y el tamaño de las rupturas registradas en el sur de Chile. Estos hallazgos destacan un aspecto clave del proceso de nucleación de rupturas en las zonas de subducción: los minerales deformados en la interfaz de la placa controlarán el tipo de ruptura que puede desarrollar el ciclo sísmico en el megathrust. A partir de esta idea principal, se infiere que la temperatura y la presión, ambas controlando las reacciones de metamorfismo prógrado en la interfaz entre ambas placas, también tendrán un impacto en la sismicidad al cambiar la estabilidad de ciertos minerales con la profundidad. Además, dado que el esfuerzo normal efectivo en la falla de subducción depende de la razón de presión de poros, la presencia de fluidos influye enormemente en el ciclo sísmico en las zonas de subducción. Nuestros resultados finales muestran que el estado hidráulico medio en la interfaz de la placa, controlado por la porosidad de la falla y la disponibilidad de fluidos, puede permitir la propagación de rupturas o disminuir el tiempo de recurrencia de rupturas específicas en áreas donde la presión de poros está cerca de la litostática, y favorecer secuencias de rupturas pequeñas y en cascada de en regiones donde no se observan fluidos. Estas características destacan las interacciones fluido-roca como un aspecto crucial del ciclo sísmico en las zonas de subducción, mejorando significativamente las evaluaciones de peligrosidad sísmica a lo largo del margen chileno.

Abstract

Subduction zones are convergent plate boundaries characterized by the subduction of a less buoyant plate beneath a lighter continental or oceanic body. This process delineates a massive thrust fault called the megathrust, which hosts most of the seismicity worldwide. The forecasting of seismicity at this interface has been debated for decades, primarily because the governing factors controlling the geodynamic processes that culminate in an earthquake are obscured by a thick layer of rock, making direct access to the megathrust currently impossible.

In recent decades, significant efforts have been made to relate surface deformation observed by GNSS and InSAR datasets with megathrust ruptures recorded by modern seismology. Several studies have associated specific deformation signals with particular stages of the seismic cycle—a centennial or decennial process of earthquake nucleation—assuming that some regions of the plate interface remain coupled, storing stress and producing a slip deficit that is eventually released during an earthquake. However, using sophisticated numerical or kinematic approaches, recent works have shown that the entire process of stress accumulation and release is more complex than previously thought, involving postseismic deformation explained by viscoelastic or poroelastic processes.

Geological observations indicate that the megathrust is a broad fault zone involving deformation over meters to kilometers, where various lithologies interact to develop different slip mechanisms, from aseismic slip to slow-slip and seismic events. These mechanisms have also been registered by processing GNSS time-series at different subduction zones worldwide. The signals of these slip mechanisms are imprinted in the rock fabric of paleo-subduction zone outcrops, revealing that megathrust seismicity involves fluid-rock interactions following episodes of brittle-creep and pressure-solution creep. These interactions generate characteristic microstructures within the damaged zone, increasing the system's complexity and ultimately triggering an earthquake.

In this framework, this work unravels the role of key parameters affecting the seismic cycle of megathrust earthquakes. By using quasi-dynamic numerical models

constrained by geological and geophysical information, we study the seismic cycle along the Chilean subduction zone. Our initial results indicate that the geological structure, as manifested in the distribution of frictional parameters along the megathrust, can explain the seismicity, recurrence times, and size of the ruptures recorded in Southern Chile. These findings highlight a key aspect of the rupture nucleation process at subduction zones: the minerals deformed at the plate interface will control the type of rupture that the seismic cycle at the megathrust may develop. From this main idea, it is inferred that temperature and pressure, both of which control prograde metamorphic reactions at the plate interface, will also impact the seismicity by changing the stability of certain minerals with depth. Moreover, since the effective normal stress at the subduction fault depends on the pore pressure ratio, the presence of fluids greatly influences the seismic cycle at subduction zones. Our final results show that the mean hydraulic state at the plate interface, controlled by fault porosity and fluid availability, may allow rupture propagation or decrease the recurrence time of specific ruptures in areas where the pore pressure is close to lithostatic, or favor small and cascading rupture sequences otherwise. These features highlight fluid-rock interactions as a crucial aspect of the seismic cycle at subduction zones, significantly enhancing seismic hazard assessments along the Chilean margin.

Index

Chapter	**1.**	**Introduction**	13
	1.1.	Subduction zones and their frictional behavior	13
	1.2.	Subduction zone seismic cycle and governing factors	17
	1.3.	The Chilean case	21
	1.4.	Scientific problem, hypothesis, and objectives	24
	1.5.	Thesis overview	25
	1.6.	Methods (summary)	26
		1.6.1. Numerical models	26
Chapter	**2.**	**Recurrence time and size of Chilean earthquakes influenced by geological structure (Article 1)**	30
	2.1.	Introduction	31
	2.2.	Modelling the subduction seismic cycle of the southern Andes	34
	2.3.	Earthquake cycle observations	37
	2.4.	Mechanics and surface deformation of simulated earthquakes	38
	2.5.	Subduction cycle at the Valdivia segment	43
	2.6.	Methods	45
		2.6.1. Fault friction and mantle viscosity	45
		2.6.2. Temperature model	48
		2.6.3. Pressure and temperature path	50
		2.6.4. Coseismic slip model	51
Chapter	**3.**	**Impact of upper-plate faulting on foreshocks: Insights from the 2014 Iquique earthquake (Article 2)**	53
	3.1.	Introduction	54
	3.2.	Data and methods	56
		3.2.1. Modeling upper-plate fault and megathrust earthquake cycles	56
	3.3.	Results	60
		3.3.1. Slip mechanisms	60
		3.3.2. Surface deformation	63
		3.3.3. Precursory activity and changes in effective normal stress	65
	3.4.	Conclusions	67
Chapter	**4.**	**Discussion**	69
	4.1.	Geological control over the seismic cycle at the Chilean subduction zone	69
	4.2.	The effect of effective normal stress	77
Chapter	**5.**	**Conclusions**	83

Chapter 6. Appendix 84
6.1. Supplementary Material Chapter 2 84
6.2. Supplementary Material Chapter 3 91
6.2.1. Modeling upper-plate fault and megathrust earthquake cycles (S1) 92
6.2.2. Geological and geophysical information (S2) 93
6.2.3. Stress to strain interactions (S3) 96
6.2.4. Thermal model (S4) 97
6.2.5. Compute of surface deformation (S5) 98
6.2.6. Supplementary Figures 999
6.2.7. Supplementary Tables 101
6.2.8. Supplementary References 101
6.3. Supplementary Material of the Thesis 107
Chapter 7. Main references 119
7.1. Thesis references 119
7.2. References of Chapter 2 (Main article) 129
7.3. References of Chapter 2 (Methods) 135
7.4. References of Chapter 3 137

Index of figures

Chapter 1. Introduction
Figure 1.1. World seismicity map 14
Figure 1.2. Shear stress evolution with time 16
Figure 1.3. Conceptual model of a subduction system and its evolution with time 18
Figure 1.4. Serpentinization front and plate interface below the continental Moho 19
Figure 1.5. Tectonic and seismic overview of the Chilean subduction zone 24
Chapter 2. Recurrence time and size of Chilean earthquakes influenced by geological structure (Article 1)
Figure 2.1. Tectonic setting of the Southern Chile Subduction Zone 32
Figure 2.2. Summary of data acquired and set-up of the model 33
Figure 2.3. Fault dynamics and recurrence times at the SCSZ 40
Figure 2.4. Upper crust deformation 42

		Figure 2.5.	Conceptual model of the SCSZ integrating insights from quasi dynamic simulations and compiled data	44
Chapter	**3.**	**Impact of upper-plate faulting on foreshocks: Insights from the 2014 Iquique earthquake (Article 2)**		
		Figure 3.1.	Tectonic setting, model structure, and forearc features	59
		Figure 3.2.	Slip-rate over time and rupture style over 1500 years of seismic cycle	62
		Figure 3.3.	GNSS data and kinematic coseismic slip model of Iquique earthquake, against models results	64
		Figure 3.4.	Foreshock seismicity and conceptual model	66
Chapter	**4.**	**Discussion**		
		Figure 4.1.	Frictional properties of relevant minerals over R_u values at Southern and Northern Chile	71
		Figure 4.2.	Different simulations of the seismic cycle at Southern Chile by changing $a - b$	73
		Figure 4.3.	Different simulations of the seismic cycle at Northern Chile by changing $a - b$	74
		Figure 4.4.	Spectrum of slip mechanisms with changes in $a - b$ for Southern Chile	75
		Figure 4.5.	Spectrum of slip mechanisms with changes in $a - b$ for Northern Chile	76
		Figure 4.6.	Seismic cycle simulations by changing λ distributions at Southern and Northern Chile	78
		Figure 4.7.	Spectrum of slip mechanisms with induced perturbation of $\overline{\sigma_n}$ at Northern and Southern Chile	79
		Figure 4.8.	Final conceptual model of the subduction system at Southern and Northern Chile	80
Chapter	**6.**	**Appendix**		
		Figure 6.1.	Temperature distribution, mesh, and pressure-temperature path	85
		Figure 6.2.	GNSS and intertidal biotic indicator data	86
		Figure 6.3.	Root mean squared error values for systematic variation on λ	87
		Figure 6.4.	Effects of petrology and depth of the end of the seismogenic zone	88
		Figure 6.5.	Time series of the east and vertical components of synthetic GPS from our model	89

Figure 6.6. Mesh of the quasi-dynamic modeling 98
Figure 6.7. Mesh of the thermal model and temperature distribution at 20°S 98
Figure 6.8. Distribution of effective normal stress along the dip of the megathrust as a result of changes in λ 99
Figure 6.9. Effective normal stress, temperature and seismicity distribution in Northern and Southern Chile 116
Figure 6.10. Effective normal stress, temperature and seismicity distribution in Northern and Southern Chile, as a result of λ perturbation 117

Index of tables

Chapter 2. Recurrence time and size of Chilean earthquakes influenced by geological structure (Article 1)
Table 2.1. Frictional parameters of the preferred and initial models 37
Chapter 6. Appendix
Table 6.1. Power-creep law properties 83
Table 6.2. Pore pressure ratio and effective normal stress variation 84
Table 6.3. Thermal properties of the temperature model 84
Table 6.4. Power-creep law parameters of equations (1), (2), and (7) 100
Table 6.5. Frictional properties of the slip-rate- and state- friction law at the megathrust and the offshore upper-plate fault (Offshore UPF). 100
Table 6.6. Compilation of frictional properties on minerals 106
Table 6.7. Frictional properties used on each simulation at Southern Chile 110
Table 6.8. Frictional properties used on each simulation at Southern Chile 113

1 Introduction

1.1 Subduction zones and their frictional behavior

Subduction zones are convergent tectonic boundaries where two plates of different densities collide, delineating a massive thrust fault—hereafter referred to as the megathrust—which hosts most of the world's seismicity (Fig. 1.1). As the denser plate sinks beneath the lighter one, the megathrust generates friction at the plate interface, causing slip to occur through different mechanisms and at varying rates, ranging from steady and transient aseismic slip in creeping regions and resulting from postseismic relaxation or spontaneous slip events respectively, to stick-slip behavior in coupled areas (Avouac, 2015; Bürgmann, 2018). Over the last decades, several studies have proposed that slip-rate complexity at subduction zones results from the state of shear and normal stresses controlling the megathrust's frictional regime (Luo & Liu, 2021; Saito & Noda, 2023; Tong & Lavier, 2018). Greater efforts have been made to study, under laboratory conditions, the response of different minerals to the stresses likely developed at subduction zones, demonstrating that empirical laws may explain part of the slip behavior observed during and before earthquakes (Marone, 1998; Marone et al., 1990).

Within this framework, slip rate–and–state friction laws (SRSF) (Barbot, 2019a; Dieterich, 1979; Rice, 1993; Rubin & Ampuero, 2005; Ruina, 1983) arise as empirical expressions in which the shear stress (τ) is understood as a function of a reference coefficient of friction (μ_0) at a reference velocity (V_0), of a state parameter that allows healing at stationary contacts between grain minerals (θ), of a critical distance of slip at which the steady state is recovered (L), of the effective normal stress ($\overline{\sigma_n}$), and of two parameters that are dependent on the material being deformed, the direct (a) and evolutionary (b) effects (Collettini et al., 2011). By invoking different evolution laws that update the state of the system with each slip-step (e.g. Dieterich, 1979; Ruina, 1983) and using constitutive behaviors from rock deformation to update the way in which these paremeters are related (e.g. Barbot, 2019a; Dieterich, 1979; Lapusta et al., 2000), several works have used these laws to explain the varying aspects of the slip

behavior during faulting. Accompanied by the outstanding development in numerical models that solve the fundamental equations of continuum mechanics (e.g. Barbot, 2018b, 2018a; Barbot et al., 2017; Dal Zilio et al., 2022; Dal Zilio & Gerya, 2022; Dal Zilio et al., 2022; Lapusta et al., 2000; Lapusta & Liu, 2009), the use of SRSF laws has allowed for the simulation of slip evolution at fault surfaces, increasing our understanding of rupture processes and earthquake nucleation.

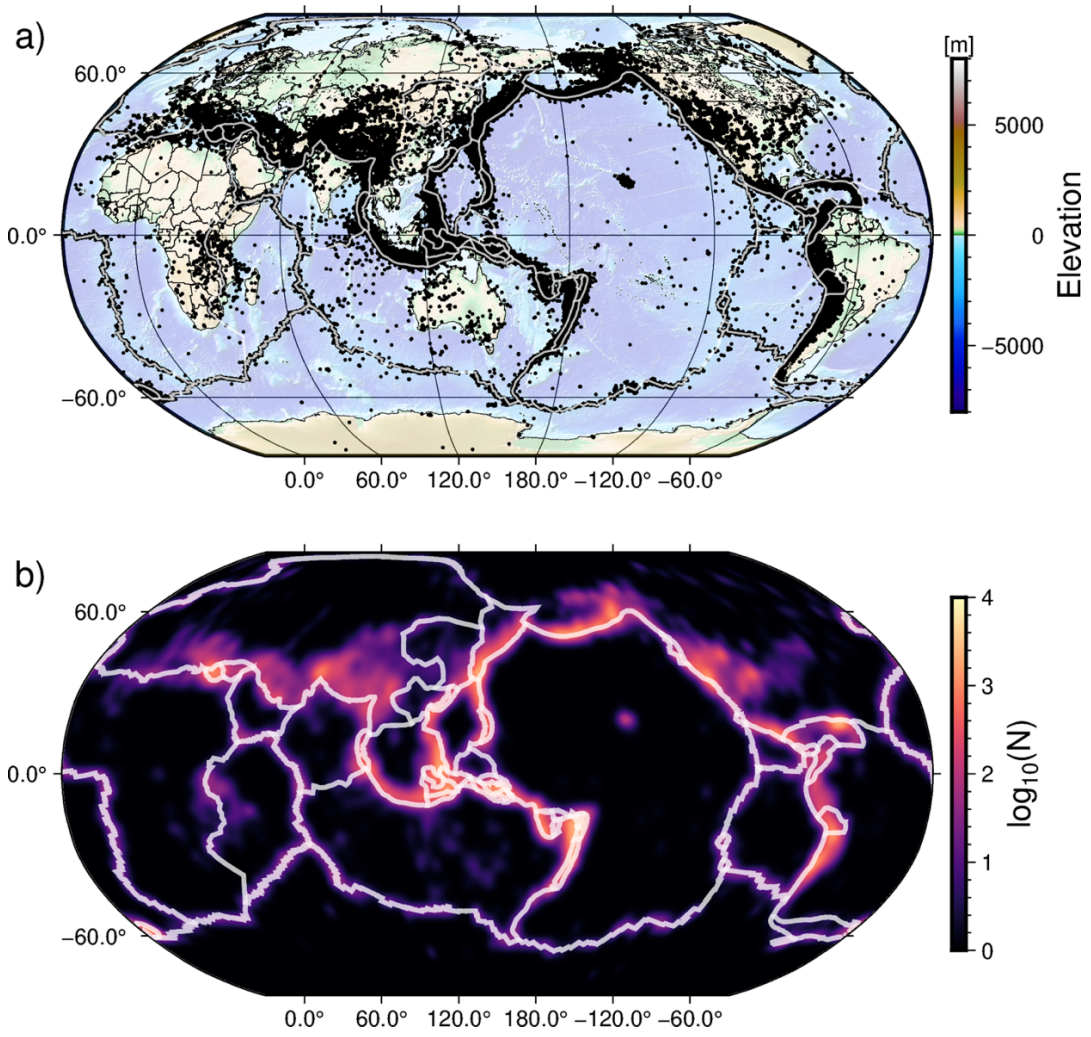

Fig. 1.1. World seismicity map. a) Map showing the world seismicity of the USGS catalogue between 2008 and 2024 for events with moment of magnitude (Mw) greater than 3 (black dots). White lines represent plate boundaries. Elevation data was obtained from Tozer et al. (2019) and correspond to the Global Bathymetry and Topography at 15 Arc Sec: SRTM 15+. b) Is the log_{10} of the number (N) of events within blocks of 200 m. The grid was obtained using the same data as in a) and the *blockmean* function of GMT6 (Wessel et al., 2019). White lines represent plate boundaries. In both panels, seismicity is highly concentrated at plate boundaries, and specifically at subduction zones.

Particularly, Barbot (2019a) proposed a multiplicative formulation of the SRSF law:

$$\tau = \overline{\sigma_n}\mu_0 \left(\frac{V}{V_0}\right)^{\frac{a}{\mu_0}} \left(\frac{\theta V_0}{L}\right)^{\frac{b}{\mu_0}} \qquad \text{eq. 1.1}$$

which comes from a constitutive model assuming that fault strength is controlled by the asperities that support the load at the microscopic level, under isothermal and isobaric conditions (Barbot 2019a). The state parameter (θ), is the same as in the formulation of Dieterich (1979):

$$\dot{\theta} = 1 - \frac{\theta V}{L} \qquad \text{eq. 1.2}$$

where the dot denotes a derivative over time, meaning that changes in θ will be controlled by the evolution of V as a response to steps in slip at a certain value of τ. Such characteristic gives an aging component to eq. 1.1, resulting in a spontaneous healing of the fault surface delineated by eq. 1.2 (Dieterich, 1979).

Fig. 1.2 shows a simulated behavior of τ using eq. 1.1 and assuming typical values of $\overline{\sigma_n}$ (50 MPa), μ_0 (0.6), V_0 (1x10^{-6} m/s), L (1x10^{-2} m), a (1x10^{-2}, 2x10^{-2}), and b (2x10^{-2}, 1x10^{-2}). Under laboratory conditions, τ_{ss} (shear stress at steady state) evolves with changes in V. In a simple experiment (Fig. 1.2), a sudden increase in V, mimicking what happens during an earthquake, will generate an immediate response in τ_{ss} reaching a new maximum value (τ_{MAX}). Then, at the new value of V, τ_{ss} will slowly decrease down to the next steady state (Fig. 1.2). The time it takes to transition from τ_{ss1} to τ_{ss2} depends on the value of L, which control the slip required for the fault to reach a new steady state. If $\tau_{ss1} > \tau_{ss2}$ then the increase in V will decrease the fault's strength, indicating a velocity weakening regime ($a - b < 0$), which allows stick-slip behavior and thus provokes earthquake nucleation (Fig. 1.2a). Conversely, if $\tau_{ss1} < \tau_{ss2}$, then the increase in V will increase the fault's strength, indicating a velocity strengthening behavior ($a - b > 0$), where slip will be aseismic (Fig. 1.2b).

Nevertheless, velocity strengthening domains may allow rupture propagation. Considering a fault whose friction is governed by a RSF law, Scholz (1998) shows that

Hopf bifurcations arise at a critical value of $\overline{\sigma_n}$, where the system becomes conditionally stable. A Hopf bifurcation occurs when a system's equilibrium loses stability as parameters vary ($\overline{\sigma_n}$ in this case), leading to periodic solutions or oscillations of the slip-rate with time. In this state, ruptures can propagate if the velocity jump of the earthquake is high enough to overcome the critical value of $\overline{\sigma_n}$, leading to instability.

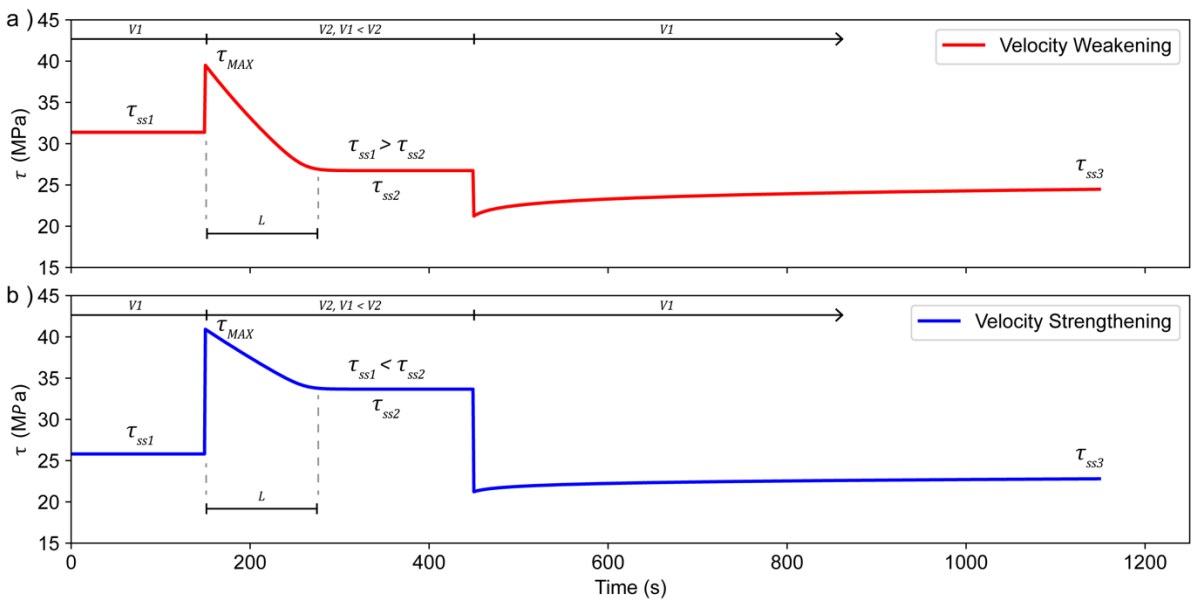

Figure 1.2. Shear stress evolution with time. a) Shear stress evolution under a velocity weakening domain. τ_{ss1} and τ_{ss2} are the first and second values of shear stress at steady state. L is the characteristic slip distance. $V1$ and $V2$ are the two values of velocity. b) Same as a) but under a velocity strengthening regime.

The evolution of slip-rate with time has been observed in different fault gouges (den Hartog et al., 2012; Moore & Lockner, 2008, 2011; Saffer & Marone, 2003; Sawai et al., 2016, 2017; Tembe et al., 2010), allowing an explanation of various slip mechanisms identified in faults. In subduction zones, Scholz (1998) proposed that the megathrust is divided into different frictional segments where SRSF properties vary with depth. The $a - b$ value seems to play a significant role in the definition of the seismogenic zone, which is where most of the seismicity is located (Fig. 1.3a). Over the last decades, geophysical monitoring via GNSS and seismic instrumentation has led to multiple observations of seismicity within the seismogenic zone and associated surface deformation. Using this data, kinematic models incorporating up-to-date

inversion methodologies have partially illuminated the heterogeneities in slip behavior at the megathrust, concluding that earthquake occurrence is a response to a cyclic process.

1.2 Subduction zone seismic cycle and governing factors

After the 1906 San Francisco earthquake, Harry Fielding Reid (1910) proposed that earthquake triggering results from surpassing the strain energy that rocks on either side of a fault can store, a statement known as the elastic rebound theory. With the development of GNSS techniques, we now know that Reid's hypothesis was correct, but we also understand that the entire process is much more complex than merely storing and releasing strain energy. At any given fault, the whole process of storage and release of strain energy after stress accumulation is known as the seismic cycle, whose understanding is key to unraveling earthquake dynamics and forecasting. If we examine the behavior of τ at the megathrust over time (Fig. 1.3b), we observe that there is no infinite build-up. Instead, a cyclic process of progressive increase, sudden peak, and decrease occurs. The period of constant increase of τ is known as the interseismic phase, that last until the stress overcome the yielding limit of the fault. In that point, a dislocation during the coseismic stage occurs, releasing as slip and elastic deformation the stress accumulated previously. In terms of τ, it is characterized by stress drop ($\Delta\tau$) at the same time as the peak in V occur (Fig. 1.3c). After the decrease, the system quickly reaches a new value of τ_{SS} and starts to accumulate τ and thus strain energy once again. Conversely, V takes years to decrease back to the background value (Fig. 1.3c). This stage is named the postseismic phase and is characterized by afterslip and anelastic deformation (e.g. J. P. Avouac, 2015; Hu et al., 2004; H. Luo & Wang, 2021; Massonnet et al., 1996; Wang et al., 2007). Within this context, any increase in V, from slow-slip up to earthquake triggering, can be understood as a dislocation on the seismogenic zone that will release elastic deformation due to stress accumulation and a consequent amount of slip.

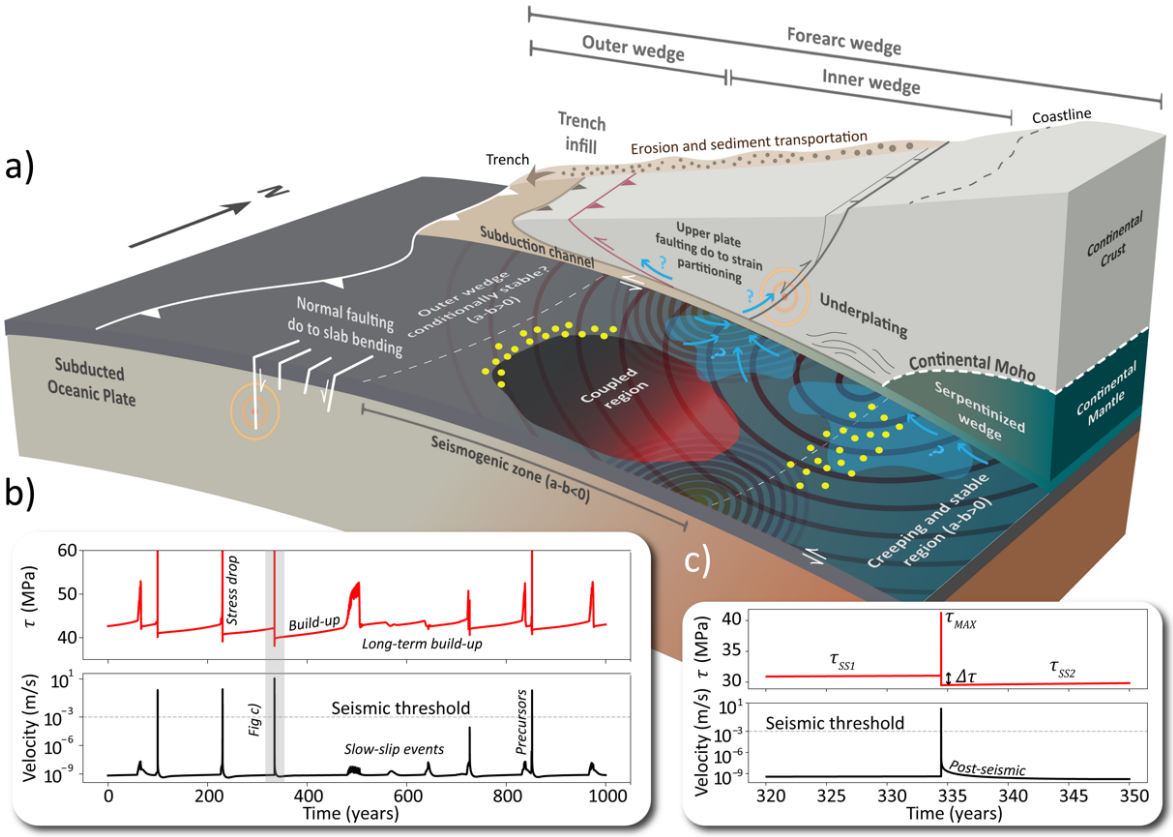

Figure 1.3. Conceptual model of a subduction system and its evolution with time. a) Shows the primary aspects that control the dynamics of the megathrust slip-rate at subduction zones. Yellow dots mark seismicity, light blue areas represent fluid distribution at the plate interface, light blue arrows are the fluid path, green colors in the continental plate and the megathrust plane denote serpentinization, concentric circles show earthquake ruptures. b) τ and V over time using eq. 1.1 and 1.2. c) Snapshot in between 320 and 350 years in b).

The evolution of τ and V (Fig. 1.3b) shows that there is no permanent periodicity in earthquake recurrence, but rather a spectrum of different slip-rates and slip mechanisms over time. While it is true that after an earthquake a new event will develop in the years to come, to predict the exact time is not possible due to the complexity of τ evolution in time, imprinting a chaotic nature to the seismic cycle. An example of this is the long-term processes of stress accumulation that may arise from the occurrence of slow-slip events (Fig. 1.3b), or the observations of earthquakes with different size at the same subduction zone (Moreno et al., 2018; Saffer & Wallace, 2015; Wallace, 2020).

The variance that arises from the theoretical framework has also been observed in several subduction zones worldwide. Kinematic models that explain surface deformation registered by GNSS data show that there are coupled regions (Fig. 1.3a) where the megathrust slips below the convergence velocity or experiences no slip at all (Scholz & Campos, 2012). It is in these areas where stress accumulation occurs, generating seismicity in the surroundings (Schurr et al., 2020) and slip deficit as a function of the stress stored (Kaneko & Fialko, 2011; Lindsey et al., 2021). Coupled regions are not homogeneous features within the megathrust (Behr & Bürgmann, 2021; Bürgmann, 2018; Scholz & Campos, 2012). Recent works have shown that there are parts of the plate interface that creep at the same velocity as the convergence rate between both plates, generating aseismic and seismic regions. If we assume that slip-rate is controlled by the stresses at the fault, the materials being deformed, and the temperature distribution, then it is likely that megathrust seismicity is strongly dependent on the geological and rheological structure at subduction zones.

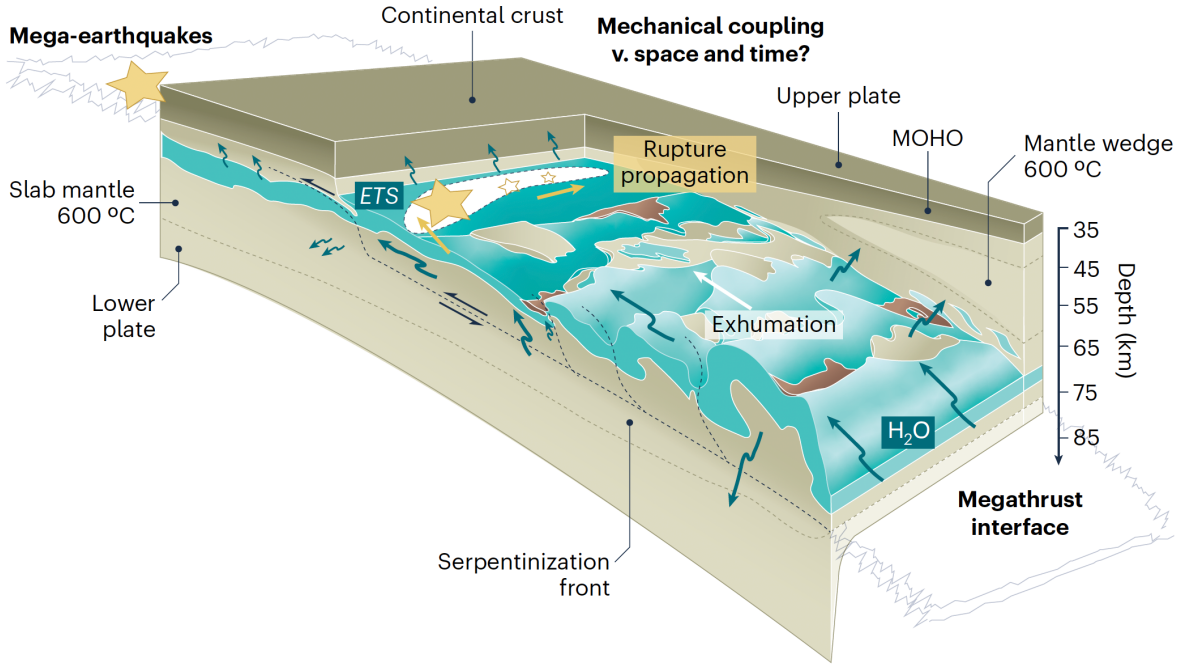

Figure 1.4. Serpentinization front and plate interface below the Continental Moho. ETS=Episodic Tremor and Slip. Blue arrows represent fluid pathways. Yellow stars are earthquake rupture. Figure obtained from Chlieh (2024).

These dynamic environments are primarily controlled by tectonic forces, but where surface erosion, which is mainly regulated by climate conditions, plays a critical role in feeding the plate interface with sediments, changing the materials that will be subducting and thus developing what nowadays is known as the subduction channel (Fig. 1.3a) (von Huene & Scholl, 1991). Larger sediment layers will have a strong impact on the friction at the megathrust, controlling the slip-rates during the seismic cycle. Moreover, a and b values will also change as a function of the percentage of phyllosilicates within the sediments being subducted, modulating the slip-rate at depth. Recently, it has been discovered that a and b have a temperature dependency (Barbot, 2022 and reference therein). Since thermal regimes at the megathrust depend on the age of the subducted plate, the convergence velocity between both plates, and the hydraulic state at the plate interface, and none of those properties remain constant along strike, slip-rate heterogeneities imprinted by these variances will arise.

Minerals conforming the rocks of the subducted and overriding plate, along with sediments at the subduction channel, experience changes on its inner structure due to the instabilities generated by the increase in temperature and pressure with depth. This process is known as prograde metamorphism and will impact both, the a and b values (Sawai et al., 2016, 2017), and the $\overline{\sigma_n}$ because of progressive fluid release within the plate interface and overriding plate (Fig. 1.3a, Fig. 1.4) (Angiboust et al., 2012; Cerpa et al., 2017; Menant et al., 2019; Wilson et al., 2014). The impact of prograde metamorphism is so strong, that seismicity stops below certain depth, defining the end of the seismogenic zone (Fig. 1.4). When temperature surpass the 350°C limit, serpentinization starts, developing a metamorphic front in the base of the overriding plate (Fig. 1.4). Minerals that host water on their inner structure will progressively start to release it, hydrating rocks of the mantle wedge, provoking serpentinization (Fig. 1.3a, Fig. 1.4). Laboratory experiments show that a and b values of serpentinites are velocity strengthening, indicating that no seismicity is expected (Moore & Lockner, 2011; Okazaki & Katayama, 2015; Takahashi et al., 2011). Nevertheless, antigorite–a type of serpentinite–can have velocity weakening behavior if temperature reach 450°C and the

large of that region is long enough to allow rupture nucleation (Erickson et al., 2020; Lapusta et al., 2000).

Finally, recent studies of megathrust earthquakes have shown that upper plate faulting may have an impact on earthquake triggering. Dynamic modeling indicates that faulting within the overriding plate occurs at different stages of the seismic cycle, influenced by internal heterogeneities within the forearc wedge, stress fluctuations, and variations in pore fluid pressure (Cortés-Aranda et al., 2022; Herrera et al., 2023; Wang et al., 2019; Wang & Hu, 2006). Seismicity and creep observations before and after megathrust earthquakes (Jara-Muñoz et al., 2022; Schurr et al., 2020; Shirzaei et al., 2012; Soto et al., 2019) indicate that faults within the overriding plate, specifically those located offshore–in between the coast and the trench– remain active (Fig. 1.3a). Hence, the wedge exhibits focused deformation during the seismic cycle, suggesting that earthquake triggering at the plate interface and upper-plate faulting are mechanically coupled. Notably, upper-plate faults exhibit a stress-state prone to faulting, requiring minimal additional changes in pore-fluid pressure or $\overline{\sigma_n}$ to trigger rupture (Wang et al., 2019). In this framework, fluid flow between the megathrust and the overriding plate has been invoked to explain the triggering of seismicity and/or aseismic slip (Bonini, 2019; Hainzl, 2004), and to interpret geodetic and seismic precursory signals before large megathrust earthquakes(Bedford et al., 2015; Schurr et al., 2020).

The interconnection of all these features acting at the same time, and thus controlling megathrust seismicity over seismic cycle timescales is going to be called the *subduction system* (Hamilton, 1994; McKenzie & Parker, 1967) hereafter.

1.3 The Chilean case

The oceanic Nazca plate subducts beneath the continental South American plate at an average relative convergence velocity of 6.6 cm/year (Quiero et al., 2022). This process delineates the Chilean subduction zone, home to the largest earthquake recorded in modern seismology, the 1960 moment magnitude (Mw) 9.5 Valdivia earthquake (Fig. 1.5). The Chilean Andean margin is characterized by a heterogeneous tectonic and geologic configuration. The age of the subducted plate is younger towards the south

(Fig. 1.5), increasing the thermal regime at the subduction zone (Syracuse et al., 2010; Völker et al., 2011). Recent studies have shown that, by doing so, metamorphic fluids are released at the plate interface and upper plate (Fig. 1.4 and 1.5), redistributing heat and thus cooling the hottest part of the system (Spinelli et al., 2016). This effect decreases the temperature in regions where the subducted plate is younger, averaging the thermal distribution throughout the entire margin.

Decades of geological surveying and geophysical imaging have defined the rock composition and structure of the forearc wedge. While northern rocks close to the coast are mainly of volcanic composition, featuring a Mesozoic volcanic arc (Charrier et al., 2007), they are progressively substituted by Late Paleozoic metamorphic belts, representing a paleo-subduction zone southwards (Hervé et al., 2007). These differences are also observed in the large package of highly deformed Paleozoic sediments in the Andean cordillera in Northern Chile, generating thin and thick skinned fault and thrust belts (Giambiagi et al., 2022), which thicken the continental crust and thus increase the depth of the Mohorovičić (Moho) discontinuity to a peak close to 75 km (Fig. 1.5b, Assumpção et al., 2013; Beck et al., 1996; Tassara et al., 2006). Conversely, Southern Chile highlights Mesozoic and Cenozoic batholiths deformed during Andean uplift, covered by volcanic sequences of the currently active volcanic arc, developing thick skinned fault and thrust belts and extensional basins towards the back arc (Echaurren et al., 2022; Folguera et al., 2011), keeping an average crustal thickness of 30 – 35 km (Fig. 1.5b).

As explained in Section 1.2, crustal Moho depth and composition at the subduction channel may impact megathrust seismicity. Moreover, forearc rock composition is a first-order factor governing vertical stress over the plate interface (Tassara, 2010). There is an increase in chemical and mechanical weathering towards the Southern Andes, manifested by the increase in erosion rates due to the evolution of the climate to more rainfall and glacier configurations (Fig. 1.5b, Carretier et al., 2018). Those sediments are transported to the trench by submarine canyons, increasing the trench infill from north to south and thus feeding the subduction channel (Fig. 1.5a). These parameters, along with those modulating friction at the megathrust (eq. 1.1), imprint a

seismic segmentation along the entire margin (Molina et al., 2021), making the seismic behavior nonhomogeneous. In fact, recent decades have shown that the Chilean margin hosts a wide range of megathrust earthquakes, from large (7 < Mw < 8.5) up-dip and down-dip ruptures to giant (Mw > 8.5) events. Historical records suggest that both Northern and Southern Chile may nucleate giant ruptures (Fig. 1.5a, Ruiz & Madariaga, 2018), although new studies indicate that the magnitude of the 1877 megathrust earthquake in Northern Chile was not as big as previously proposed (Vigny & Klein, 2022).

Despite major tectonic differences, large down-dip ruptures are a feature that can be observed throughout the entire Chilean margin. Great examples include the 1995 Mw 8.0 Antofagasta, 2007 Mw 7.8 Tocopilla, 1983 Mw 7.7 Copiapo, 1971 Mw 7.8 La Ligua, and 2016 Mw 7.6 Melinka earthquakes (Fig. 1.5a, Ruiz & Madariaga, 2018). Several studies have proposed different mechanisms for earthquake nucleation at the down-dip segment of the seismogenic zone, ranging from changes in the frictional properties from unstable to conditionally stable regimes (Schurr et al., 2012), basal erosion and underplating (Cubas et al., 2022), and changes in the pore-fluid pressure (Moreno et al., 2018a). However, a common process that reconciles observations is still missing.

The diverse nature of the seismic behavior at the Chilean subduction zone raises several unanswered questions: **How does the geological control affect megathrust seismicity observed in the last century? Are these features acting during seismic cycle timescales? Is there any mechanical relationship between large and giant ruptures? How does the upper-plate structure impact megathrust seismicity?** Currently, the increasing amount of geological and geophysical data allows the implementation of numerical models aimed at understanding some of the key aspects governing the seismic cycle. Using up-to-date numerical frameworks, this work will focus on unraveling how the subduction system impacts on the frictional parameters at the plate interface, which ultimately modulate megathrust seismicity in regions where a higher degree of locking has been observed (Fig. 1.5a).

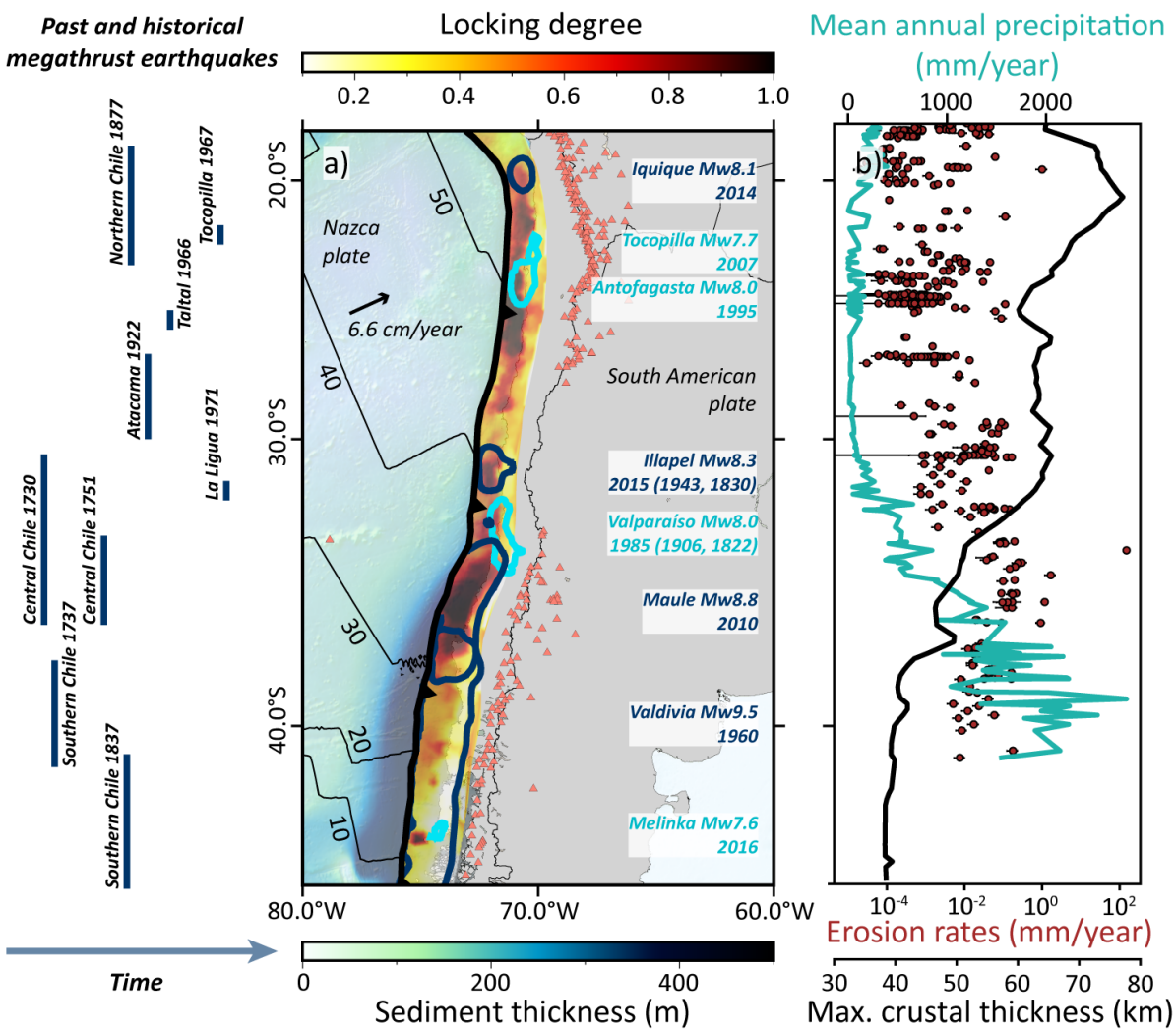

Fig. 1.5. Tectonic and seismic overview of the Chilean subduction zone. a) Tectonic map of the Chilean subduction zone. The locking degree correspond to the period before 2010 (Moreno et al., 2011; Moreno et al., 2014). Sediment thickness is obtained from (Straume et al., 2019). Black contours are the seafloor age in million years (Seton et al., 2020). Historical earthquakes and coseismic extensions are from (Ruiz & Madariaga, 2018). Following the classification of (Lay et al., 2012; Scholz, 1998), dark blue and light blue contours are coseismic slip areas of earthquakes rupturing the B and C segments of the seismogenic zone respectively. b) Latitudinal variation of mean annual precipitations and erosion rates from (Carretier et al., 2018). Maximum crustal thickness from (Tassara & Echaurren, 2012).

1.4 Scientific problem, hypothesis, and objectives

Since the influence of the geological and rheological structure in the seismic cycle along the Chilean subduction zone has not been addressed, this work will be focused into understand ***how key features of the subduction system as the hydraulic state at***

the plate interface, the thermal regime, the compositional variance of the subduction channel, the rheology of the overriding plate, and the offshore structure of the forearc wedge, may have an impact on the seismicity and rupture development at the megathrust.

To do so, this research will be centered around the following hypothesis: ***The structure of the subduction system controls the size, recurrence, and imprint a mechanical relationship between the family of earthquakes nucleated at the megathrust***. To test it, the main objective of this work is to ***assess the impact of key features of the subduction system on earthquake triggering at the Chilean subduction zone***. Finally, this objective will be developed by addressing the following specific objectives:

1) *Evaluate the effect of the rock composition at the subduction channel over the megathrust seismicity and consequent surface deformation.*
2) *Determine the role of the hydraulic state at the plate interface in the triggering of earthquakes at the megathrust during seismic cycle timescales.*
3) *Analyze de effect of the depth of the continental Moho and offshore upper-plate faulting on the megathrust seismicity and surface deformation.*

1.5 Thesis overview

This work is presented in 5 chapters. The first one describes the theoretical summary of the scientific problem to be addressed. Then, chapters 2 and 3 are the articles developed to answer the knowledge gap found before. In chapter 2, the focus is put into how the geological and rheological structures govern earthquakes size and recurrence patterns in Southern Chile. Then, chapter 3 is a study about the impact of the hydraulic state in the precursory phase of the Iquique earthquake in Northern Chile, highlighting the role of upper-plate faulting over seismicity at the megathrust. Chapter 4 discuss how these key features of the subduction system control the seismic cycle at the Chilean subduction zones, leading to the main conclusions in chapter 5.

1.6 Methods (summary)

The extensive details of all the methodologies used in this work is presented on each of the following chapters. Nevertheless, a brief summary of the main tools used to compute numerical models of the Chilean subduction zone is going to be mentioned here.

1.6.1 Numerical models

Each of the numerical simulations presented in this work, has been developed assuming that the frictional behavior of the megathrust and any other fault, follows a SRSF law (eq. 1, Barbot, 2019a). The geometry of the megathrust has been constrained using the Slab2 model (Hayes et al., 2018), while the structure of the upper-plate fault has been delineated using seismicity, seismic wave profiles and focal mechanisms (Chapter 3). All these faults are embedded over a viscoelastic oceanic and continental mantle, whose rheology is thermally activated following a power-law creep constitutive equation (Hirth & Kohlstedt, 2003; Masuti et al., 2016). Within this framework, the rheological properties where choose assuming a wet olivine petrology (Karato & Jung, 2010) and considering the occurrence of a cold nose above the down-dip decoupled megathrust (Wada et al., 2008), which is also incorporated.

The temperature model used to activate the viscoelastic mantle has been computed using the steady state heat advection-diffusion equation, which is solved with a finite element method (Araya et al., 2023). We assumed a layered structure for the lithosphere using the density model of Tassara and Echaurren (2012), from where an average thermal conductivity and diffusivity is assumed for each layer of the lithosphere (upper crust, lower crust, and lithospheric mantle).

The distribution of the frictional parameters at each fault is defined using a compilation of geological and geophysical data. Two key latitudes of the Chilean subduction zone have been selected, Northern Chile (20°S) where the recent Mw 8.2 2014 Iquique earthquake occur, and Southern Chile (43°S) due to the triggering of the deep Mw 7.6 2016 Melinka earthquake in the same segment of the Mw 9.5 1960 Valdivia earthquake.

The structure of each subduction system was defined using seismic wave profiles, background seismicity, locking degree models, coseismic slip models, seismic tomographies, and bathymetric datasets. The velocity weakening region of the megathrust – the seismogenic zone – was defined by looking at the distribution of interplate seismicity with depth, the decrease in the locking degree with depth, the intersection of the continental Moho with the geometry of the megathrust derived from the Slab2 model, and the location of the 350°C isotherm obtained from the computation of each thermal model.

The rate weakening and rate strengthening values ($a - b$) was defined by assuming a specific composition of the minerals being deformed at the megathrust with depth, based on the tectonic settings that characterize the Chilean margin at each latitude. To assume if the frictional behavior of the fault may be governed by sediments being subducted or altered basalts from the oceanic plate, several seismic wave profiles were analyzed detecting if a subduction channel is present.

Finally, once each parameter has been defined, the interaction of stress and traction with time is obtained by solving the fundamental equations of continuum mechanics. Particularly, the conservation of linear momentum at steady state (Navier's equation):

$$\nabla \cdot (C : \varepsilon) + f = 0 \qquad \text{eq. 1.3}$$

where C is the elastic moduli tensor, ε is the strain tensor, f is the body-force density, and the dot and colon denote the dot and doble dot product respectively. To solve it, it is assumed that the material subjected to a certain elastic stress follows the constitutive stress–elastic strain relationship (Barbot, 2018b):

$$\sigma = C : \varepsilon^{e} \qquad \text{eq. 1.4}$$

in which σ is the Cauchy stress tensor. Since many of Earth's processes are anelastic, such as faulting and viscoelastic deformation, then the strain tensor cannot be purely elastic (Andrews, 1978):

$$\varepsilon = \varepsilon^e + \varepsilon^a \qquad \text{eq. 1.5}$$

Fortunately, the body-force density is related to the anelastic strain tensor (ε^a) as follows (Barbot, 2018b):

$$f = -\nabla \cdot m \qquad \text{eq. 1.6}$$

$$m = C : \varepsilon^a \qquad \text{eq. 1.7}$$

where m is the moment density. The total displacement $u(x)$ due to anelastic strain and the elastic response of the medium can be obtained by solving the momentum equation (Barbot, 2018b):

$$\varepsilon = \frac{1}{2}(\nabla u + \nabla u^t) \qquad \text{eq. 1.8}$$

in which ∇u^t is the transpose of the displacement gradient. Finally, the stress field is derived by removing the anelastic strain contribution combining eq. 1.4 and 1.5 as follows (Barbot, 2018b):

$$\sigma = C : (\varepsilon - \varepsilon^a) \qquad \text{eq. 1.9}$$

This equation applies to the quasi-static domain and is valid if plastic deformation does not affect the elastic moduli in the medium and inertia can be ignored (Barbot, 2018b). Then, to apply this framework to the subduction system, the integral numerical method is used (Barbot, 2018a, 2020; Barbot et al., 2017; Muto et al., 2019), where surface and volume elements may be integrated. If the anelastic strain is confined to the viscoelastic domain of the oceanic and continental mantle, changes in fault traction depends on the surrounding fault slip and distributed strain. This allows to write the shear traction as (Barbot, 2020; Shi et al., 2020):

$$\dot{\tau} = \int_{\partial\Gamma} K \cdot (v - v_L) dA + \int_{\Delta} J \cdot (\dot{\varepsilon} - \dot{\varepsilon_L}) dV - \frac{G}{2V_s}\dot{V} \qquad \text{eq. 1.10}$$

where K is the stress kernel for slip on the megathrust surface $\partial\Gamma$, v is the instantaneous slip velocity vector, v_L is the local loading rate on the fault (convergence

rate), $\dot{\varepsilon}$ is the anelastic strain-rate tensor from eq. 1.5 in the ductile domain Δ, and J is another stress kernel connecting distributed deformation to fault traction. The last term of eq. 1.10 correspond to a radiation damping approximation controlled by the rigidity G, the shear wave velocity V_s and slip acceleration $\dot{V}$ (Rice, 1993). Similarly, the evolution of stress in the ductile region can be expressed as (Barbot, 2020; Shi et al., 2020):

$$\dot{\sigma} = \int_{\Delta} M \cdot (\dot{\varepsilon} - \dot{\varepsilon_L}) dV + \int_{\partial\Gamma} L \cdot (v - v_L) dA \qquad \text{eq. 1.11}$$

where M is a stress kernel associated with viscoelastic flow and L is another stress kernel associated with fault slip. This formulation assumes background slip-rate v_L and strain-rate $\dot{\varepsilon_L}$, both possibly non-uniform, at which no stress is being accumulating. Combining the SRSF law (eq. 1.1) and the Navier's equation (eq. 1.9), where ε^a is controlled by the thermally activated power-law creep constitutive formulation (Hirth & Kohlstedt, 2003), a closed system of equations is formed and can be evaluated numerically. To do so, we employ the software UniCyclE (Barbot, 2018a, 2020; Barbot et al., 2017; Muto et al., 2019; Shi et al., 2020), where all the geometries and parameters involved were constrained by geological and geophysical information and ensuring numerical convergence.

2 Recurrence time and size of Chilean earthquakes influenced by geological structure.

Joaquín Julve [1,2], Sylvain Barbot[3], Marcos Moreno[4], Andrés Tassara[1,2], Rodolfo Araya[5], Nicole Catalán[1], Jorge G. F. Crempien[4] & Valeria Becerra-Carreño[4].

[1]Departamento Ciencias de la Tierra, Facultad de Ciencias Químicas, University of Concepción, Concepción, Chile.

[2]Millennium Nucleus: The Seismic Cycle Along Subduction Zones CYCLO, Valdivia, Chile.

[3]Department of Earth Sciences, University of Southern California, Los Angeles, CA, USA.

[4]Department of Structural and Geotechnical Engineering, Pontifical Catholic University of Chile, Santiago, Chile.

[5]Departamento de Ingeniería Matemática, University of Concepción, Concepción, Chile.

The second chapter corresponds to the first paper developed during this thesis. It was submitted to *Nature Geoscience* on January 21st, 2023, and accepted on October 19th, 2023 (Published on December 15th, 2023).

Cite as: Julve, J., Barbot, S., Moreno, M. et al. Recurrence time and size of Chilean earthquakes influenced by geological structure. Nat. Geosci. 17, 79–87 (2024). https://doi.org/10.1038/s41561-023-01327-8.

Abstract

In 1960, the giant Valdivia earthquake (moment magnitude, $Mw\,9.5$), the largest earthquake ever recorded, struck the Chilean subduction zone, rupturing the entire depth of the seismogenic zone and extending for 1,000 km along strike. The first sign of new seismic energy release since 1960 occurred in 2017 with the Melinka earthquake ($Mw\,7.6$), which affected only a portion of the deepest part of the seismogenic zone. Despite the recognition that rupture characteristics and rheology vary with depth, the mechanical controls behind such variations of earthquake size remain elusive. Here we build quasi-dynamic simulations of the seismic cycle in

southern Chile including frictional and viscoelastic properties, drawing upon a compilation of geological and geophysical insights to explain the recurrence times of recent, historic, and palaeoseismic earthquakes and the distribution of fault slip and crustal deformation associated with the Melinka and Valdivia earthquakes. We find that the frictional and rheological properties of the forearc, which are primarily controlled by the geological structure and fluid distribution at the megathrust, govern the magnitude and recurrence patterns of earthquakes in Chile.

2.1 Introduction

Earth's largest earthquakes, frequently accompanied by devastating tsunamis, are hosted at subduction zones, outlying the key importance to understand subduction dynamics during the seismic cycle. This process is controlled by the structure of the Accretionary Prism and the fabric of the megathrust—the seismogenic interface that separates the downgoing oceanic lithosphere from the upper plate. Earthquakes originate from a frictional instability at the plate interface, primarily affected by the lithology, temperature, and fluid content of the fault zone, leading to a stratification of source properties (Lay et al., 2012; Scholz, 1998; Saffer & Tobin, 2011). Numerous studies have shown variability in rupture width and slip of earthquakes in different depth domains, encompassing great ruptures (moment magnitude, $Mw > 8.5$) with a trench-breaking feature (Qiu & Barbot, 2022), and large blind ruptures ($7 < Mw < 8.5$) nucleated within the interseismically locked region as illustrated by palaeoseismic and instrumental record at the Japan (Barbot, 2020), Sunda (Lay, 2015), and Aleutian (Ye et al., 2021) trenches. The succession of large and great ruptures at the subduction megathrust modulates the size and frequency of earthquakes, but the underlying mechanics are uncertain.

The Southern Chile Subduction Zone (SCSZ) produced the Mw 9.5 Valdivia 1960 mega-quake (Plafker & Savage, 1970), the largest earthquake on record, which was followed 56 years later by the Mw 7.6 Melinka earthquake (Ruiz et al., 2017) (Figure 2.1). The 2016 Melinka rupture concentrated in the down-dip limit of the Valdivia

earthquake, sparing the central part of the seismogenic zone that is currently locked (Ruiz et al., 2017).

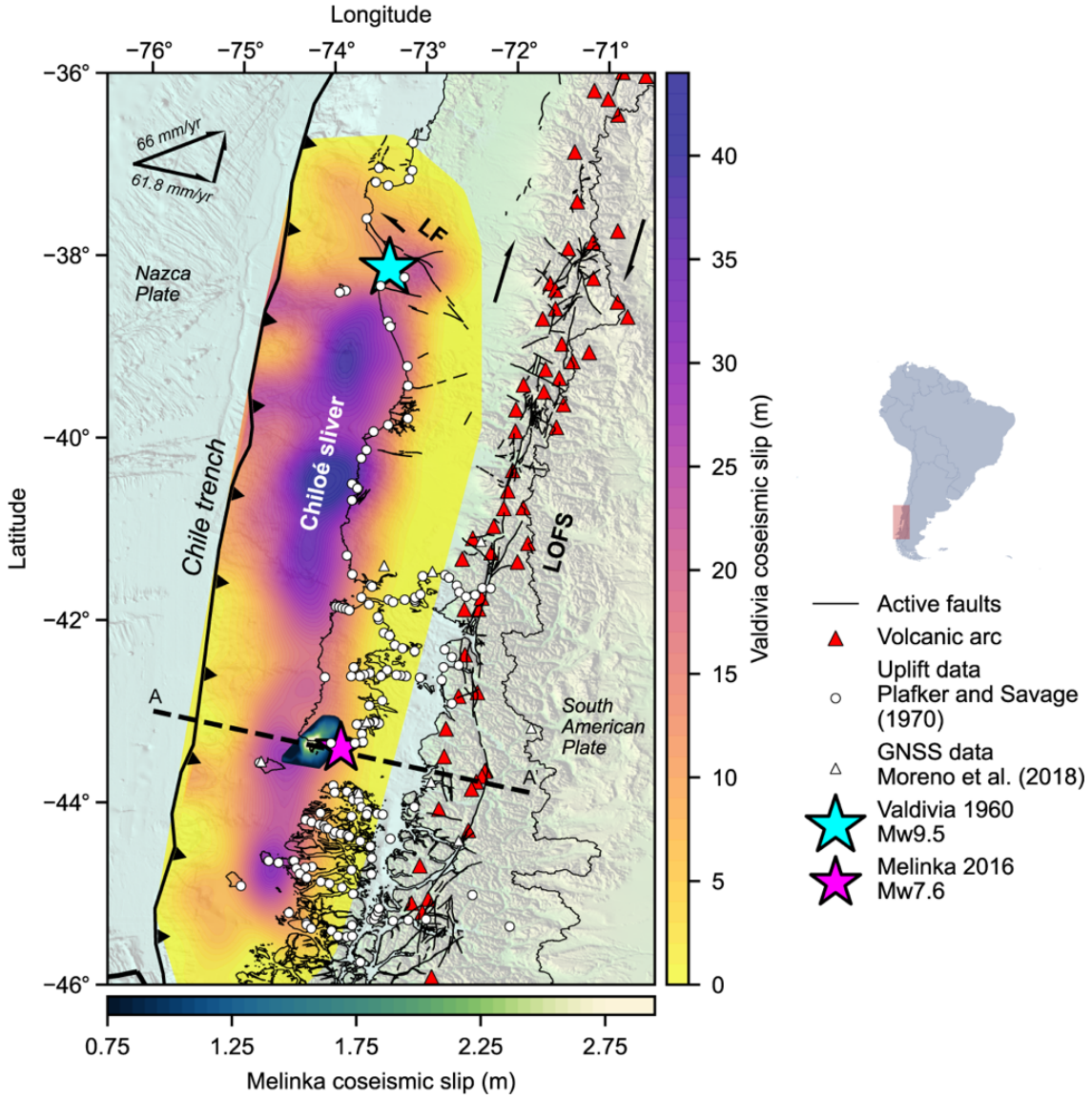

Figure 2.1. Tectonic setting of the Southern Chile Subduction Zone. Coseismic slip model of the Valdivia earthquake (Moreno et al., 2009) and coseismic slip model of the Melinka earthquake (Moreno et al., 2018). LOFS, Liquiñe-Ofqui Fault System; LF, Lanalhue Fault, and active crustal faults. The Chiloé Sliver (Melnick et al., 2009) is bounded by the trench, the LOFS, and the LF. We consider the slip distribution and seismic cycles along the representative cross section A – A'. Basemap is from GEBCO Compilation Group GEBCO 2023 Grid (National Oceanic Centre & British Oceanographic Data Centre, 2023).

The sequence of a full-depth rupture followed by seismic resurgence in the deep segment of the seismogenic zone, along with the extensive geodetic, geophysical, and

palaeoseismological record associated with the 1960 mainshock, is fundamental to explore the factors that control the slip evolution and recurrence of subduction earthquakes.

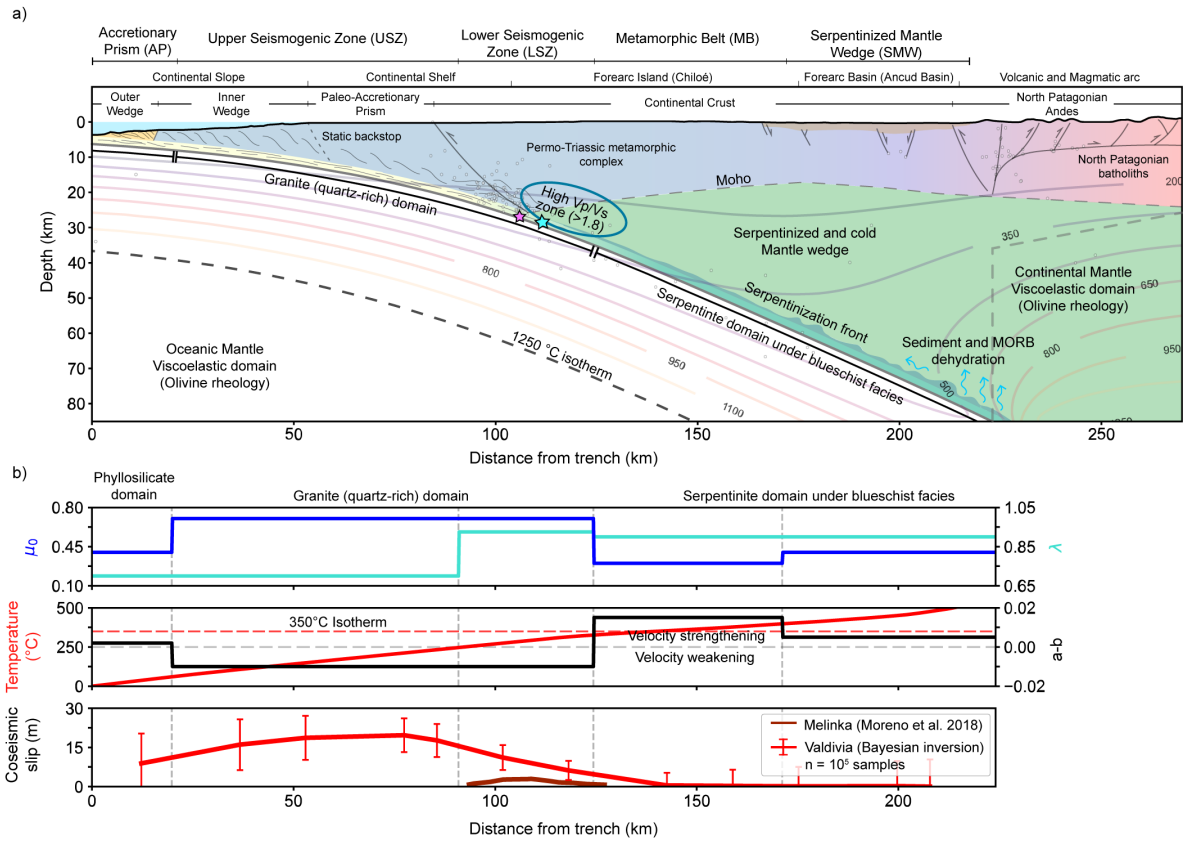

Figure 2.2. Summary of data acquired and set-up of the model. a) Cross section of the SCSZ with the compilation of available data. Crustal faults are from Maldonado et al. (2021), interseismic seismicity is from Lange et al. (2007), and outer and inner wedge structures are from Bohm et al. (2002). Horizontal lines and names at the top of the figure define the downdip megathrust segments presented in our work. b) Set-up of the quasi-dynamic model, μ_0 is the reference coefficient of friction, λ is the pore pressure ratio assumed at each segment, and $a - b$ is the parameter obtained from equation 3 (Chapter 2.6.1). The temperature is obtained from our thermal model (Chapter 2.6.2) at the plate interface. The Melinka slip was obtained from Moreno et al. (2009) while the Valdivia slip is the result of our new inversion (Chapter 2.6.4), where error bars are one standard deviation.

Here we implement a numerical model of the seismic cycle at the SCSZ with depth-variable rate- and state-dependent frictional properties on the megathrust and thermally activated rheological properties in the subducting oceanic asthenosphere and overturning mantle wedge underneath the upper plate. We base the constitutive

properties on our own thermal model of the SCSZ (Chapter 2.6.2) and the lithology of the subducted channel and surrounding lithosphere. We construct a cross section of the SCSZ with a structural layout compatible with geological and geophysical observations. We then explore how the recurrence periods, slip, and deformation of large and great earthquakes are controlled by the frictional properties of the megathrust. Our optimal model, based on a sensitivity analysis of the main parameters controlling frictional resistance, such as rheology and pore pressure ratio (λ), allows us to match multiple measurements at the earthquake cycle in Chile, providing new insights into the mechanical control of subduction earthquakes.

2.2 Modelling the subduction seismic cycle of the southern Andes

Using quasi-dynamic numerical simulations that resolve the mechanical interactions between a frictional megathrust and a temperature-controlled viscoelastic asthenosphere, we simulate the occurrence of great (Valdivia-like) and large (Melinka-like) ruptures throughout the seismic cycle of the SCSZ. The model resolves all phases of the seismic cycle, including nucleation and propagation of earthquakes, along with afterslip and viscoelastic relaxation that follow the mainshocks. We build a model of subduction dynamics along a representative cross section (Figure 2.2a) assuming a 61.8 mm per year convergence rate between the Nazca and South American plates in the trench-perpendicular direction (Quiero et al., 2010). The structural layout is constrained by the Slab2 model (Hayes et al., 2018), seismicity (Lange et al., 2007; Bohm et al., 2002), seismic wave tomography and reflection profiles (Contreras-Reyes et al., 2010; Bangs et al., 2020; Maksymowicz et al., 2022; Maksymowicz et al., 2021; Scherwath et al., 2009), and gravity-constrained density models (Maksymowicz et al., 2022; Tassara & Echaurren, 2012). The outer wedge is defined by the highly deformed Accretionary Prism (Contreras-Reyes et al., 2010). The inner wedge extends from the outer arc high to the continental slope, featuring inactive accretion structures. The Lower Seismogenic Zone encompasses the palaeoprism up to the intersection with the Moho, presenting underplating structures (Maksymowicz et al., 2021; Krawczyk et al., 2006) and seismic wave velocities (Contreras-Reyes et al., 2010) and density (Maksymowicz et al., 2022) anomalies suggesting the presence of a high ratio of

compressional to shear wave velocities (V_p/V_s) (Dzierma et al., 2012) and a static backstop. Eastwards, the continental crust transitions from Permo–Triassic metamorphosed units to granitoids of the North Patagonian Batholith (Echaurren et al., 2022). The Liquiñe–Ofqui Fault System (Cembrano et al., 1996) (LOFS) deforms the granitoids and bounds the eastern part of the Chiloé Sliver (Figure 2.1a). Beneath the continental crust, the megathrust underlies the Metamorphic Belt and the Serpentinized Mantle Wedge, terminating at the 650 °C isotherm at about 85 km depth. From there, the downgoing slab is permanently coupled to the mantle wedge that deforms by viscous flow.

We assume that the frictional behavior of the megathrust is controlled by a slip-rate- and state-dependent friction law (Barbot, 2019b, 2020) (equation 2.3 in Chapter 2.6.1):

$$\tau = \mu_0 \bar{\sigma} \left(\frac{V}{V_0}\right)^{\frac{a}{\mu_0}} \left(\frac{\theta V_0}{L}\right)^{\frac{b}{\mu_0}} \qquad \text{eq. 2.1}$$

where μ_0 is the effective coefficient of friction, $\bar{\sigma}$ is the effective normal stress, V and V_0 are the instantaneous and reference velocities at the fault interface, θ is a state variable that follows an evolution law allowing healing at stationary contacts (Barbot, 2020) and L is a characteristic slip distance. The direct and steady-state velocity dependence of friction is controlled by the parameters a and $a-b$, respectively, with $a-b<0$ corresponding to velocity-weakening, potentially unstable friction and $a-b>0$ giving rise to velocity-strengthening friction, which inhibits rupture nucleation and propagation. Guided by the expected mineralogical composition at the plate interface and considering the thermal structure, we use laboratory-derived information extracted from fault gouges to constrain the frictional parameters assigned to the megathrust (Table 2.1). The depth-dependent thermal and compositional stratification leads to a structural model for the fault with five down-dip segments with distinct properties (Figure 2.2b).

Seismic wave profiles (Contreras-Reyes et al., 2010) and sedimentary fluxes (Kukowski & Oncken, 2006) indicate a trench fill varying from 1 to 3 km (Krawczyk et al., 2006), reflecting the strong denudation of the exhumed North Patagonian Batholith (Genge et al., 2021) during the last Pliocene glaciation (Melnick & Echtler, 2006). The

erosion of the Andean Cordillera (Adriasola et al., 2006) allows us to assume that friction in the outer wedge is controlled by a mixed phyllosilicates and quartz composition. We use average values from laboratory results on fault gouges composed of about 50% quartz and 50% clay minerals at low temperatures (Tembe et al., 2010; den Hartog et al., 2012), yielding $a - b = 2x10^{-3}$. As ~80% of the sediments enter the subduction channel (Behrmann & Kopf, 2001), we assume that the seismogenic zone is controlled by a granitic composition (Liu & Rice, 2009), rather than by altered basalts from the subducting slab (Figure 2.2a), leading to $a - b = -1x10^{-2}$ in the Upper and Lower Seismogenic Zone (Figure 2.2b). Finally, background seismicity and locking degree models show the transition from a locked to creeping fault at 35 km depth (Lange et al., 2007; Melnick et al., 2018), suggesting that the megathrust shifts to velocity-strengthening properties beyond the continental Moho. Fluid-driven serpentinization occurs in the cold mantle wedge, developing a serpentinization front at the plate interface (Angiboust et al., 2012). We assume frictional parameters of serpentinites (Okazaki et al., 2015; Takahashi et al., 2011; Moore & Lockner, 2011) to characterize the two deepest segments. This accounts for the transition from lizardite to antigorite at ~350 °C (Schwartz et al., 2013), leading to $a - b = 1.5x10^{-2}$ underneath the Metamorphic Belt and $a - b = 5x10^{-3}$ below the Serpentinized Mantle Wedge (Figure 2.2b).

The effective normal stress on the megathrust depends on the local value of the partial fluid pressure ratio (λ) via $\bar{\sigma} = \sigma_n(1 - \lambda)$, where σ_n is the local normal stress based on gravity (equation 14 in Chapter 2.6.3). Our initial set-up considers published estimates of λ at the Accretionary Prism (Saffer & Wallace, 2015) that suggest an overpressure region at the bottom of the seismogenic zone (Saffer & Tobin, 2011; Moreno et al., 2018) (Table 2.1). To obtain the pressure–temperature path along the fault (Supplementary Figure 6.1), we build a finite-element thermal model based on near-lithostatic pore fluid pressure at megathrust depth (Araya et al., 2023), where the temperature satisfies the steady-state heat advection–diffusion equation (Chapter 2.6.2). The resulting temperature distribution (Supplementary Figure 6.1a and Figure 2.2a) shows the same depth of the 650 °C isotherm (~85 km) as previous models

(Spinelli et al., 2016; Völker et al., 2011) but features a deeper 350 °C isotherm. For the viscoelastic domain, we assume the rheological parameters of olivine aggregates for transient and steady-state dislocation creep (Karato & Jung, 2010; Masuti et al., 2016) and divide the mantle wedge into a serpentinized wet region below the arc and a dry region farther east, establishing a cold-nose configuration (Wada et al., 2011) (Supplementary Figure 6.1a and Supplementary Table 6.1). Viscoelastic deformation on each volume element is captured by a Burger's assembly of springs and dashpots (Masuti et al., 2016) whereby the anelastic strain rates in the Maxwell and Kelvin elements follow a power-law rheology (equation 7 Chapter 2.6.1), which is activated with the background temperature distribution of the finite-element thermal model (equation 13 in Chapter 2.6.2). Finally, we conduct simulations spanning 10,000 years of seismic activity following the distribution of parameters constrained by the geological structure, providing the surface displacement associated with various sequences of total and partial ruptures in the SCSZ (Figure 2.3a) and the distribution of down-dip slip. The simulations employ adaptive time steps to capture the details of rupture initiation and propagation and the more quiescent periods in between. To mitigate bias from initial conditions (Erickson et al., 2020), we focus on the last 7,500 years of each simulation during which the patterns of the rupture sequences are stable over time.

Table 2.1. Frictional parameters of the preferred and initial models.

Segment	Geology	References	a	b	L (m)	a-b	σ (Mpa)	μ	W (m)	λ
AP	phyllosilicates + qtz	35, 36	1.00E-02	8.00E-03	7.50E-02	2.00E-03	45	0.40	19997	0.700*
LSZ	granite	38	3.00E-03	1.30E-02	1.50E-02	-1.00E-02	113	0.60	72790	0.700
USZ	granite	38	3.00E-03	1.30E-02	1.00E-02	-1.00E-02	56	0.60	29596	0.925
MB	lizardite	40, 41 ,42	2.00E-02	5.00E-03	5.00E-02	1.50E-02	130	0.30	84788	0.900
AB	antigorite	40, 41, 42	1.00E-02	5.00E-03	5.00E-02	5.00E-03	220	0.40	59780	0.900

2.3 Earthquake cycle observations

Decadal records of crustal deformation allow the characterization of the earthquake cycle, in which vertical tectonic displacements modulate the local relative sea level by several meters, while horizontal deformation evolves on a continental scale (Weiss et al., 2019). The surface deformation associated with the Valdivia earthquake is

constrained by an extensive array of biological and anthropogenic markers that capture coseismic and postseismic vertical displacements (Plafker & Savage 1970), involving slip on the megathrust but also an eight-year-long viscoelastic flow in the surrounding lithosphere (Luo & Wang, 2021). Coseismic deformation of the Melinka earthquake was registered with Global Navigation Satellite System (GNSS) data (Moreno et al., 2018) and intertidal biotic indicators (Garrett et al., 2019) that describe up to 0.3 m of uplift at the Lower Seismogenic Zone. The occurrence of palaeoseismic trench-breaking ruptures followed by large earthquakes in the following years has also been recorded in sediments at lake and fjords of the SCSZ. The recurrence time for earthquakes with $Mw \geq 8.6$ is 292 ± 93 years (Wils et al., 2020; Moernaut et al., 2018), while events with $7.7 \leq Mw \leq 8.5$ happen every 139 ± 69 years (Moernaut et al., 2018).

To calibrate the model, we compare our predictions with the estimations of recurrence times for large and great events at the SCSZ (Wils et al., 2020; Moernaut et al., 2018) and with surface deformation of the Melinka (Moreno et al., 2018) and Valdivia (Plafker & Savage 1970) earthquakes (Supplementary Figure 6.2). We compute the root mean square error between the model results and the available dataset (Supplementary Figure 6.3). Using the distribution of pore fluid pressure ratio from the initial model (Table 2.1), we cannot simultaneously reproduce the recurrence time and the surface deformation after large and great ruptures. We evaluate different configurations of pore fluid pressure ratio at each frictional segment (Supplementary Table 6.2) while keeping the rest of the frictional parameters constant. The pore fluid pressure ratio distribution that minimizes the root mean square error features $\lambda \geq 0.9$ in the Lower Seismogenic Zone, $0.7 \leq \lambda \leq 0.75$ in the Upper Seismogenic Zone and $\lambda = 0.9$ in the Creeping Zone. We use this configuration hereafter as our preferred model (Table 2.1) to describe the rupture mechanics and consequent deformation at the SCSZ.

2.4 Mechanics and surface deformation of simulated earthquakes

We analyze the seismic cycle at the SCSZ viewing a representative example of fault dynamics of our preferred model between 6,000 to 7,000 years (Figure 2.3a). Seismicity predominantly nucleates at the transition from the keel of the continental

crust to the cold nose of the mantle wedge corner. Large earthquakes involve partial ruptures (Figure 2.3a), which include Melinka-like events (Figure 2.3b) that nucleate at the Lower Seismogenic Zone but stopped on their way to the trench. Great ruptures encompass the entire seismogenic zone and the outer wedge (Figure 2.3c), with Valdivia-like events (Figure 2.3c) showing similar rupture style (Cifuentes et al., 1989; Krawczyk, 2003) and trench-breaking propagation (Ho et al., 2019) to the 1960 mega-quake. Despite the assumed velocity-strengthening friction in the outer wedge, all great ruptures break the trench, in line with $Mw > 8.5$ palaeoseismic data (Wils et al., 2020; Hocking et al., 2021), and uplift models derived from tsunami data after the Valdivia earthquake, indicating up to 4 m of seafloor uplift (Ho et al., 2019). Both earthquake types propagate through creep zones resulting from stress concentration at previous event tips (Figure 2.3b,c), indicating a mechanical link between large and great earthquakes. This interaction allows the trench to experience coseismic slip during great ruptures and creeping during interseismic periods (Figure 2.3b–d).

The preferred model predicts recurrences for large (82 ± 43.4 year) and great (271 ± 70 year) ruptures matching the estimates from paleo-turbidites and tsunami deposits (Wils et al., 2020; Moernaut et al., 2018; Kempf et al., 2019) within uncertainties (Figure 2.3e,f). For large earthquakes, the mean recurrence time of simulated eventsapproaches the median recurrence of past earthquakes with $7.7 \leq Mw \leq 8.5$ derived from the geological record and the 56-year lagbetween the 1960 and 2017 earthquakes. In the simulations, the recurrence times and the coseismic slip of each rupture depend mostly on $\bar{\sigma}$, $a - b$ and the width of the seismogenic zone. There is a trade-off between fitting large recurrence times and data-constrained maximum slip, but our model with the optimized pore fluid pressure generates results within the 95% confidence interval of estimations derived from palaeoseismicity (Supplementary Figure 6.3 and Figure 2.3e,f).

We compare simulated surface deformation for great and large ruptures with available uplift data eight years after the Valdivia earthquake and coseismic GNSS data following the Melinka earthquake (Supplementary Figure 6.2). For each great earthquake, we extract vertical displacement produced by coseismic rupture and eight years of

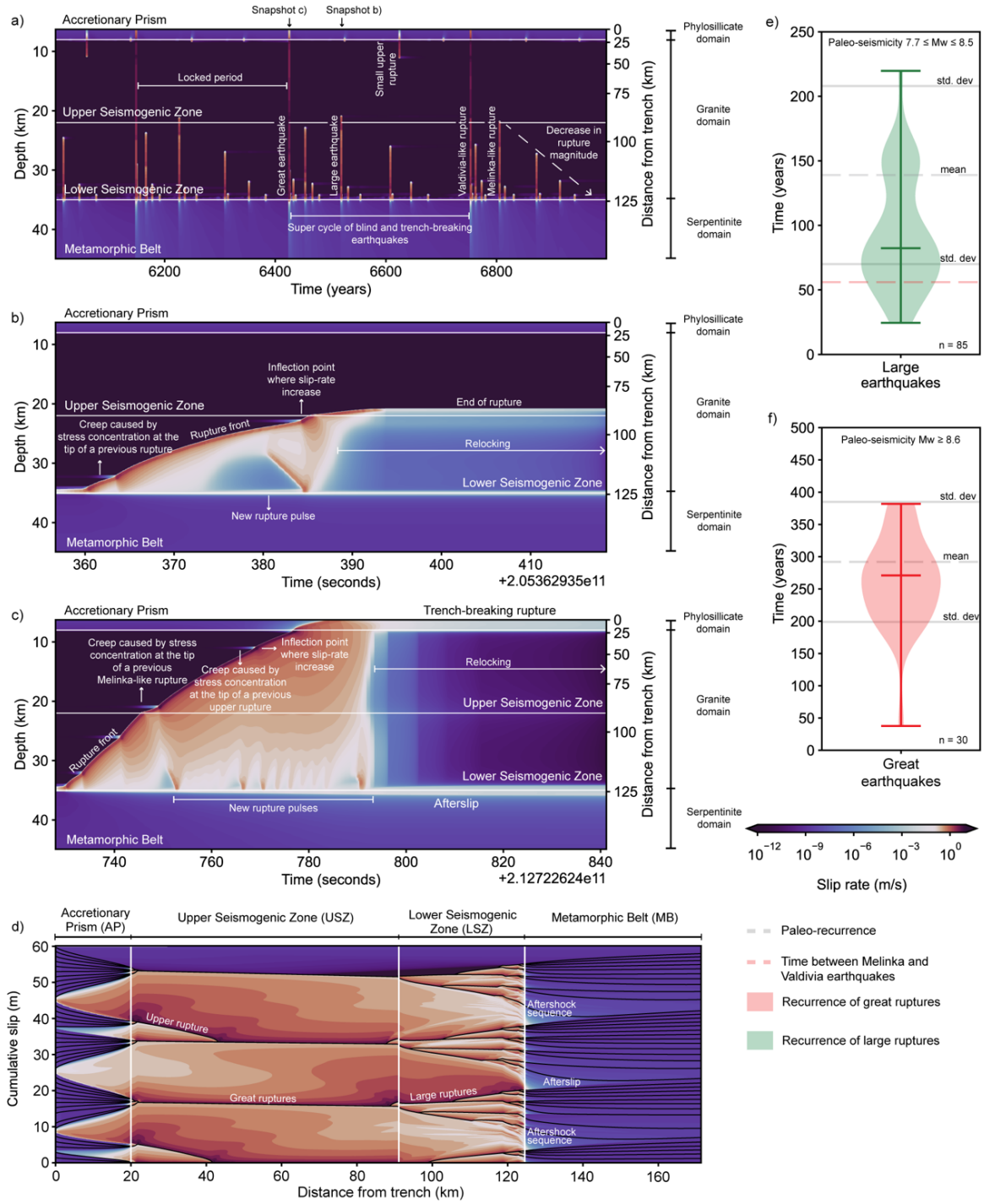

Figure 2.3. Fault dynamics and recurrence times at the SCSZ. a) Slip rate over time of the simulation along the megathrust. b) Snapshot of Melinka-like earthquakes at a). c) Snapshot of Valdivia-like earthquakes at a). d) The cumulative slip over the same period as a); black lines represent the cumulative slip curve every 25 years at the interseismic period. e,f) Violin plots of recurrence times of simulated events showing median, minimum and maximum values against recurrence times of palaeoseismicity presented as mean values with one standard deviation (Wils et al., 2020; Moernaut et al., 2018; Kempf et al., 2019).

postseismic deformation to obtain a surface vertical profile. The median pattern mirrors the observed eight-year Valdivia earthquake deformation, featuring from west to east offshore uplift, coastal subsidence, and volcanic arc uplift (Figure 2.4). Postseismic deformation results from afterslip in the Lower Seismogenic Zone and behind the Metamorphic Belt and viscoelastic uplift in the Accretionary Prism and volcanic arc (Figure 2.4). Uplift at the volcanic arc is attributed to the rheological contrast between the cold nose and a high-temperature mantle beneath it, consistent with prior works (Luo & Wang, 2021). Viscoelastic flow in the oceanic asthenosphere causes postseismic uplift near the trench (Luo & Wang, 2022). The magnitude of uplift is not fully compensated by interseismic subsidence in the years after the main event (Supplementary Figure 6.4 and 6.5), explaining the similar magnitude of coseismic and postseismic uplift (Figure 2.4a).

The slip distribution of the simulated great ruptures eight years after each mainshock is consistent with a Bayesian estimate of coseismic slip for the Valdivia earthquake (Becerra-Carreño et al., 2022) (equation 15 in Chapter 2.6.4) that is inverted form the same land-level changes data captured eight years after the main event. Our kinematic inversion shows up to 7 m of coseismic slip near the trench (Figure 2.4b), like previous results from estimations incorporating tsunami data (Ho et al., 2019), and has the same maximum slip (around 20 m) as past models that include changes in slab geometry (Moreno et al., 2009). The minimum uncertainty is observed between 75 to 150 km from the trench, solving the slip distribution at the end of the rupture and thus coinciding with the end of the seismogenic zone at 35 km depth (Figures 2.2b and 2.4b). A small proportion of simulated giant ruptures generate a slightly lower coseismic slip in the seismogenic zone compared with the geodetic model. However, all simulated events and their median profile (black bold line at Figure 2.4b) match the slip distribution within uncertainties. All simulated great earthquakes generate coseismic slip up to the trench, consistent with the proposed trench-breaking feature of the Valdivia event (Ho et al., 2019).

Finally, we assess crustal deformation linked to large ruptures by comparing model predictions with data from continuous GNSS displacements (Moreno et al., 2018) and

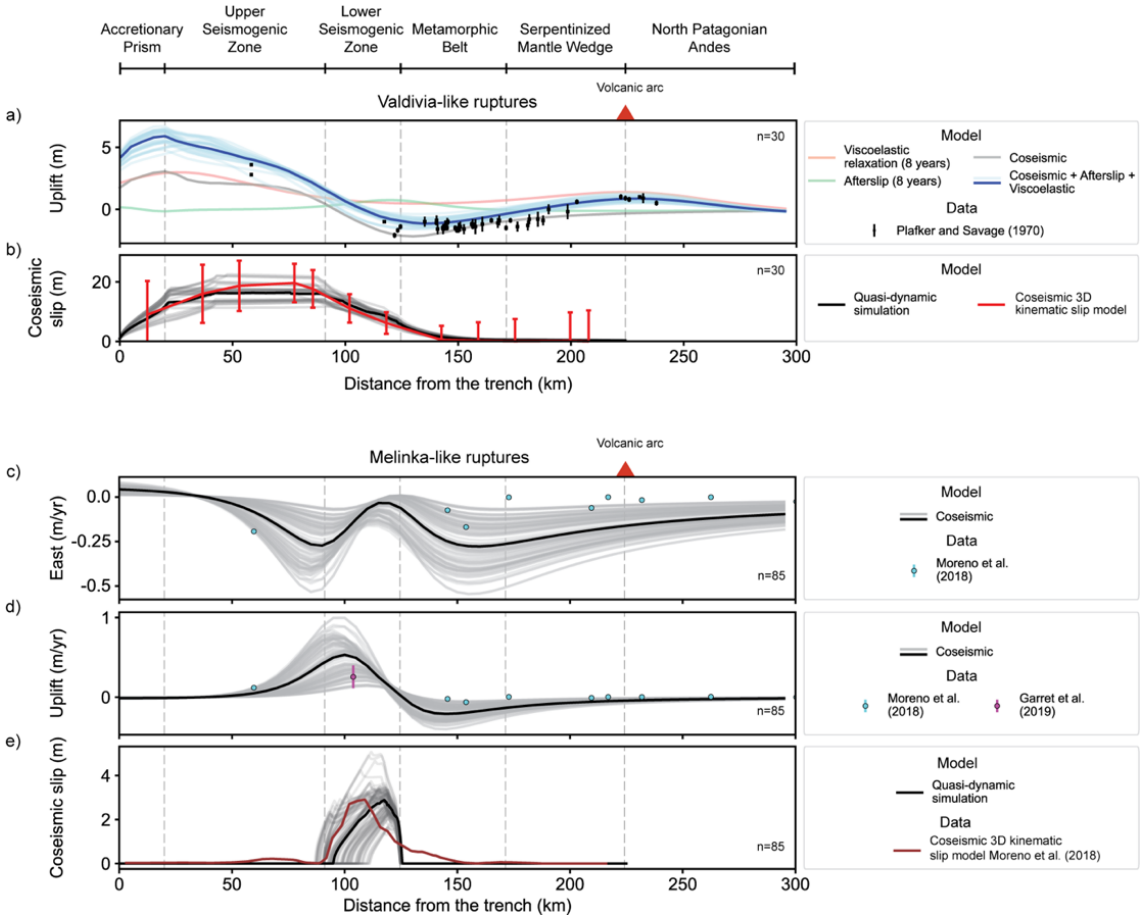

Figure 2.4. Upper crust deformation. a) Comparison between Valdivia-like ruptures with the land-level changes data eight years after the Valdivia earthquake (Plafker and Savage, 1970) and error bars with mean standard error. Bold lines are the mean curve of each component obtained from all simulated events. b) Coseismic slip generated by Valdivia-like ruptures compared against our coseismic slip model (red lines) with one standard deviation (red bars). c) Comparison between Melinka-like ruptures and the East component of the GNSS data from the Melinka earthquake (Moreno et al., 2018). d) Comparison between Melinka-like ruptures and the vertical component of the GNSS data from the Melinka earthquake (Moreno et al., 2018) and uplift from intertidal biotic indicators (Garrett et al., 2019) plus two standard deviations (error bars). e) Coseismic slip generated by simulated Melinka-like ruptures compared against the model of Moreno et al. (2018).

land-level changes (Garrett et al., 2019) following the 2016 Melinka earthquake. Our simulated Melinka-like ruptures (Figure 2.4c,d) show a median curve exceeding the immediate coseismic pattern (Moreno et al., 2018). However, simulations with smaller surface deformation match both horizontal and vertical components of observed data, reproducing coseismic uplift above the Lower Seismogenic Zone inferred from intertidal biotic indicators (Garrett et al., 2019). The amplitude of median simulated coseismic slip agrees with published models (Ruiz et al., 2017; Moreno et al., 2018) but shifts

slightly towards the down-dip limit of the seismogenic zone. Large ruptures represent a family of moderate events, inducing surface deformation ranging from tens to hundreds of centimeters, with up to 4 m of coseismic slip concentrated mainly within the Lower Seismogenic Zone (Figures 2.3a and 2.4c–e). Minor disparities between our two-dimensional models and GNSS data of the horizontal component for the Melinka earthquake (Figure 2.4c) arise due to source–receiver distance decay variations, particularly noticeable in smaller ruptures. Along-strike rupture propagation is an important aspect of megathrust dynamics (Yu et al., 2018). In nature, we expect other Melinka-like earthquakes to initiate at similar depths at different latitudes along the trench axis, but this is not captured within our two-dimensional approximation.

2.5 Subduction cycle at the Valdivia segment

Our synoptic model (Figure 2.5) integrates down-dip variations in the composition of rocks at the subduction channel, lithospheric temperature distribution and mantle rheology to explain the sequence and recurrence of great and large earthquakes and associated crustal deformation in the SCSZ. Our models underscore the role of geological structure and pore fluid pressure in controlling frictional behavior governing large and great earthquake sequences (Supplementary Figures 6.3 and 6.4). If no increase in pore fluid pressure is considered, then the time between each kind of earthquake will not match the observations and the amplitude of uplift and subsidence will not reproduce the coseismic and postseismic data after the Valdivia earthquake. Our models do not explain the origin of fluid concentration at the Lower Seismogenic Zone, but our pressure–temperature path (Supplementary Figure 6.1b) is consistent with in situ fluid release from prograde metamorphism of metapelites (Condit et al., 2020; Hernández-Uribe et al., 2021) at the observed high Vp/Vs ratio zone (Dzierma et al., 2012), outlying the effect of dehydration processes on earthquake mechanics.

Mineralogy at the plate interface also plays an important role. Neglecting sediment input from the erosion of the continental crust, and thus allowing altered oceanic plate basalt to govern friction at the megathrust, fails to explain the eight-year deformation curve following great earthquakes (Supplementary Figure 6.4a). Enlarging the seismogenic

zone width displaces the pattern of surface deformation and coseismic slip inland compared to observations, suggesting that the bottom of the seismogenic zone may be influenced by fluids and/or the continental Moho (Figure 2.5), rather than exclusively by megathrust temperature distribution (Supplementary Figure 6.4b,c).

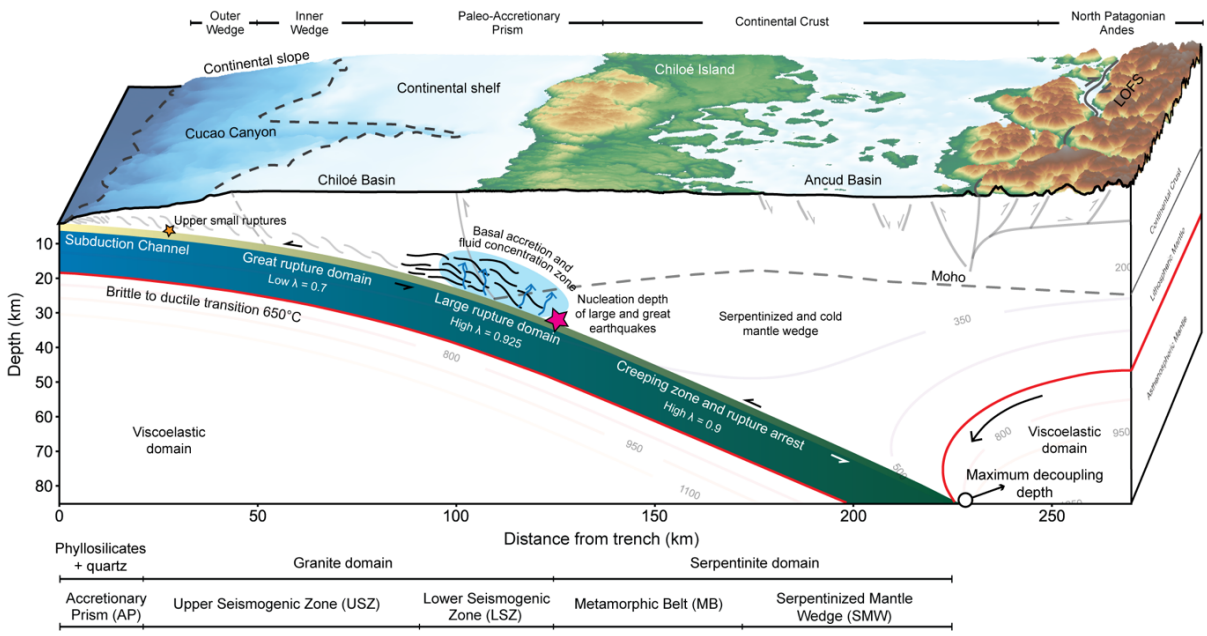

Figure 2.5. Conceptual model of the SCSZ integrating insights from quasi dynamic simulation and compiled data. λ values are the ones calibrated to our preferred model. Nucleation depth is referred to the depth at which large and great ruptures start. Water concentration region is inferred from in situ fluid release (Condit et al., 2020). Basal accretion structures are interpreted from seismic wave profiles (Maksymowicz et al., 2021; Krawczyk et al., 2006). Isotherms are obtained from our modelled thermal distribution. Basemap from NASA EOSDIS (Land Processes Distributed Active Archive Center NASA Shuttle Radar Topography Mission Global 1 Arc Second).

Numerical models constrained by geological and geophysical data, such as presented here, provide an ideal medium to integrate and test geodynamics processes throughout the seismic cycle of megathrust earthquakes, with possible applications at other subduction zones worldwide. Given the spatial relationship between fluid concentration depth and forearc structure at the SCSZ (Figure 2.5), we propose that the seismic cycle depends on the thermodynamic conditions at the plate interface associated with the resulting depth-dependent lithology, hydrothermal regime and geological structure,

leading to a fluid–rock interaction along the seismogenic megathrust that impacts the stability of frictional sliding.

2.6 Methods

2.6.1 Fault friction and mantle viscosity

The stages of the seismic cycle in faults can be described using constitutive relationships of slip-rate- and state-dependent friction that explain the evolution of sliding velocity over time. These laws had been used to model several rupture styles in nature (Lapusta and Rice, 2003) and to characterize the seismic cycle at different tectonic settings. This leads to the possibility of understanding fast and slow ruptures at different fault configurations. Here we use a constitutive framework obtained from the assumption of a microphysical model of the slip-rate- and state-dependent friction under isothermal conditions. In this context, the sliding velocity depends on the density of the real area of contact as follows (Barbot, 2019a):

$$V = V_0 \left(\frac{\tau}{\mathcal{A}\chi}\right)^{\mu_0 a} exp\left[-\frac{Q}{R}\left(\frac{1}{T} - \frac{1}{T_0}\right)\right] \qquad \text{eq. 2.1}$$

where V is the sliding velocity, τ is the norm of the shear stress resolved on the fault plane, T is the absolute temperature, μ_0 is the static coefficient of friction at V_0 and T_0, $\mathcal{A}$ is the real area of contact density (real area of contact divided by the nominal surface area), χ is the indentation hardness, $a \ll 1$ is the direct effect, Q is the activation energy and R is the gas constant. The real area of contact depends on the effective normal stress and changes as a function of the shape of the surrounding contact junctions (Dieterich & Kilgore, 1996). This last feature is characterized by a state variable that represents the age of the grain, which coincides with the age of contact defined by Dieterich (1971). The relationship between the effective normal stress and the real area of contact is given by (Barbot, 2019a):

$$\mathcal{A} = \frac{\mu_0 \sigma_{eff}}{\chi}\left(\frac{\theta V_0}{L}\right)^{b\mu_0} \qquad \text{eq. 2.2}$$

where σ_{eff} is the effective normal stress, θ is the state variable, L is the characteristic weakening distance associated with the gouge thickness or fault roughness and $b \ll 1$ is the evolution effect. By combining equations 2.1 and 2.2, the multiplicative form of slip-rate- and state-dependent friction at isothermal conditions is obtained (Barbot 2019a, 2019b):

$$\tau = \mu_0 \overline{\sigma} \left(\frac{V}{V_0}\right)^{\frac{a}{\mu_0}} \left(\frac{\theta V_0}{L}\right)^{\frac{b}{\mu_0}} \qquad \text{eq. 2.3}$$

The state variable under isothermal conditions follows an evolution law which allows healing at the stationary contacts (Barbot 2019a, 2020):

$$\dot{\theta} = exp\left[-\frac{H}{R}\left(\frac{1}{T} - \frac{1}{T_0}\right)\right] - \frac{\theta V}{L} \qquad \text{eq. 2.4}$$

Fault dynamics are controlled by the spatial distribution of μ_0, $\bar{\sigma}$, a, b and L, which are governed by the thermal state at the fault interfaceand by the mineral assembly of the respective stable lithological facie under that state. We assume that those parameters do not change overtime and are not affected by heat and fluid transport, which means that the value that controls the frictional behaviour on the fault at steady state will be $a - b$. Depending on its temperature distribution, effective normal stress and rock composition, any given fault can experience a velocity-weakening ($a - b < 0$) or a velocity-strengthening ($a - b > 0$) behavior (Marone, 1998). Velocity-weakening areas will experience unstable slipwhereas velocity-strengthening regions should slip aseismically (Bürgmann, 2018). Nonetheless, previous works had shown that velocity-strengthening regions can propagate ruptures (Kozdon & Dunham, 2013).

As can be anticipated from equations 2.3 and 2.4, there is a very wide spectrum of sliding mechanisms that are generated at the fault over time. This introduces high uncertainties about the distribution of the parameters that govern slip-rate- and state-dependent friction relations. Nevertheless, from a dimensional analysis of the frictional equations, (Barbot 2019b) defined two dimensionless parameters that can be understood as two degrees of freedom for the frictional behavior of a given fault:

$$R_u = \frac{(b-a)\sigma_{eff}W}{GL} \quad \text{eq. 2.5}$$

$$R_b = \frac{b-a}{b} \quad \text{eq. 2.6}$$

where R_u is known as the Dieterich–Ruina–Rice number and depends on the geometry of the fault given by the width W of the velocity-weakening patch, on the frictional behaviour given by $a - b$, on the effective normal stress, and on the shear modulus G at plane strain conditions. For a velocity-weakening segment R_u takes positive values and represents the relation between the segment dimension and the nucleation size. Greater values of R_u will lead to the nucleation of smaller instabilities with respect to W (Barbot, 2019b). The other parameter is R_b, which controls the transient evolutionary effects and the strengthening behaviour. Velocity-strengthening patches will have $R_b < 0$, velocity-weakening domains are characterized by $0 < R_b < 1$ and velocity neutral regimes are defined when $R_b \approx 0$. R_b also controls the rupture propagation in the same way as the ratio a/b (Rubin & Ampuero, 2005). At velocity-weakening domains and high sliding velocities, when a/b is close to the unity, then the rupture will tend to extend towards the whole segment. The combination of R_u and R_b gives a two-dimensional space where different rupture styles can arise. By constraining the spectrum of frictional parameters, the actual slip behaviour of a given fault can be approximated. We use this approach to feed the initial state of all the parameters in our model. We collect a wide range of datasets to constrain the pressure–temperature conditions and the slip mechanism at the plate interface. Then, we assume an initial composition for the oceanic plate and for the sediments at the trench. From that point, we use previous stability fields of subduction related metamorphic facies to define the metamorphic state along dip. Finally, we define the frictional parameters using previous gouge data from different lithologies that represent the metamorphic facies at the plate interface. The viscoelastic behavior is calculated using a power-creep law that assumes pure dislocation creep over minerals with a constant water concentration (Karato & Jung, 2010):

$$\dot{\varepsilon} = A\sigma^n C_{OH}^r d^{-m} exp\left(-\frac{Q+p\Omega}{RT}\right) \quad \text{eq. 2.7}$$

where $\dot{\varepsilon}$ is the strain rate, A is a pre-exponential factor, σ is the deviatoric stress, C_{OH} is the water concentration, d is grain size, Q is the activation energy, p is the lithostatic pressure, Ω is the activation volume, R is the constant for ideal gasses, T is the temperature and n, r and m are experimentally derived exponents. To yield an expression independent ofthe grain size, we assume $m = 0$ and $n > 1$ (Karato & Jung, 2010; Hirth & Kohlstedt, 2004).

From this configuration of the subduction fault, we make a meshed subduction system (Supplementary Figure 6.1a) to run a numerical model of the subduction seismic cycle. We discretize the system into a triangular mesh of 857 cells with a size of 20 km (Supplementary Figure 6.1a), while the points elements at the fault are separated by 200 m along the Slab2 geometry (Hayes et al., 2018), allowing numerical convergence. Deformation at each triangle is computed considering a Burger'sassembly where the total anelastic strain rate is given by $\varepsilon_T = \varepsilon_M + \varepsilon_K$,in which ε_M and ε_K are the instantaneous strain rates in the Kelvin and Maxwell elements, respectively (Masuti et al., 2016). Power-creep law parameters for the oceanic and continental mantle (Supplementary Table 6.2) are assumed following previous experimental works and simulations (Karato & Jung, 2010; Hirth & Kohlstedt, 2004). We used the numerical code Unified Cycle of Earthquakes (UniCyclE) that employs the integral method (Barbot, 2020; Barbot et al., 2017; Muto et al., 2019), including surface and volume elements. The changes in fault traction will depend on the surrounding fault slip and distributed strain. We assume a background strain rate in the horizontal direction of $\varepsilon = -1x10^{-14}$ s^{-1} and predefine a set of synthetic GNSS stations at the surface of our mesh to compare those results with the actual data.

2.6.2 Temperature model

The subduction thermal model is constructed considering an oceanic slab subducting with a kinematically prescribed velocity (66 mm per year) (Marota et al., 2013) beneath a fixed and layered continental plate. We use the continental lithospheric structure of Tassara & Echaurren (2012) considering an upper and lower crust, an oceanic crust and a continental and oceanic mantle. In this framework, the downgoing slab drives

flow within the overlying viscous mantle wedge. Velocity and pressure at the mantle wedge are found by solving the equations of mass and momentum conservation. Following van Keken (2008), we solve the equation of conservation of mass:

$$\nabla \cdot \mathbf{v} = 0 \qquad \text{eq. 2.8}$$

and the conservation of momentum:

$$\nabla \cdot \boldsymbol{\tau} - \nabla P = 0 \qquad \text{eq. 2.9}$$

where v is velocity, τ is the deviatoric stress tensor and P is the dynamic pressure. The deviatoric stress tensor is given by:

$$\boldsymbol{\tau} = 2\eta\dot{\boldsymbol{\epsilon}} \qquad \text{eq. 2.10}$$

in which η is the effective dynamic viscosity and the components of the strain rate tensor $\dot{\varepsilon}$ are:

$$\dot{\varepsilon}_{ij} = \frac{1}{2}\left(\frac{\partial v_i}{\partial x_j} + \frac{\partial v_j}{\partial x_i}\right) \qquad \text{eq. 2.11}$$

We assume that viscosity is obtained by dislocation creep:

$$\eta = Aex\,p\left(\frac{Q}{nRT}\right)\dot{\varepsilon}^{\frac{1-n}{n}} \qquad \text{eq. 2.12}$$

where the rheological parameters are the same as in equation 2.7. We consider a temperature- and stress-dependent wet olivine rheology for the mantle wedge (Karato & Jung, 2010). The boundary conditions for mantle wedge are (1) no slip below the rigid overriding plate and (2) constant velocity with a value equal to plate convergence along the top of the slab and below the maximum decoupling depth (Peacock & Wang, 2021). The thermal field within the entire subduction zone is computed by solving the steady-state heat advection–diffusion equation, so temperature is obtained by solving:

$$\rho c_p(\mathbf{v} \cdot \nabla)T = \nabla \cdot (k\nabla T) + f \qquad \text{eq. 2.13}$$

in which ρ is density, c_p is the specific heat, k is thermal conductivity and f is a parameter that describes possible heat sources. To solve the system, we assume a constant temperature at the surface of the model (0 °C) and at the bottom of the oceanic lithosphere (1,450 °C). On the slab inflow boundary, we prescribe a geotherm obtained using a half-space cooling model (Turcotte & Schubert, 2014) considering an age of 14 million years ago (Tebbens & Cande, 1997). At the right edge of the model, we assume a conductive geotherm calculated using the thermal properties of (Supplementary Table 6.3), which is then applied along the landward boundary of the overriding plate. Along the inflow part of the wedge, we prescribe a geotherm that is obtained using an adiabatic gradient of 0.4 °C km^{-1} and a mantle potential temperature of 1,300 °C. For the outflow boundary of the wedge, zero heat flux is assumed.

Finally, we solve equations 2.8, 2.9 and 2.11 using a stabilized finite element (Araya et al., 2023) that allows us to use equal order of polynomial interpolation at each unknown point.

2.6.3 Pressure and temperature path

To compute the pressure–temperature path, we use the lithospheric structure of (Tassara & Echaurren, 2012), and we take the average density structure of (Tassara, 2010). We compute the vertical stress with:

$$\sigma_v = g\rho h \qquad \text{eq. 2.14}$$

where g is the gravity acceleration constant, ρ is density and h is the thickness of the lithospheric layer (upper crust, lower crust and lithospheric mantle). Then, we compute the normal component over each element of the fault surface to obtain the $\bar{\sigma}$. By combining the temperature distribution at the plate interface and the σ_v over it, we obtain the pressure–temperature path from (Supplementary Figure 6.1b).

2.6.4 Coseismic slip model

We invert the coseismic slip for the dip direction using the uplift displacements on the surface from the work of (Plafker & Savage, 1970) in between 42° S and 45° S. To find the solution, we apply the Bayesian inversion approach of (Becerra-Carreño et al., 2022), which allows us to obtain positive model parameters and associated uncertainties. This constraint allows us to obtain a more realistic slip solution as the slip direction is positive with respect to the dip direction, given the subduction stress regime. We impose a slip solution to be a multivariate folded normal distribution, and simultaneously we seek to find a solution for $Gm = d$, where d is the deformation data, m is the backslip on each subfault in the plate contact and G is the matrix which contains the Green's functions. The Bayesian formulation is given by:

$$p(\mathbf{s}|\mathbf{d}, H) = \frac{p(\mathbf{d}|\mathbf{s})p(\mathbf{s}|H)}{p(\mathbf{d}|H)} \qquad \text{eq. 2.15}$$

with

$$p(\boldsymbol{s} \mid H) = (2\pi)^{-\frac{N_m}{2}}|\boldsymbol{S}|^{-\frac{1}{2}}exp\left[-\frac{1}{2}(\boldsymbol{s}_p - \boldsymbol{s})^T\boldsymbol{S}^{-1}(\boldsymbol{s}_p - \boldsymbol{s})\right] \qquad \text{eq. 2.16}$$

$$p(\boldsymbol{d} \mid \boldsymbol{s}) = (2\pi)^{-\frac{N_d}{2}}|\boldsymbol{D}|^{-\frac{1}{2}}exp\left[-\frac{1}{2}(\boldsymbol{d} - \boldsymbol{G}\boldsymbol{s})^T\boldsymbol{D}^{-1}(\boldsymbol{d} - \boldsymbol{G}\boldsymbol{s})\right] \qquad \text{eq. 2.17}$$

To enforce positivity constraints on the model parameters, we impose the following changes of variables:

$$\mathbf{m}(\mathbf{s}) = (|s_1|, |s_2|, \dots, |s_m|)^T \qquad \text{eq. 2.18}$$

which guarantees us a positive solution and results in a folded normal distribution in the posterior distribution. We use the maximum evidence criteria to perform Bayesian model selection, namely, to search for the hyperparameters of a particular hypothesis H. D and S are the covariance matrices of the likelihood and prior, respectively. The mean of the prior is s^p. We then obtain the correlation between the slip parameters based on the information of the same data.

Data availability

The GPS data that support the findings of this study are available in the GNSS data repository of the Centro Sismológico Nacional, Chile (http:// gps.csn.uchile.cl/data/). Uplift data after the Valdivia earthquake can be found at Plafker & Savage (1970) (https://doi.org/10.1130/0016-7606(1970)81[1001:MOT CEO]2.0.CO;2). Data of intertidal biotic indicators were obtained from (Garrett et al., 2019) (https://doi.org/10.1785/0120180173). Thermal model, coseismic slip model and quasi-dynamic input files to be run using UniCycle are uploaded to https://doi.org/10.5281/zenodo.8435744. Specific results from the quasi-dynamic simulations are available from the corresponding author upon reasonable request.

Code availability

Quasi-dynamic simulations were computed using the code Unicycle (Barbot 2018, 2020) (https://bitbucket.org/sbarbot/unicycle/src/master/). The code to process quasi-dynamic results is available from the corresponding author upon reasonable request.

Acknowledgements

This work is supported by the National Agency of Research and Development (ANID-Human Resources Branch/National Doctorate/2021) (J.J.), the Millennium Scientific Initiative (ICM) grant NC160025 'CYCLO—the seismic cycle along subduction zones' (A.T., J.J.). R.A. acknowledges funding from the Centro de Modelamiento Matemático (FB210005) of the PIA Program: Concurso Apoyo a Centros Científicos y Tecnológicos de Excelencia con Financiamiento Basal (ANID-Chile). S.B. acknowledges funding from the National Science Foundation under award number EAR-1848192. J.G.F.C. has been supported by Centro de Investigación para la Gestión Integrada del Riesgo de Desastres (CIGIDEN), Agencia Nacional de Investigación y Desarrollo (ANID)/Fondo de Financiamiento de Centros de Investigación en Áreas Prioritarias (FONDAP)/1522ª0005 and acknowledges support from ANID/Fondo Nacional de Desarrollo Científico y Tecnológico (FONDECYT)/11201180. M.M. acknowledges support from ICN12019N Instituto Milenio de Oceanografía and FONDECYT 1221507 and CIGIDEN (FONDAP)/1522ª0005.

References

The list of references cited at this chapter is part of the section **Main references** at page 119.

3 Impact of Upper-Plate Faulting on Foreshocks: Insights from the 2014 Iquique Earthquake

J. Julve[1], M. Moreno[2], S. Barbot[3], A. Tassara[1].

[1]Universidad de Concepción, Earth Science Department.

[2]Pontifical Catholic University, Structure and Geotechnical Engineer Department.

[3]University of Southern California, Earth Science Department.

The third chapter corresponds to the second paper developed during this thesis. It was submitted to Geophysical Research Letters on June 26th, 2024, and it is currently being reviewed.

Abstract

The role of upper-plate faulting in the seismic cycle of large megathrust earthquakes remains poorly understood. We use quasi-dynamic numerical simulations of multiple seismic cycles to analyze the interaction between crustal faulting and the foreshock sequence of the 2014 Iquique (Mw 8.2) earthquake in Northern Chile. Multi-cycle models incorporating upper-plate faulting align better with coseismic displacements, replicating events akin to the Iquique earthquake. Upper-plate faulting significantly influences foreshock seismicity and deformation patterns. By calibrating the average hydraulic state—varying the effective normal stress—along the megathrust with pre-earthquake seismicity, we find that lower pore pressure ratios result in more seismicity before the mainshock. This implies that the hydraulic state of the megathrust is critical for foreshock activity. This comprehensive modeling approach underscores the importance of the mechanical interplay between the megathrust and upper-plate faults in precursory sequences of large subduction zone earthquakes.

Plane Language Summary

Active upper-plate faults in subduction zones worldwide have shown activity before, during, and after large earthquakes, suggesting a mechanical link to megathrust

behavior. Advancing our understanding of these mechanisms is essential for enhancing seismic hazard assessment. The 2014 Iquique earthquake (Mw 8.2) in Northern Chile is probably the best-documented earthquake in terms of pre-earthquake upper-plate activity, characterized by an intense foreshock sequence 15 days before the main event. Here, we utilize quasi-dynamic numerical simulations of multiple seismic cycles (several thousand years) to analyze the interaction between crustal faulting and foreshocks preceding events similar to the 2014 Iquique earthquake. Upper-plate faults in our models significantly influence the seismic activity prior to the mainshock and are key to achieving a coseismic slip distribution that induces surface displacements consistent with geodetic observations. Additionally, we find that by decreasing the pore pressure ratio within the megathrust down to 0.8, we consistently increase the foreshock activity. This research underscores the importance of considering both the mechanical interactions between faults and the role of fluid dynamics in understanding and characterizing seismic cycles in subduction zones.

3.1 Introduction

Upper-plate faults occupy the accretionary prism of worldwide subduction zones (e.g., Park et al., 2002; Melnick et al., 2012), showing evidence of synchronized activity with the basal megathrust (e.g., Barnes et al., 2002; Wilson et al., 2006; Melnick et al., 2009; Schurr et al., 2014), as observed before (Schurr et al., 2014; Hayes et al., 2014), during (Melnick et al., 2012; Herman et al., 2023), and after great subduction zone earthquakes (Farias et al., 2011; Kato et al., 2011; Fukushima et al., 2018). The mechanical coupling between the megathrust and offshore upper-plate faults produces transient slip manifesting as earthquake clusters and aseismic slip (Ruiz et al., 2014), and enhances tsunami excitation in the outer wedge (Qiu & Barbot, 2022). However, the mechanisms controlling the triggering, delay, and size of earthquakes among upper-plate faults fracturing the outer wedge are still poorly understood. Dynamic models suggest that the permanent deformation of the upper plate accrues throughout the seismic cycle (van Dinther et al., 2014; Sathiakumar & Barbot, 2020; van Zelst et al., 2022; Sathiakumar et al. 2024). The deformation of the forearc structures may

redistribute stress and pore fluid pressure (Wang et al., 2019), affecting megathrust dynamics.

On April 1st, 2014, a moment magnitude (Mw) 8.1 megathrust earthquake struck the subduction zone in Northern Chile close to Iquique (Fig. 1a). The mainshock was preceded by a slow-slip event triggered 8 months before (Socquet et al., 2017), and by a sequence of significant foreshocks that initiated on March 16th, 2014, including a Mw 6.7 event that ruptured an offshore W-dipping upper plate fault (Bedford et al., 2015; González et al., 2015, Ruiz et al., 2014, Schurr et al., 2014; Soto et al., 2019) (Fig. 1a, b). The seismicity pattern before the earthquake exhibited migration towards the up-dip portion of a locked region within the plate interface (Schurr et al., 2020; Socquet et al. 2017), indicative of a mechanical interaction between an offshore W-dipping fault in the eastern limit of the outer wedge and the megathrust (Herman et al., 2016; Schurr et al., 2020). Changes in the stress field that unclamped the plate interface has been proposed (González et al., 2015; Herman et al., 2016), followed by the northward migration towards the plate interface driven by aseismic slip (Meng et al., 2015; Ruiz et al., 2014).

Offshore upper-plate crustal faults, akin to those observed in Chile, are documented in Japan (Moore et al., 2007; Kamei et al. 2012; Kodaira et al., 2017), Cascadia (Watt and Brothers, 2020), Sumatra (Singh et al. 2008; Hananto et al. 2020), Java (Kopp et al., 2009), the Philippines (Zhu et al. 2013), Sunda (Lüschen et al., 2011), the Aleutians (Miller et al., 2014; von Huene et al., 2016), and New Zealand (Barker et al., 2009) subduction zones. They have been also inferred from outcrops of paleo-subduction zones in the central European Alps (Dielforder et al., 2015). Recent studies have focused on the influence of mechanical and rheological properties on megathrust seismicity (e.g., Li & Liu, 2016; Li & Liu, 2017; Barbot, 2020; Oncken et al., 2021; Shi et al. 2022). However, understanding the influence of hanging-wall structures on megathrust seismicity remains a recondite problem.

Here, we employ quasi-dynamic numerical simulations of multiple seismic cycles to examine the mechanical interactions between a W-dipping offshore upper-plate fault

and the megathrust, resembling the structural context of the Iquique 2014 earthquake. Due to the influence of the geological structure on the seismicity at subduction zones (Julve et al., 2024), we establish a two-dimensional modeling framework integrating geological and geophysical data to evaluate the mechanical impact of an active upper-plate fault on the initiation of large megathrust earthquakes. We compare our models with seismic activity during pre-seismic unrest phase of the Iquique sequence and with geodetic data during the coseismic displacement. Our analysis suggests that an offshore W-dipping upper-plate fault influences the precursory phase of megathrust earthquakes, where a reduction in pore pressure ratio within the seismogenic zone, drives foreshock activity.

3.2 Data and methods

3.2.1 Modeling upper-plate fault and megathrust earthquake cycles

We investigate how an offshore upper-plate fault influences megathrust earthquakes in Northern Chile, using 2D quasi-dynamic models to assess its impact on rupture and precursory activity in subduction zones. We estimate the evolution of slip-rate over time using a slip-rate- and state-dependent friction law in isothermal, isobaric conditions (Barbot, 2019a), using the UniCyclE code (Barbot, 2018; Barbot, 2020). We use the Slab2 (Hayes et al. 2018) model to constrain the megathrust geometry, while foreshock seismicity one month before the Mw 8.1 Iquique earthquake (Schurr et al., 2020), seismic line interpretations of the forearc structure (Storch et al., 2021), and the preferred orientation of nodal planes from the Mw 6.7 earthquake (Herman et al., 2016; Schurr et al., 2020) delineate the offshore fault (Fig. 3.1c). We determine the temperature distribution using a finite-element method (Araya et al., 2023), considering a stratified continental plate with constant thermal properties. See Supplementary Material 6.2.1 to 6.2.4 for details of the numerical model.

We infer the distribution of frictional parameters at the plate interface in Northern Chile based on geological and geophysical data. Our cross-section at 20°S incorporates subduction zone features by integrating seismic tomography, reflection profiles (Comte et al., 2016; Geersen et al., 2018; Sallarès & Ranero, 2005; Storch et al., 2021),

foreshock seismicity before the Mw 8.1 Iquique earthquake (Schurr et al., 2020), geodetic locking models (Li et al., 2015; Jolivet et al. 2020), and a new thermal model (Fig. 3.1b, Supplementary Material 6.2.4). The Northern Chile subduction zone has a thin sediment layer due to low erosion rates from hyper-arid conditions since the Upper Miocene (Carretier et al., 2018; Kober et al., 2007), leading to a narrow frontal accretionary prism of 5 to 30 km in the outer wedge (Geersen et al., 2018; Maksymowicz et al., 2018) (Fig. 3.1c). Seismicity (Schurr et al., 2020; Sippl et al., 2023; Soto et al., 2019) and locking models (Li et al., 2015; Jolivet et al., 2020) indicate frictional instability along the megathrust from 17 to 60 km depth. The outer wedge shows intense faulting and high V_p/V_s ratios, suggesting a high-fluid zone (Petersen et al., 2021, Fig. 3.1d).

Basaltic rocks from the Nazca plate control megathrust frictional behavior above the continental Moho (Tassara & Echaurren, 2012) (Fig. 3.1b). We use mean a and b values (Supplementary Material 6.2.1, eq. (1)) from basalt gouge experiments (Zhang et al., 2017) (Fig. 3.1b). The megathrust shows velocity-strengthening below the outer wedge (< 100°C) and velocity-weakening between the inner wedge and the Coastal Cordillera (100°C – 300°C, Fig. 1b-c), defining a seismogenic zone with locking degree ≥ 0.5. At greater depths, V_p/V_s ratios indicate serpentinization in the cold mantle wedge (Comte et al., 2016). We assume serpentinites control the fault core's behavior, using the values of the frictional parameters a and b from lizardite and antigorite experiments (Moore & Lockner, 2011; Okazaki & Katayama, 2015; Takahashi et al., 2011), resulting in velocity-strengthening below the Central Depression (Fig. 3.1b-c). The frictional parameters are summarized in Supplementary Material Table 6.5.

We compute the effective normal stress $\bar{\sigma}_n = (1-\lambda)\sigma_n$, assuming an average background pore fluid pressure ratio $\lambda = 0.825$. This value closely aligns with the mean value explaining strain rates observed in the fabric of rocks in paleo subduction zones, ranging between brittle creep and solution precipitation creep as deformation mechanisms (Oncken et al., 2021). This assumption is also consistent with values obtained from Coulomb wedge theory, considering that λ remains constant between the wedge and the megathrust (Adam & Reuther, 2000; Wang & Hu, 2006). With these

assumptions, we get the continuous down-dip distribution of $\bar{\sigma}_n$ shown in Fig. 3.1b. The outer and inner wedge regions exhibit background and foreshock seismicity, indicating a highly fractured environment (Herman et al., 2016; Soto et al., 2019; Storch et al., 2021, Fig. 3.1d), with densities consistent with a mafic composition (Sallarès & Ranero, 2005; Tassara and Echaurren, 2012). Sedimentary sequences are primarily confined to the poorly developed frontal accretionary prism and the slope of the forearc wedge (Geersen et al., 2018). Based on geophysical and geological data, we infer that the offshore crustal fault related to the foreshock sequence cut through mafic rocks of the upper crust. The minimum depth of foreshock and background seismicity indicates velocity weakening behavior below 5 km. We assume the same a and b values as those used for the seismogenic megathrust (Fig. 3.1b), ignoring the sedimentary cover below the middle and lower slopes. We choose a value of L (Fig. 3.1b) that allows to solve the nucleation size on both faults capturing the seismicity of the seismic cycle.

We compute the effective normal stress $\bar{\sigma}_n = (1-\lambda)\sigma_n$, assuming an average background pore fluid pressure ratio $\lambda = 0.825$. This value closely aligns with the mean value explaining strain rates observed in the fabric of rocks in paleo subduction zones, ranging between brittle creep and solution precipitation creep as deformation mechanisms (Oncken et al., 2021). This assumption is also consistent with values obtained from Coulomb wedge theory, considering that λ remains constant between the wedge and the megathrust (Adam & Reuther, 2000; Wang & Hu, 2006). With these assumptions, we get the continuous down-dip distribution of $\bar{\sigma}_n$ shown in Fig. 3.1b. The outer and inner wedge regions exhibit background and foreshock seismicity, indicating a highly fractured environment (Herman et al., 2016; Soto et al., 2019; Storch et al., 2021, Fig. 3.1d), with densities consistent with a mafic composition (Sallarès & Ranero, 2005; Tassara and Echaurren, 2012). Sedimentary sequences are primarily confined to the poorly developed frontal accretionary prism and the slope of the forearc wedge (Geersen et al., 2018). Based on geophysical and geological data, we infer that the offshore crustal fault related to the foreshock sequence cut through mafic rocks of the upper crust. The minimum depth of foreshock and background seismicity indicates velocity weakening behavior below 5 km. We assume the same a and b values as those

used for the seismogenic megathrust (Fig. 3.1b), ignoring the sedimentary cover below the middle and lower slopes. We choose a value of L (Fig. 3.1b) that allows to solve the nucleation size on both faults capturing the seismicity of the seismic cycle.

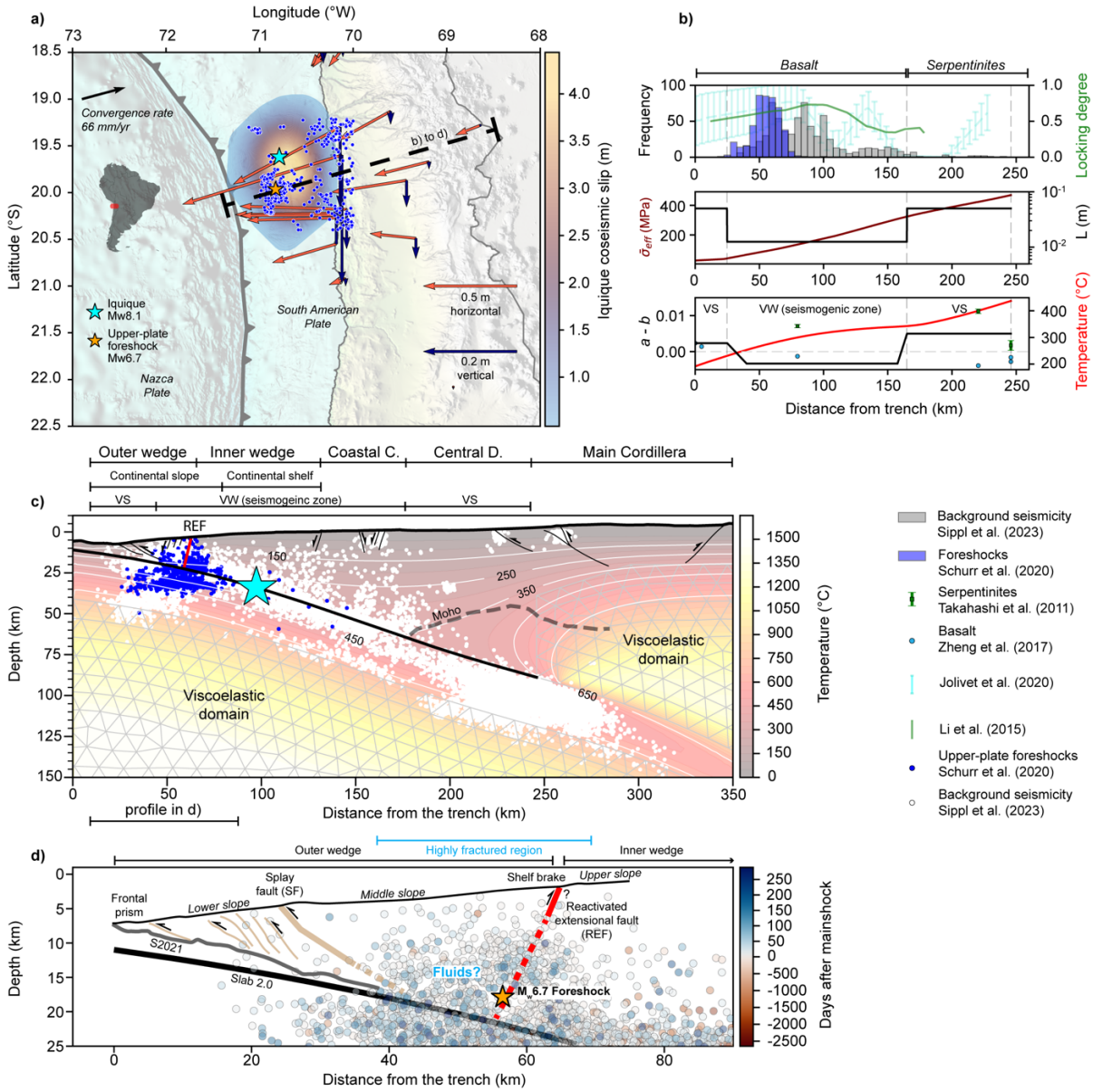

Figure 3.1. Tectonic setting, model structure, and forearc features. a) The 2014 Iquique earthquake rupture concentrated slip (Schurr et al., 2014). GNSS-derived displacements indicate consistent horizontal deformation towards the zone of maximum slip (red vectors) and coastal subsidence (black vectors). The foreshock sequence (blue dots) increased after the occurrence of a Mw 6.7 upper-plate fault earthquake (orange star) 15 days before the mainshock. The foreshocks and the mainshock epicenter (cyan star) surround the zone of maximum coseismic slip. b) Top: Distributions of background (gray) and foreshock (blue) seismicity and locking degree. Foreshocks in the histogram are filtered to show only those interpreted as interplate events. Center: Distribution

of parameters a and b, which frictionally segment the velocity-strengthening (VS) and velocity-weakening (VW) behavior of the megathrust. The slab temperatures from our thermal model and the rocks at the plate interface are shown. Bottom: Distributions of effective stress ($\bar{\sigma}_n$) and values of parameter L. c) White and blue dots are background and foreshock seismicity. Coastal C. = Coastal Cordillera, Central D. = Central Depression. Upper-plate structure based on the works of Storch et al. (2021), Geersen et al. (2018), and Giambiagi et al. (2022). Dashed line is the Moho discontinuity from Comte et al. (2016). White contours are isotherms from our temperature distribution. Gray triangles represent the mesh of the viscoelastic domain. d) The faults in red and brown are interpreted according to Storch et al. (2021), from which we also obtained the bathymetry and the plate interface (line S2021).

3.3 Results

3.3.1 Slip mechanisms

We consider two end-member simulations. The first model (M1, Fig. 3.2a) assumes that the megathrust is the only active fault, while the second model (M2, Fig. 3.1d-2b) also incorporates a W-dipping offshore upper-plate fault with reverse kinematics resembling the structure activated during the foreshock sequence. For the megathrust, the loading rate $V_L = 67$ mm/yr comes from the relative convergence velocity (Fig. 3.1a). For the upper plate fault, we assume that this structure accommodates 20% of the local plate convergence (Sathiakumar et al. 2020), resulting in $V_L = 13.4$ mm/yr. Due to modeling constraints, we assume that the offshore W-dipping upper-plate fault has reverse kinematics throughout the subduction seismic cycle. Although dynamic models (Herrera et al., 2023) and Coulomb wedge theory (Wang et al., 2019; Wang & Hu, 2006) suggest that normal faulting can occur on westward-dipping structures during the coseismic phase, we focus on the latter part of the interseismic phase before the Iquique-like earthquakes, where a reverse mechanism is expected as shown by the Mw 6.7 upper-plate event on March 15th, 2014. Each simulation spans 5,000 years, with the initial 3,000 years disregarded to mitigate the influence of initial conditions.

In both M1 and M2 simulations, the seismic cycles exhibit a series of earthquakes with different rupture lengths (Fig. 3.2), showing full ruptures extending from the down-dip limit of the seismogenic zone up to the trench, and partial ruptures occurring at the upper and lower parts of the velocity weakening region (Fig. 3.2a-b). Each partial earthquake is followed by a sequence of aftershocks located at the tip of each rupture, which then cascade into a new event, thus leading to a precursory phase for another

earthquake (Fig. 3.2a-b). The upper portion of the megathrust seismogenic zone experiences extended periods of acceleration, which in some cases can be classified as slow-slip events ($10^{-8} < V < 10^{-7}$ m/s), lasting decades before a new partial earthquake occurs (Fig. 3.2a-b). This acceleration is accompanied by either pulse-like (Fig. 3.2a) or progressive (Fig. 3.2b) unlocking of the velocity-weakening segment. The down-dip area is characterized by intense seismicity, represented by foreshock sequences that last hundreds of years, limiting the size of the subsequent down-dip partial ruptures (Fig. 3.2a-b).

In simulation M1, a super cycle of partial and full ruptures lasts approximately 800 years (Fig. 3.2a), while in M2, the duration spans around 750 years (Fig. 3.2b). To determine the magnitude of these events, we employ a scaling law that correlates the maximum coseismic slip (MCS) with Mw (Brengman et al., 2019). We recover the maximum slip of each event reaching a slip rate larger than 1 mm/s (Fig. 3.2a-b). For M1 and M2, the MCS of full ruptures reaches maximum values of 54.9 m and 52.2 m, respectively. We then apply (Brengman et al., 2019):

$$M_w = 6.3574 + 1.5439 \times log(MCS) \qquad \text{eq. 3.1}$$

As a result, a Mw 9 is obtained for both cases, consistent with estimations of the magnitude of the last giant earthquake in 1877 (Mw > 8.5) (Vigny & Klein, 2022). For the up-dip partial earthquakes, the rupture process initiates at the up-dip limit of the foreshock activity (Fig. 3.2e-f) and then propagates up to the boundary of the velocity-strengthening region and down to a point within the seismogenic zone (Fig. 3.2e-f), resembling the Mw 8.1 Iquique earthquake. Both up-dip and down-dip foreshock sequences are accompanied by aseismic slip, accelerating the fault within the rupture length (Fig. 3.2c-f). Upon initiation, the earthquake rupture front progresses towards the up-dip limit between the velocity-weakening and velocity-strengthening regions, ultimately diffusing at that boundary (Fig. 3.2e-f). Applying eq. 3.1, the maximum simulated partial earthquakes in M1 reach MCS = 9.2 m and Mw 7.8, while in M2 MCS = 11.9 m and Mw 8.0 (Fig. 3.3e-f).

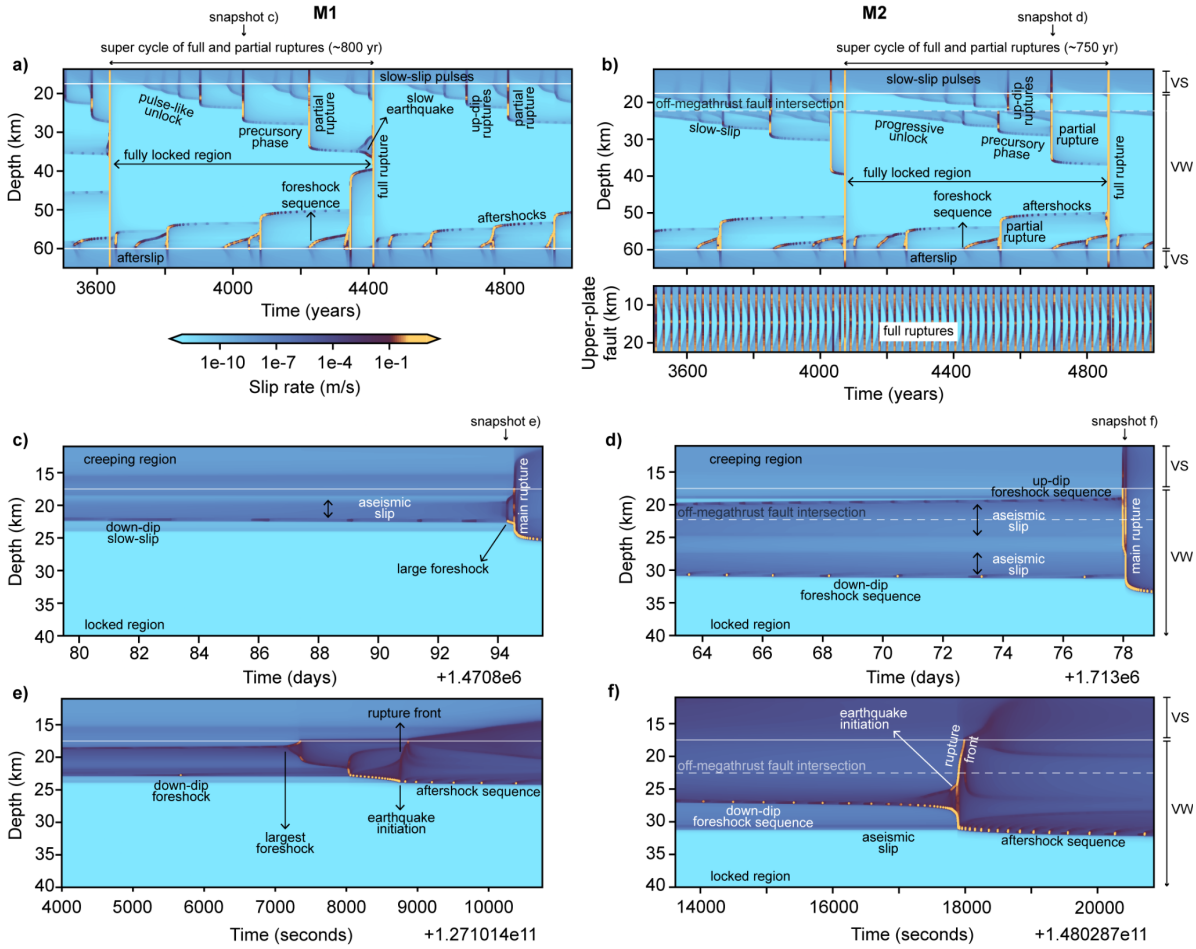

Figure 3.2. Slip-rate over time and rupture styles over 1,500 years of seismic cycle. a) Supercycle of full and partial ruptures for M1. Yellow lines represent a megathrust earthquake. White lines are the limits of the velocity weakening (VW) region defined in Fig. 1b. The supercycle lasts 800 years. Full ruptures are the ones that break from the trench up to the down-dip velocity strengthening (VS) area. Partial ruptures break a portion of the velocity-weakening region and can be nucleated at the up-dip or down-dip limit within the seismogenic zone. b) Same as in a) but for M2. In the bottom panel of b) we present the evolution of slip-rate in the upper-plate fault at the same time as in the megathrust. c) and d) describe the slip-rate and seismic activity 16 days before each mainshock, while e) and f) show the same but before 2 hours of the main rupture.

Both models exhibit similar rupture patterns (Fig. 3.2a-b) that arise from the elevated Dieterich-Ruina-Rice number R_u (Barbot 2019b) that controls the importance of non-local stress transfer and results from the frictional configuration and the geometry of the system. In our modeling, the megathrust has a minimum value of $R_u = 195.3$ within the velocity weakening region, which is associated with down-dip and up-dip partial ruptures, and full rupture of the seismogenic zone (Barbot, 2019b). In addition, M2 shows a clear influence of the upper-plate fault on the precursory activity prior to the

main partial rupture (Fig. 3.2d, f), developing a combination of aseismic slip and foreshock seismicity at the megathrust weeks before the mainshock. Given the assumed R_u number, up-dip partial events in Northern Chile may be linked to the gouge composition at the plate interface and to the length of the seismogenic zone, factors known to affect the rupture style and recurrence patterns within the velocity-weakening region (Barbot, 2019b; Nie & Barbot, 2022).

Eventually, after a continuous increase in aseismic slip in the up-dip region, the upper-plate fault (Fig. 3.2b) breaks in its full length during seismic ruptures that repeat approximately every 11 years, with MCS = 0.403 m and Mw 5.8. Due to computational limitations, our modeling does not use small enough values of L ($L < 10^{-3}$ m/s) to generate smaller ruptures, preventing us from representing the full spectrum of seismic activity within the upper-plate fault. As a result, we are unable to capture the complete foreshock sequence of small-sized seismicity observed before the Iquique mainshock.

3.3.2 Surface deformation

To verify our results with observations, we compute the root mean squared error (RMSE) between GNSS-derived displacements (see Supplementary Material 6.2.5) and our modeling outputs in two cases: first, comparing the coseismic displacement from the GNSS data with the simulated surface deformation ($RMSE_{GNSS}$ Fig. 3.3e-f); and second, assessing the combined difference between GNSS data plus coseismic slip (Schurr et al., 2014, Duputel et al. 2015) against the same model results ($RMSE_T$ Fig. 3.3e-f). In both cases, M2 exhibits a better fit to the data compared to M1 (Fig. 3.3), suggesting that Iquique-like events are better explained when an offshore upper-plate fault is active and mechanically coupled with the megathrust.

M1 generates two families of partial ruptures: the first with no more than 0.5 m of surface deformation in the east and vertical components, and the second with greater deformation, reaching 2 m of westward motion and 1.5 m of coseismic uplift offshore, along with 1.25 m of subsidence close to the coast (Fig. 3.3a, c). The $RMSE_T$ = 2.51 m with a maximum slip of 9.2 m (Fig. 3.3e).

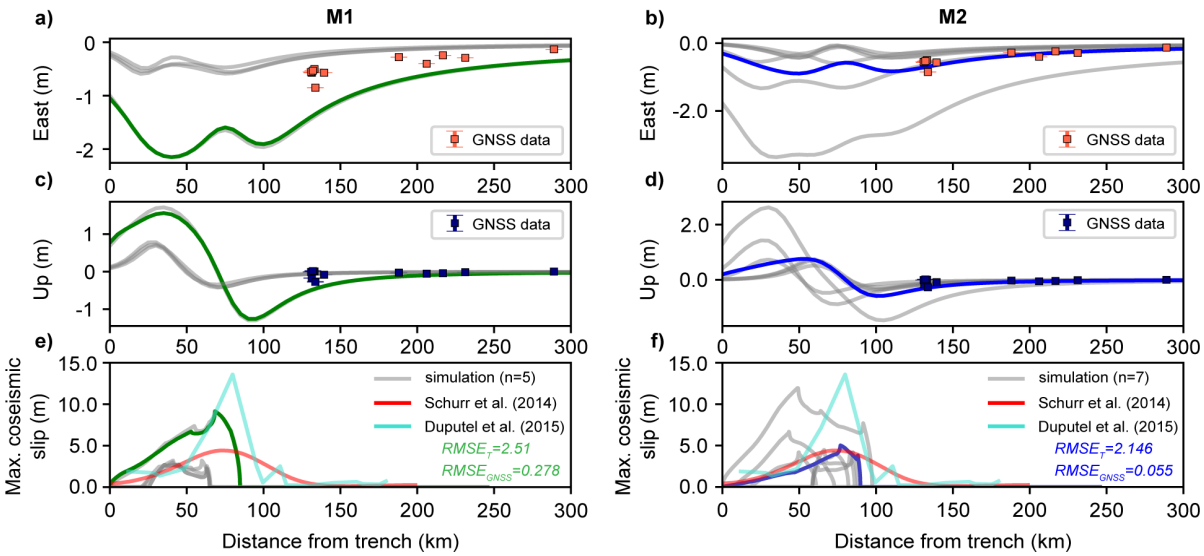

Figure 3.3. GNSS data and kinematic coseismic slip model of Iquique earthquake, against models results. In both M1 and M2, blue and green lines represent the partial rupture event with lowest $RMSE_T$ from each model. The n value represents all the simulated partial ruptures from each model. a) and b) show the East component of coseismic deformation for the Iquique earthquake in orange squares, and the same component of deformation for the simulated partial ruptures in gray and colored lines. c) and d) show the vertical component of the coseismic deformation of the Iquique earthquake in blue squares, and the same component of deformation for the simulated partial ruptures in gray and colored lines. e) and f) show two different coseismic slip models for the Iquique earthquake from Schurr et al. (2014) and Duputel et al. (2015), and all the simulated coseismic slips from the partial ruptures generated by the model.

M2 also exhibits two families of partial ruptures. Larger events reach a maximum of 2.5 m and 3 m of offshore uplift and westward motion respectively, with coastal subsidence of 1.9 m. The event with the lowest $RMSE_T$ (blue line Fig. 3.3b, d, f) shows 0.8 m of westward motion and offshore uplift, with coastal subsidence of 0.7 m (Fig. 3.3b, d). The coseismic slip has a maximum of 5 m, which is the same value obtained by Schurr et al. (2014), but lower than the 13 m estimated by Duputel et al. (2015) (Fig. 3.3f). In M2, the event with maximum coseismic slip is close to the results obtained by Duputel et al. (2015) and has a Mw closer to the 2014 Iquique earthquake. Also, it reproduces better the position of the rupture termination close to 100 km from the trench (Fig. 3.3f). As slip arrest occurs within the velocity weakening segment, we suggest that it is caused by the increasing value of $\bar{\sigma}_n$ (Fig. 3.1b), leading to a sequence of aftershocks at the end of the rupture once the earthquake reaches its maximum propagation (Fig. 3.2a-f, 3.3e-f).

3.3.3 Precursory activity and changes in effective normal stress

By computing the moment magnitude of each simulated foreshock (Fig. 3.2e-f), we compare the normalized cumulative seismicity one month before each partial rupture with the equivalent period before the Iquique event (Mw > 3, Fig. 3.4e). Our results indicate that offshore W-dipping upper-crust active faulting is not necessary to trigger an Iquique-like event, but its presence alters the precursory phase leading to the main rupture.

We select the simulated partial rupture with the lowest RMSE_T (blue and green lines Fig. 3.3) and estimate the coseismic slip of all the precursors within a 30-day time window to compute their Mw using eq. 3.1. We demonstrate that under identical parameters, when an offshore upper crustal fault is considered, M2 exhibits a higher cumulative foreshock count before the mainshock, generated by a burst of stress drop the month prior to the rupture (Fig. 3.4e, g). To analyze the full spectrum of seismicity, we select the data between 2013 and March 31st, 2014, from the catalog of Sippl et al. (2023). We identify the upper-plate events by computing the normal distance from each event with respect to the slab surface proposed in Sippl et al. (2023, Fig. 3.4a-d). During January and March of 2014, there was a sudden increase in upper-plate and interplate seismicity (Fig. 3.4a-d). In M2, to simulate that increase our results show that we have to decrease λ up to 0.825, increasing the density of foreshock seismicity (Fig. 3.4e). If λ is increased, then the density of foreshock seismicity will decrease below observations (Fig. 3.4e). We suggest that the mean hydraulic state at the megathrust does not feature high pore-fluid pressure at the last stage of the interseismic period, due to fluid migration to the upper plate (Fig. 3.4f), as the seismicity during the last 3 months prior to the mainshock indicate (Fig. 3.4a-d). The evolution of pore-fluid pressure will decrease $\bar{\sigma}_n$, reducing the nucleation size of simulated foreshocks (Barbot, 2019b; Lapusta & Liu, 2009; Rubin & Ampuero, 2005).

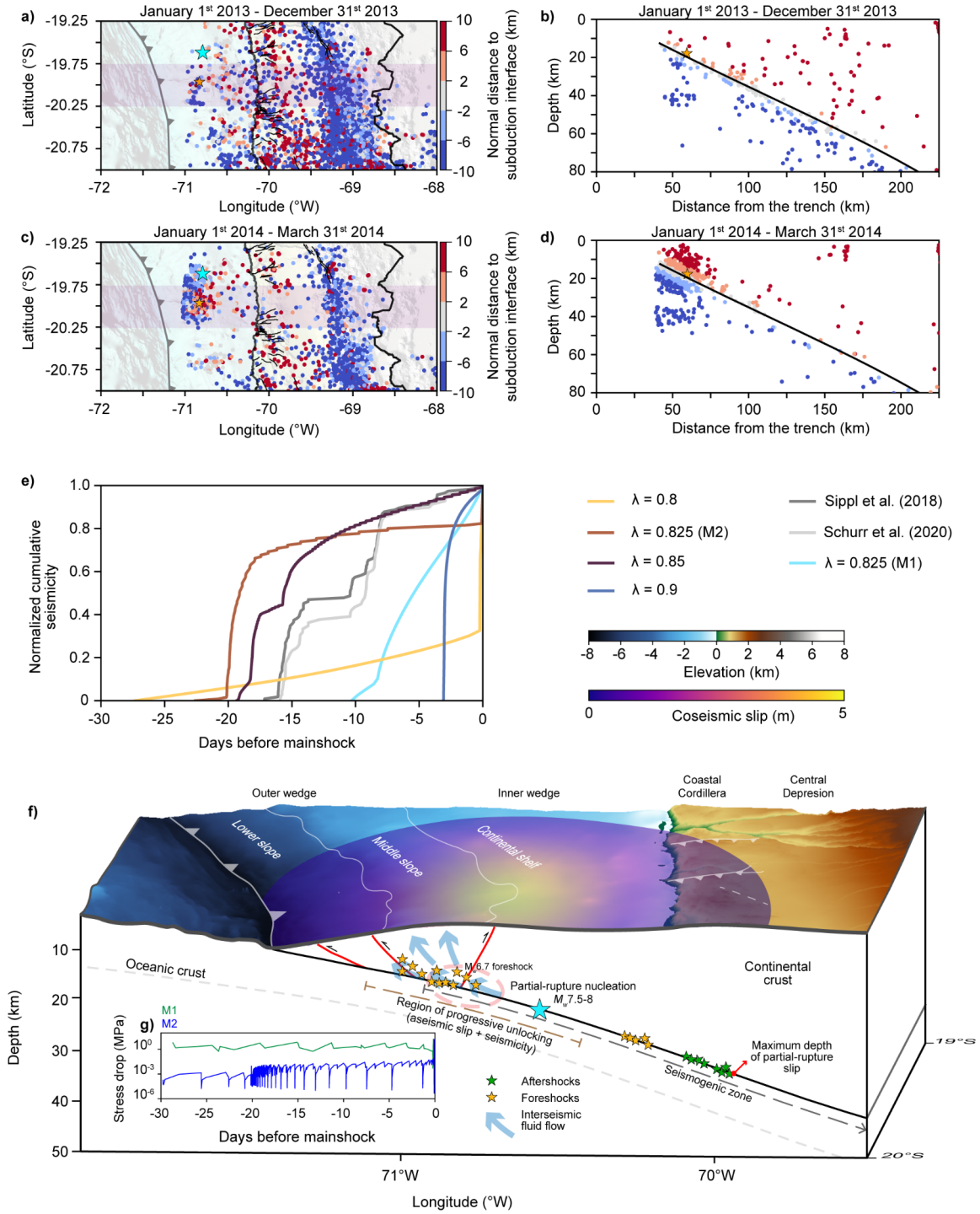

Figure 3.4. Foreshock seismicity and conceptual model. a) to d) correspond to the catalog of Sippl et al. (2023). The purple box represents the area at which we select the seismicity for cross sections in b) and d). e) foreshock seismicity is normalized for the total number of events before each mainshock. f) red dashed circle is the area in which we obtained the maximum stress that we use to compute the stress drop in g), and the colored ellipse in the surface is the coseismic slip model of Schurr et al. (2014).

3.4 Conclusions

By employing quasi-dynamic numerical models of the Northern Chile subduction zone, our study reveals the dynamic interplay between slip mechanisms induced by the interaction of the megathrust with W-dipping upper-plate faults located offshore in between the inner and outer wedge. Both full and partial ruptures exhibit distinct precursory phases characterized by foreshock seismicity and aseismic slip, followed by intense aftershock sequences. While the occurrence of up-dip partial earthquakes like the Iquique 2014 event is not directly influenced by upper-plate faulting, their presence significantly impacts the rate of foreshock seismicity and surface deformation patterns. Models integrating offshore upper-plate faults show better alignment with observed data, particularly in replicating events akin to the Iquique earthquake, underscoring the mechanical interaction between these structures and the megathrust. Furthermore, our exploration of changes in $\bar{\sigma}_n$ along the subduction zone demonstrates that lower values of λ increase foreshock activity before partial ruptures, providing valuable insights into the mean hydraulic state within the megathrust, which governs the initiation of seismicity culminating in large earthquakes. This study highlights the pivotal role of comprehensive modeling approaches in elucidating seismic hazard, emphasizing the significance of fluid-rock interactions in the latter stages of the interseismic phase during megathrust seismic cycles.

Acknowledgements

This work is supported by the National Agency of Research and Development (ANID-Human Resources Branch/NationalDoctorate/2021) (J.J) and by the FONDECYT project 1221507 (M.M.).

Open Research

The code for quasi-dynamic modeling – UniCyclE – can be found at: https://bitbucket.org/sbarbot/unicycle/src/master/. The input parameters for each simulation M1 and M2, the effective normal stress distributions used to model different scenarios of Fig. 4, the coseismic displacements derived from data of the GPS stations, the thermal model at 20°S, and the codes to process the output from UniCyclE (Figure 3) can be found at: https://doi.org/10.5281/zenodo.12615565. Foreshock seismicity was obtained from the work of

Sippl et al. (2018) (https://doi.org/10.1002/2017JB015384), Sippl et al. (2023) (https://doi.org/10.1016/j.jsames.2023.104326), and Schurr et al. (2020) (https://doi.org/10.1029/2020GL088351).

References

The list of references cited at this chapter is part of the section **Main references** at page 119.

4 Discussion

4.1 Geological control over the seismic cycle at the Chilean subduction zone.

Following eq. 1.1, changes in the rocks and sediments at the plate interface will impact the $a - b$ and μ values. In Chapter 2, it is shown that both parameters, specially $a - b$, will control not only the size of the earthquakes at the megathrust, but also the surface deformation after giant ruptures and at seismic cycle timescales. This mean that the amount of sediments being subducted will play a key role on the evolution of slip-rate and associated deformation in time. Laboratory experiments over synthetic fault gouges have also demonstrated that $a - b$ changes with temperature (e.g. Sawai et al., 2016, 2017). Minerals closely related with a high input of continental and marine sediments at the trench (phyllosilicates, quartz, feldspar, and carbonates), may have velocity weakening behavior (i.e. $a - b < 0$) below the 350°C isotherm, allowing rupture nucleation over different ranges of $\overline{\sigma_n}$ (Fig. 4.1). This feature arises new questions about which mineral within rocks and sediments being subducted, control the frictional behavior during the seismic cycle of megathrust earthquakes at Southern and Northern Chile.

Quasi-dynamic numerical simulations can be characterized by two non-dimensional parameters that will define the expected slip mechanism during the time of simulation, (1) the Dieterich – Ruina – Rice number (R_u) which depends on the rigidity moduli (G), on the width of the velocity weakening segment (W), on the effective normal stress ($\overline{\sigma_n}$), on the critical slip distance (L), and on the direct and evolutionary effects (a and b respectively), (2) and R_b that only depends on these last two values (Barbot, 2019b):

$$R_u = \frac{(b-a)\overline{\sigma_n}}{G}\frac{W}{L} \tag{4.1}$$

$$R_b = \frac{b-a}{b} \tag{4.2}$$

R_u controls the spectrum of fault slip, from periodic slow-slip events to aperiodic fast ruptures, while R_b governs the importance of transient weakening and strengthening effects (Barbot, 2019b).

Based on eq. 4.1 and 4.2, Figure 4.1 shows the values of R_u within certain ranges of $\overline{\sigma_n}$ and $a - b$. Over that grid, the values of $a - b$ obtained in laboratory experiments at varying $\overline{\sigma_n}$ conditions for different minerals and rocks –relevant at subduction zones– are plotted. The white contours represent the threshold values of R_u at which a new pattern of slip-mechanism arise during numerical modeling of planar faults in plane strain configurations (Barbot, 2019b). As was explained during Chapter 2, the Southern Chile subduction zone has a thick subduction channel (up to 1 km) filled with continental sediments of the last Pliocene glaciation. If we assume that the composition of those sediments is mostly from the North Patagonian Batholith, then the most likely minerals controlling the frictional regime at the subduction channel are quartz and phyllosilicates (smectite, illite, montmorillonite, etc.). While in Northern Chile, in Chapter 3 it was shown that there are almost no sediments at the trench, which means that the plate interface will be govern by the frictional behavior of the altered basalt from the subducted plate. Given its fractured state (Geersen et al., 2018), it may also host a large amount of fluids coming either from the ocean or from the hydrofracturing at the base of the upper plate (von Huene et al., 2004). To evaluate the influence of blueschist compositions during the seismic cycle, prograde metamorphism with depth is assumed. Stability fields from metapelites and altered basalts show that blueschist facies at plate interface start over 0.5 GPa and 200 °C (Condit et al., 2020), conditions that are met in both Northern and Southern Chile. In Chapter 2 and Chapter 3, we divided the megathrust in frictional segments governed by specific mineral compositions. Figure 4.1 show that not only quartz may develop large and giant megathrust earthquakes, but also blueschist. Another feature is that slow slip is more likely to happen under smectite and quartz compositions (Fig. 4.1). To evaluate this ideas, several new simulations that assumed the same parameters and geometries as in Chapter 2 and Chapter 3 are run but changing just the $a - b$ values at the seismogenic zone (Fig. 4.2 and Fig. 4.3).

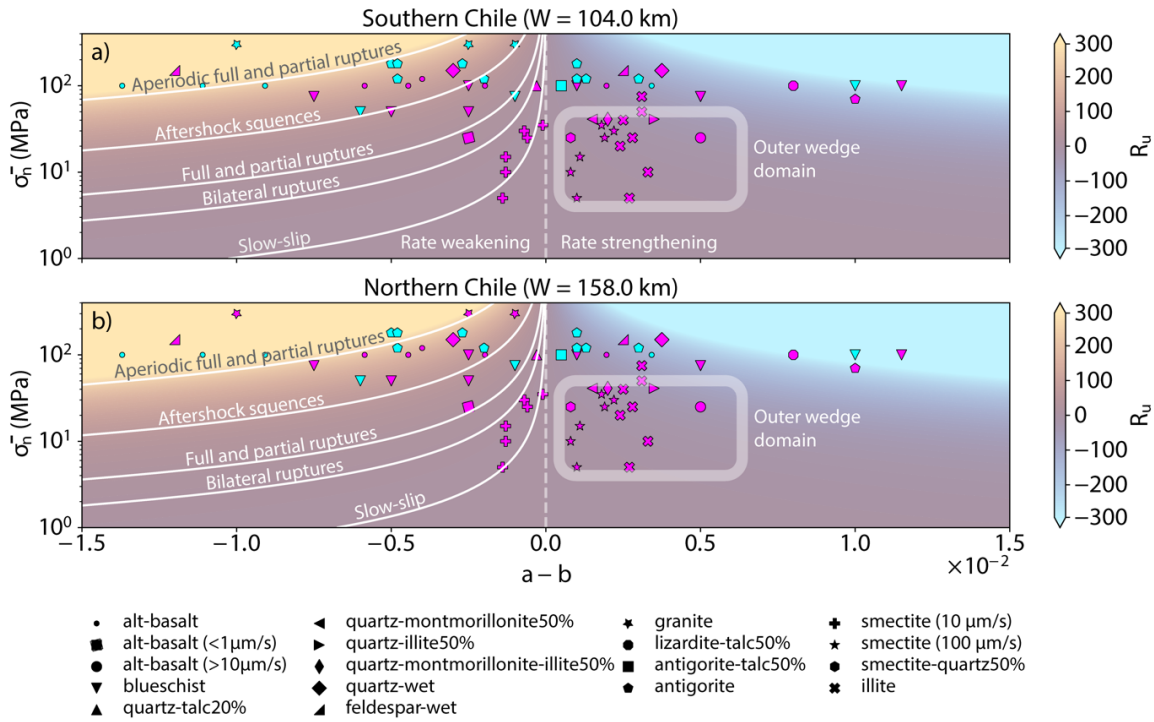

Figure 4.1. Frictional properties of relevant minerals over R_u values at Southern and Northern Chile. a) R_u values where calculated using eq. 4.1 and assuming 104 km for the width of the seismogenic zone (W), 1x10^{-2} m for L, and the respective $\overline{\sigma_n}$ and $a-b$ values of each axis. White contours are the approximate R_u values at which the simulations start to show a new slip mechanism (Barbot, 2019b). Magenta polygons are the minerals whose frictional properties are possible at the respective subduction zone, considering the thermal models of Chapters 2 and 3. Cyan polygons are the minerals whose frictional properties are not possible at the respective subduction zone. The frictional parameters of each mineral and its reference are in Supplementary Table 6.6. b) Same as a) but for Northern Chile and considering $W = 158$ km. Percentages values at each mineral represent the homogeneous mixture made for reproduce synthetic fault gouges on each laboratory experiment from where those values where obtained (Supplementary Material Table 6.6).

At Southern Chile, if smectite controls the frictional behavior within the megathrust, then no slip acceleration is observed, and the seismogenic zone creeps at slip-rates close to the convergence rate (Fig. 4.2a). Then, if the value of $a-b$ is decreased up to the one of quartz with 20% of talc and below the threshold of bilateral ruptures (Fig. 4.1), the simulations generate low-frequency pulses of acceleration (Fig. 4.2b) that can be considered as slow-slip events (SSE). Although no SSE has been observed at these latitudes yet, the assumed mineralogy at the subduction channel may allow its occurrence, specially up-dip. Continuing the exploration of $a-b$, values that are close to zero will be named as low rate-weakening, while those progressively decreasing towards negative values are high rate-weakening. Low rate-weakening behavior of

blueschist fault gouges (Fig. 4.1), generate full semi-periodic ruptures with low recurrence times (147 years, Fig. 4.2c), not reproducing paleoseismological observations in Southern Chile (Moernaut et al., 2018; Wils et al., 2020). Interestingly, the simulation also develops partial ruptures at the down-dip region, like the Mw 7.6 2016 Melinka earthquake, and up-dip partial ruptures which has not been instrumentally registered at these latitudes (Fig. 4.2c and Fig. 4.4c). Blueschist show even higher rate-weakening values of $a - b$, here used as an end member (Fig. 4.2d and Fig. 4.4d). This new model shows aperiodic patterns of full and partial ruptures with aftershock sequences, being consistent with the data in Fig. 4.1. Recurrence time of full ruptures is 357 years, reproducing the paleoseismological data (Moernaut et al., 2018; Wils et al., 2020). Few SSE are generated with blueschist compositions at the up-dip and down-dip limits of the seismogenic zone (Fig. 4.4c, d).

While blueschist metamorphism is reached close to 300°C in Southern Chile (Supplementary Material Fig. 6.1), quartz does not suffer major changes from this process, exhibiting brittle deformation up to 350°C. In Chapter 2, it was defined that quartz compositions control the seismic cycle in Southern Chile (Fig. 4.2e). Now, the effect of feldspars is also considered because they are major constituent within batholiths at North Patagonian Andes and altered basalts in the subducted plate (Fig. 4.2f). Wet quartz compositions show up-dip and down-dip partial ruptures, along with earthquakes that rupture the entire seismogenic zone. SSE and slow-earthquakes can be observed at the down-dip and up-dip area (Fig. 4.4e). Progressive unlocking occurs at the up-dip and down-dip limit of the seismogenic zone, which is sometimes accompanied by SSE (Fig. 4.2e). This supports the hypothesis of SSE occurring in Southern Chile but not being yet detected. Finally, wet feldspar simulation shows full and partial ruptures with aftershock sequences, similarly to high rate-weakening values of $a - b$ in blueschist (Fig. 4.2f and 4.2d respectively). Recurrence time for full ruptures is 357 years, agreeing with paleoseismic data in Southern Chile (Moernaut et al., 2018; Wils et al., 2020).

The simulations listed in Fig. 4.2 and Fig. 4.4 show that giant ruptures with high slip-rates (>10^{-1} m/s) and with recurrence time agreeing with observations require $a - b <$

$-7.5x10^{-3}$, which means that sediments filling the trench are controlled by feldspar and quartz compositions. When conditions of stable blueschist facies are met, those minerals also may control rupture nucleation at Southern Chile. This increases the potential of SSE in this segment, even not needing a decrease in $\overline{\sigma_n}$. Nevertheless, as it was shown in Chapter 2, regions of low $\overline{\sigma_n}$ at the down-dip region control the mechanical interaction between large and giant earthquakes, decreasing recurrence times of smaller ruptures nucleated at that depth compared to models with homogeneous λ as in Fig. 4.2d and Fig. 4.2f.

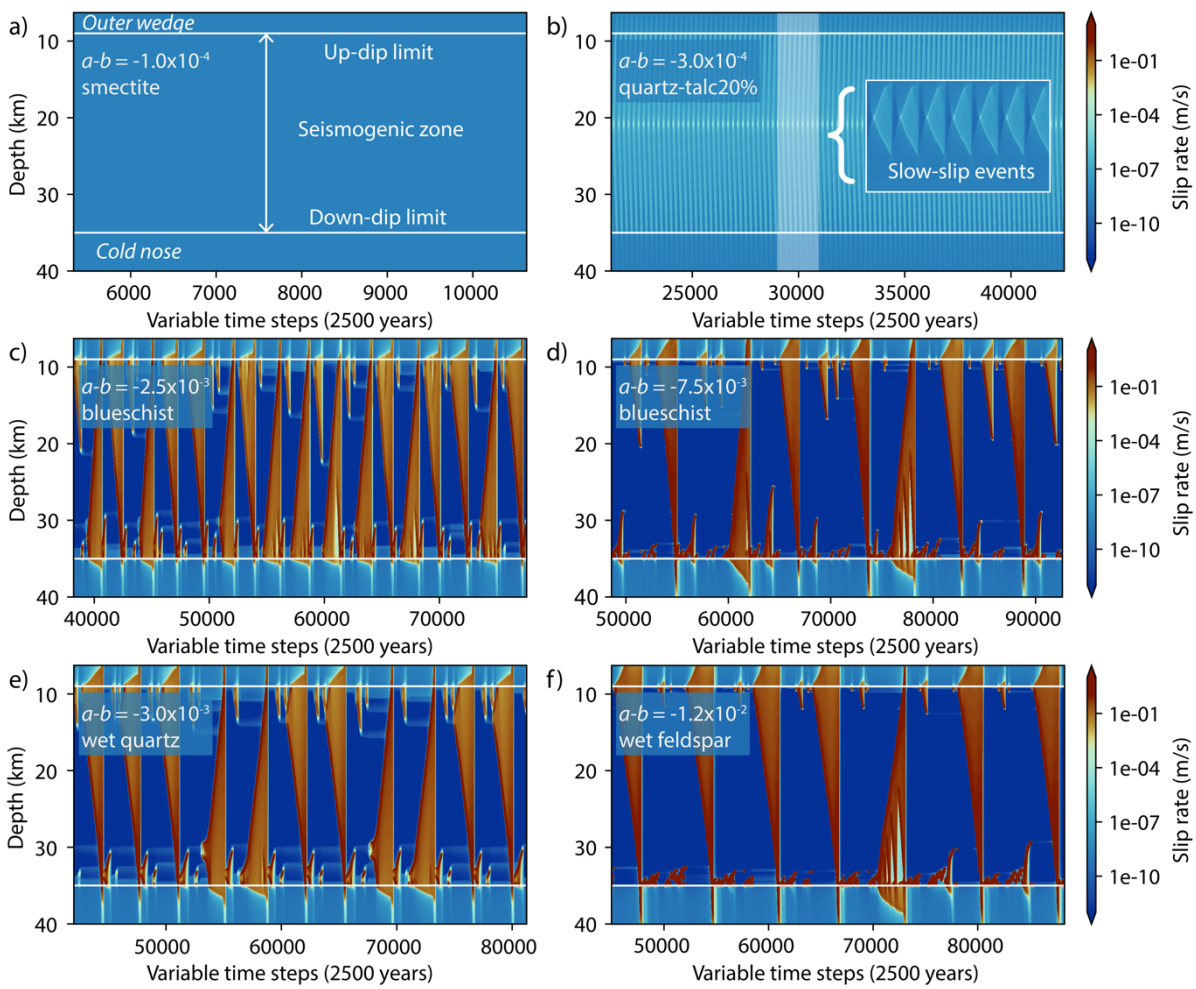

Figure 4.2. Different simulations of the seismic cycle at Southern Chile by changing $a-b$. Each plot is depth at the fault against variable time steps of simulation. The grid shows the values of slip-rates at the fault. Properties used on each model are listed in Supplementary Material Table 6.7. All cases show the slip-rate with

variable time steps in between the years 2500 and 5000 of the simulation assuming $\lambda = 0.825$. $a - b$ values are obtained from minerals at Fig. 4.1.

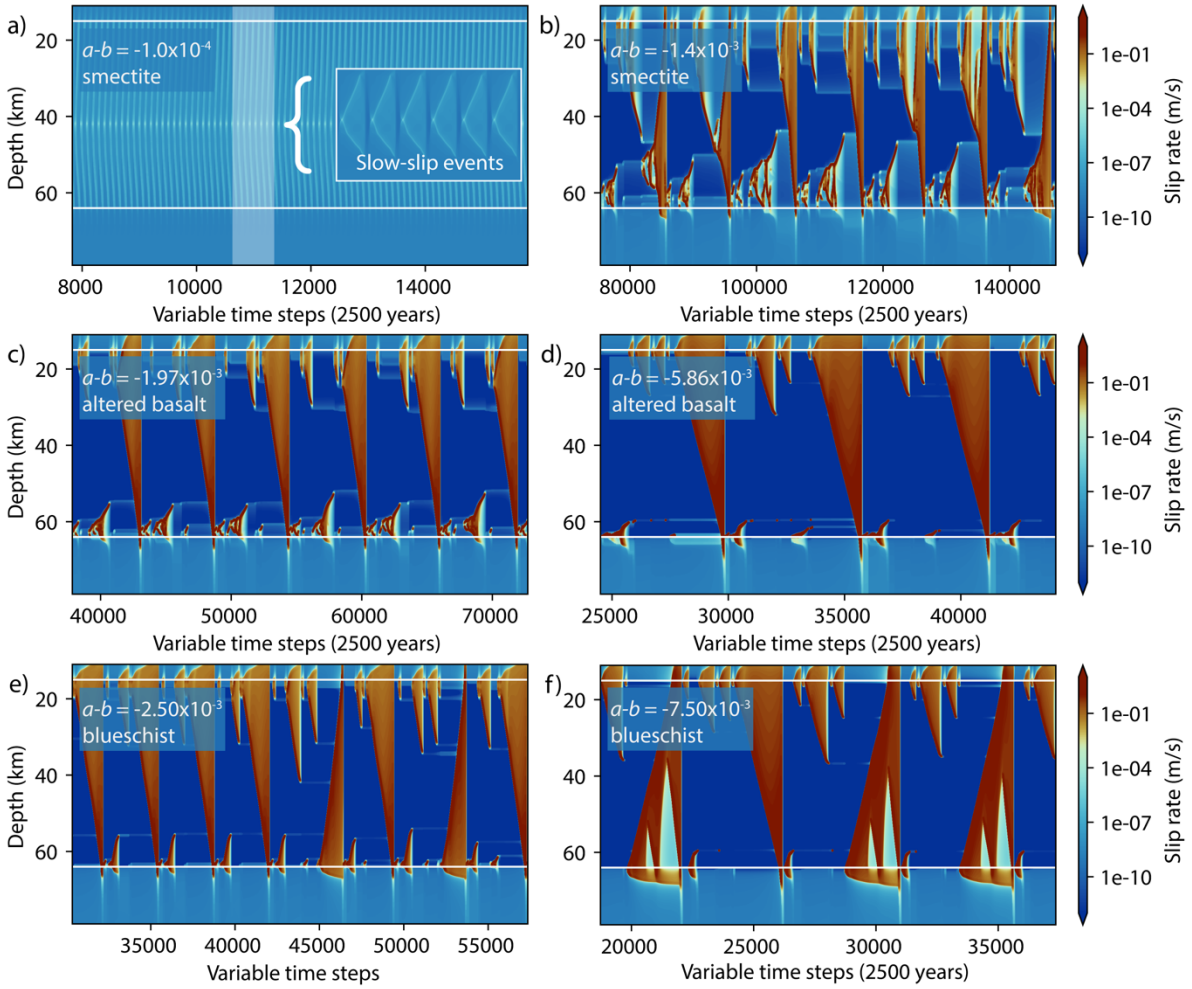

Figure 4.3. Different simulations of the seismic cycle at Northern Chile by changing $a - b$. Each plot is depth at the fault against variable time steps of simulation. The grid shows the values of slip-rates at the fault. Properties used on each model are listed in Supplementary Material Table 6.8. All cases show the slip-rate with variable time steps in between the years 2500 and 5000 of the simulation assuming $\lambda = 0.825$. $a - b$ values are obtained from minerals at Fig. 4.1.

For Northern Chile, we used the same assumptions as in Chapter 3, but varying the $a - b$ values based on the expected gouge composition inferred from geophysical and geological observations (Chapter 3). High rate weakening values of $a - b$ are expected for smectites, altered basalt, and blueschist samples at low $\overline{\sigma_n}$ and temperature (Fig. 4.1). A major difference with Southern Chile is that smectite samples with the smaller rate weakening behavior can produce SSE (Fig. 4.3a and Fig. 4.5a), where same

values show aseismic creeping at convergence rate in the Southern case (Fig. 4.2a). By looking the assumed $\overline{\sigma_n}$ for both models (Supplementary Figure 6.9), is clear that under same $a - b$ values, larger $\overline{\sigma_n}$ distribution develop SSE activity, highlighting the role of the upper plate composition during the seismic cycle. Previous works have shown that SSE are prompt to occur at regions where $\overline{\sigma_n}$ is decreased by fluid flow at high porosity faults (Kodaira et al., 2004; Liu & Rice, 2007; Wallace, 2020), but these models show that under rate-weakening to rate-strengthening transitions, SSE may still develop. In these models, this feature is especially important at $a - b \leq -5x10^{-3}$ (Fig. 4.5).

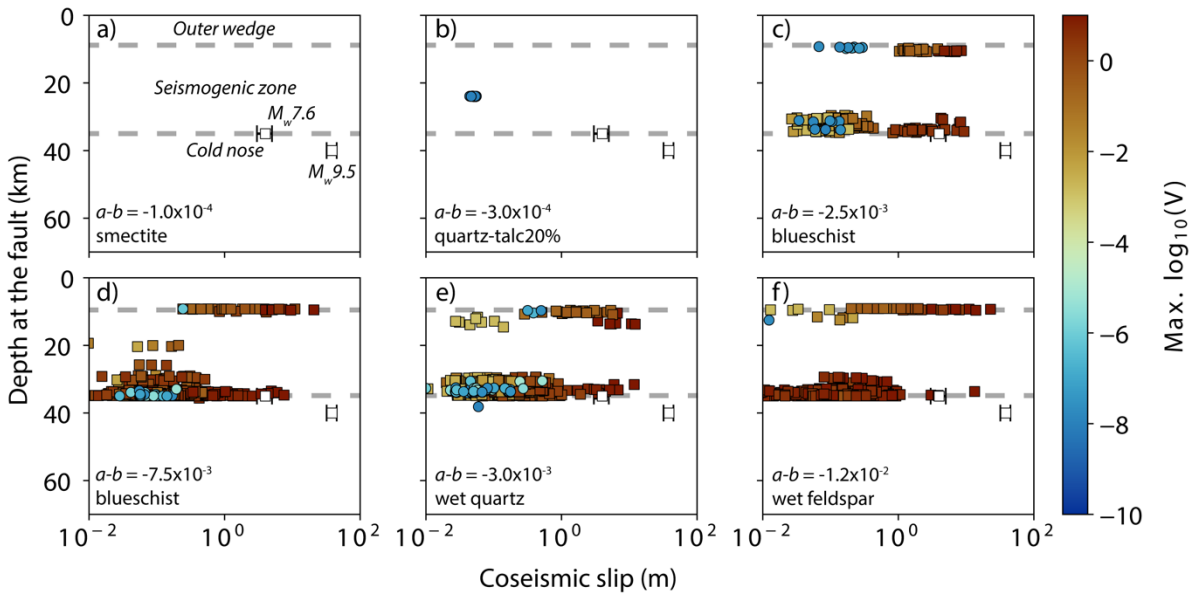

Figure 4.4. Spectrum of slip mechanisms with changes in $a - b$ for Southern Chile. The models shown are the same as is Fig. 4.2. Frictional parameters used on each simulation are detailed in Supplementary Table 6.7. The white box of Mw 7.6 corresponds to the Melinka earthquake, while the one with Mw 9.5 is the Valdivia earthquake. Gray dashed lines mark the limits of the seismogenic zone. Circles are events categorized as SSE with peak velocities of less than 10^{-5} m/s. Squares are earthquakes with peak velocities surpassing 10^{-3} m/s.

When greater rate weakening values of smectite are considered, the Northern Chile simulation develops complex patterns of ruptures in which full and partial events are precluded by cascading sequences (Fig. 4.3b). Notably, when the rate weakening behavior is slightly greater up to altered basalt range (Fig. 4.3c), then up-dip and down-dip partial ruptures decrease in size and its nucleation start to be restricted to the limits

of the seismogenic zone (Fig. 4.5c, d). Since the $\overline{\sigma_n}$ distribution is constant between all cases, a strong effect of μ is suggested. Smectite gouges have μ = 0.25, while altered basalt gouges have μ = 0.6 (and even greater in blueschist compositions μ = 0.7, Supplementary Table 6.6 and 6.8). There is a progressive decreases in cascading foreshock and aftershock ruptures before partial and full earthquakes from smectite to blueschist gouges (Fig. 4.3b-f and Fig. 4.5a-f). Within this framework, while $a - b$ allows the sequence of full and partial ruptures, lower values of μ control the extension of those events, developing cascading sequences of seismicity before large or giant earthquakes in the simulation.

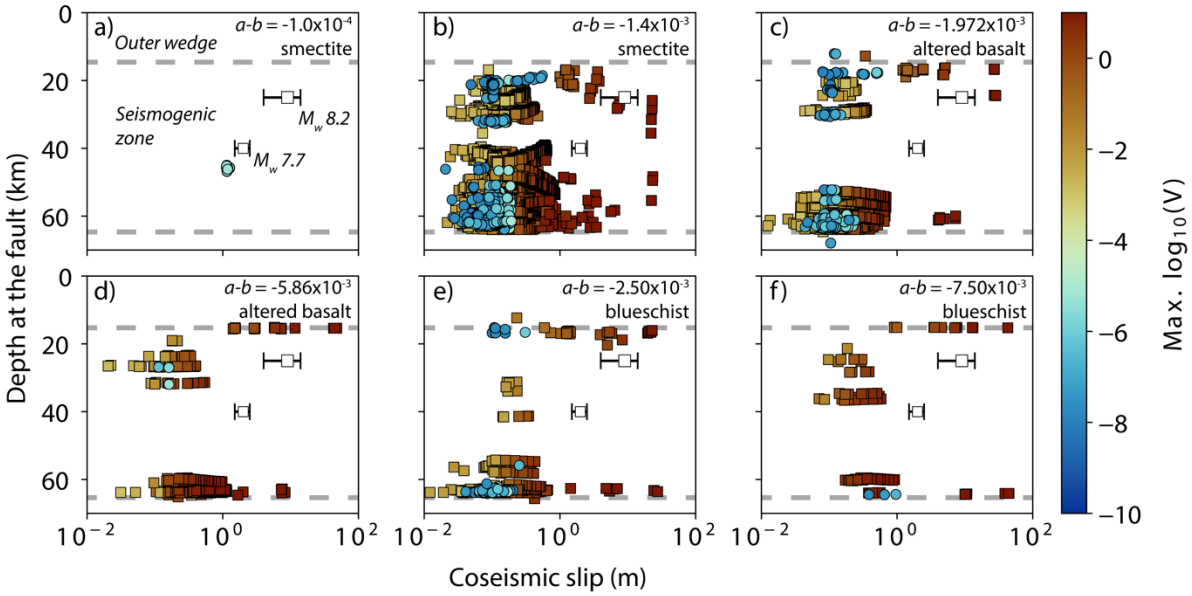

Figure 4.5. Spectrum of slip mechanisms with changes in $a - b$ for Northern Chile. The models shown are the same as is Fig. 4.3. Frictional parameters used on each simulation are detailed in Supplementary Table 6.8. The white box of Mw 8.2 corresponds to the Iquique earthquake, while the one with Mw 7.7 is the Tocopilla earthquake. Gray dashed lines mark the limits of the seismogenic zone. Circles are events categorized as SSE with peak velocities of less than 10^{-5} m/s. Squares are earthquakes with peak velocities surpassing 10^{-3} m/s.

Finally, both altered basalt and blueschist gouges may develop giant and large ruptures, where the last ones are mostly nucleated at the up-dip limit of the seismogenic zone, like the 2014 Mw8.2 Iquique earthquake, supporting the conclusions of Chapter 3. Simplified models as the one shown in Fig. 4.3, cannot reproduce the precursory face simulated in Chapter 3, highlighting the role of upper-plate faulting during observed

up-dip partial earthquakes in Northern Chile. In a similar case to Southern Chile, the Northern seismic cycle is controlled by altered basalt from the subducted plate and blueschist metamorphism, although the observed SSE can be the expression of the transition from rate strengthening to rate weakening behavior up-dip. In both simulations of the Chilean subduction zone, the composition of the fault gouge will play a key role on the spectrum of slip-mechanisms observed during the seismic cycle.

By using simplified models, here it is shown that the nature of the earthquakes and slow slip events observed along the Chilean margin, arise mainly from the interaction and deformation of minerals at the plate interface, which is likely controlled by the tectonic environment that will modulate the amount and type of sediments being subducted, and the thermal and stress regime that those materials will experience. Ultimately, this conditions will govern the frictional response due to the changes of $a - b$ with temperature and stress.

4.2. The effect of effective normal stress

During Chapters 2 and 3, it was shown that the hydraulic state governs recurrence times and rupture styles during the seismic cycle of the Chilean subduction zone. Fluids coming from the release of water due metamorphic reactions during prograde metamorphism below the cold nose, are then trapped at the limit between the continental Moho and the plate interface. The presence of basal accretion and underplating structures allows the accumulation of fluids at that depth, generating a segmentation in the pore-pressure ratio close to the transition from rate weakening to rate strengthening behavior. Moreover, upper-plate faulting located in the outer and inner wedge, can develop fluid flow in between the plate interface and the forearc wedge, draining the megathrust and thus allowing precursory seismicity and aseismic slip before large earthquakes.

To explore even further the role of $\overline{\sigma_n}$ at Southern and Northern Chile, 4 new simulations are run (Fig. 4.6 and Fig. 4.7). In these examples, a $\overline{\sigma_n}$ perturbation is induced in the initial setup of the model. The same parameters as in Fig. 4.2 and Fig. 4.3 are assumed,

using wet feldspar and wet quartz in Southern Chile, and altered basalt and blueschist in Northern Chile. The selection of these $a-b$ values is based on the most likely composition expected at the plate interface based on the geological and geophysical observations mentioned in Chapter 2 and Chapter 3 respectively. Perturbations in $\overline{\sigma_n}$ are induced by assuming a linear increase in the λ distribution with depth, from 0.825 to 0.985, to then return to the mean value of 0.825 (Supplementary Figure 6.10 and Fig. 4.8), in a similar way to the one proposed by Saffer & Tobin (2011) and Saffer & Wallace (2015). The main idea is to test how smooth changes in λ, which represent the concentration of fluids at the continental Moho depth and below the outer wedge in Southern and Northern Chile respectively, impact the seismic cycle at the megathrust.

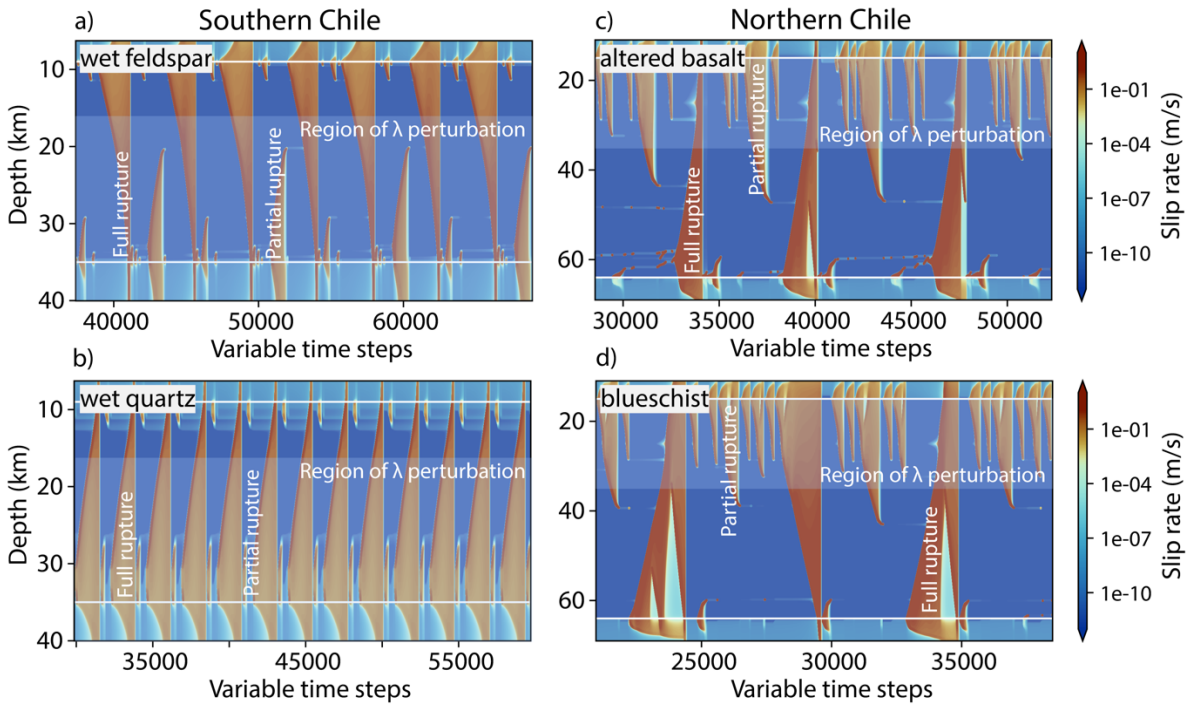

Figure 4.6. Seismic cycle simulations by changing λ distribution at Southern and Northern Chile. Figures a) and b) are two models run with the same properties as in Fig. 4.2 for wet quartz and wet feldspar $a-b$ values. Here, a λ perturbation has been induced to capture the changes in $\overline{\sigma_n}$ at the down-dip limit of the seismogenic zone. Figures c) and d) show two models run with the same properties as in Fig. 4.3 for altered basalt and blueschist $a-b$ values (Fig. 4.3d and Fig. 4.3f respectively). Here, a λ perturbation has been induced to capture the changes in $\overline{\sigma_n}$ at the up-dip limit of the seismogenic zone.

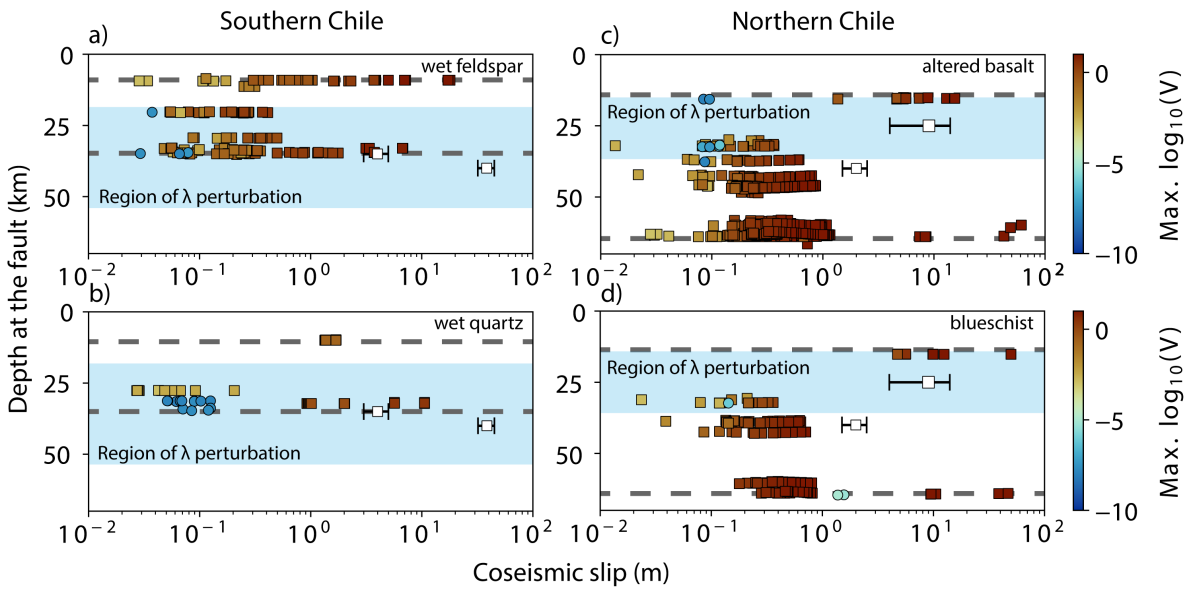

Figure 4.7. Spectrum of slip mechanisms with induced perturbation of $\overline{\sigma_n}$ at Northern and Southern Chile. Each subplot shows the maximum coseismic slip of each event against the nucleation depth. The scatter plots are colored based on the maximum velocity at each event. Results from a) to d) correspond to the simulations in Fig. 4.6 respectively. Squares represent the seismicity above 10^{-3} m/s, while dots are SSE with peak velocities of less than 10^{-5} m/s.

By inducing a decrease in $\overline{\sigma_n}$ changing the λ distribution at the base of the seismogenic zone in Southern Chile, the variability of seismicity is diminished (Fig. 4.7a, b). The seismic cycle becomes homogeneous in both scenarios of wet feldspar and wet quartz, but wet feldspar configuration show that great earthquakes are nucleated only at the up-dip limit of the seismogenic zone. In Chapter 2, it was proposed that Valdivia-like events are nucleated at the bottom of the seismogenic zone, close to the continental Moho intersection, being strongly controlled by the structure of the forearc wedge. If that is the case, then wet quartz gouges are needed along with the decrease of $\overline{\sigma_n}$ at the down-dip region. This means that when the plate interface is controlled by strong rate-weakening values as in wet feldspar configuration, then there is a preference for the megathrust to accumulate stress at the up-dip region, even if the distribution of $\overline{\sigma_n}$ has been smoothed by a perturbation of λ. A trade-off scenario arises between $a - b$ and $\overline{\sigma_n}$ distributions with depth. Not only small variation of $\overline{\sigma_n}$ within the seismogenic zone is needed, but also rate-weakening values of $a - b < -10^{-2}$ (Fig. 4.7a, b). This fact leads to think that the hydraulic state at the megathrust in Southern Chile cannot

be averaged at least within the seismogenic zone, and some segmentation is needed to decrease the curve of $\overline{\sigma_n}$, which is generated by the increase of vertical stress with depth, at the seismogenic megathrust. Chapter 2 shows that in Southern Chile, this feature is achieved by the release of fluids after prograde metamorphic reactions, which are then trapped at the base of the seismogenic zone. If wet quartz configurations are in fact, controlling the frictional behavior of the fault, then the smooth variation of $\overline{\sigma_n}$ in this specific case will favor rupture nucleation of giant and large earthquakes down-dip and close the Moho intersection, where a change from rate weakening to rate strengthening is expected (Fig. 4.6b and Fig. 4.8).

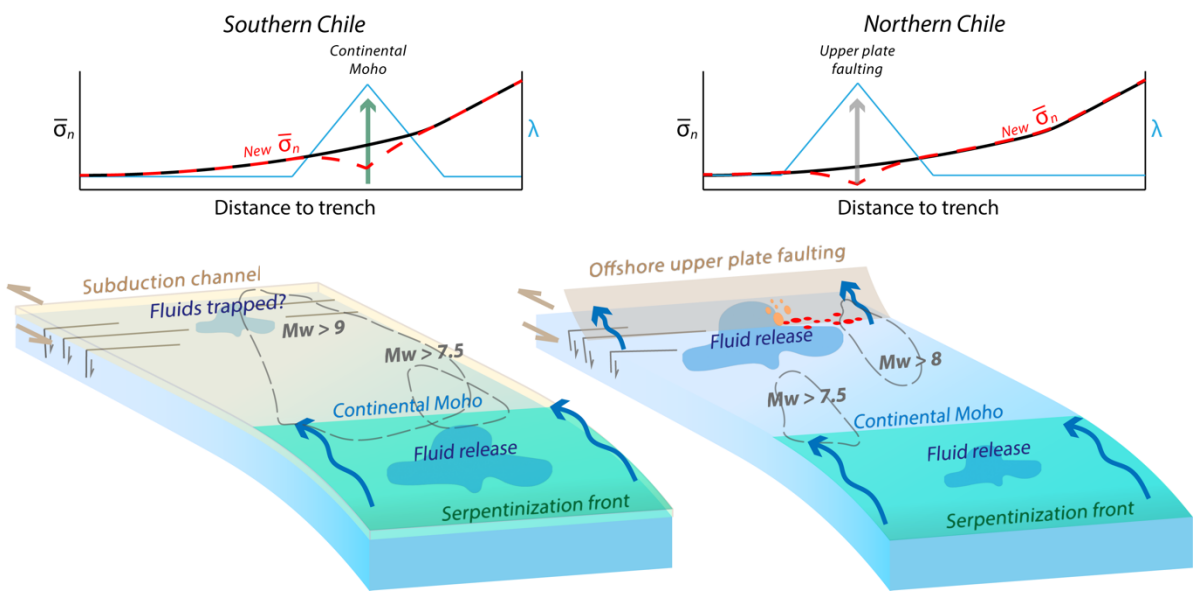

Figure 4.8. Final conceptual model of the subduction systems at Southern and Northern Chile. Dashed lines represent coseismic slip distributions of major earthquakes at the plate interface. Blue arrows mark the fluid path released from prograde metamorphism. Orange dots are the seismicity observed at upper plate faults, while red dots represent the seismicity observed in the vicinity of the fault at the plate interface. Dashed red line is the new distribution of $\overline{\sigma_n}$ after the induced perturbation in λ.

Regarding SSE, the decrease in the $\overline{\sigma_n}$ at the down-dip limit, decrease the number of events with peak velocities of less than 10^{-5} m/s, which suggest that in Southern Chile, SSE are a slip-mechanism that is not favored by high pore-pressure ratios, but by the composition of the minerals at the plate interface. One possibility is that the transitions from a lower λ value to a higher one, which are needed to decrease $\overline{\sigma_n}$, happen abruptly

and not in a smooth way as it was assumed in these cases. This feature will impose a strong stress concentration at those boundaries, thus allowing the nucleation of SSE. The last property that changes with $\overline{\sigma_n}$ are recurrence times. Smaller values of $\overline{\sigma_n}$ generate lower recurrence times (i.e. more frequent events). In Chapter 2 it was shown that paleoseismic data can be used to constrained λ distributions. The simplified models shown in this chapter are not intended to reproduce that dataset, but to show how the models are sensitive to some changes in some relevant physical properties.

For the Northern Chile scenario (Fig, 4.6c, d and Fig. 4.7c, d), a λ perturbation in the up-dip region will generate more up-dip partial ruptures compared with the case without it (Fig. 4.3d and Fig.4.6c), and it will also enlarge the rupture propagation down-dip on each of those earthquakes (Fig. 4.6c, d). Foreshock and aftershock sequences are decreased, meaning that lower $\overline{\sigma_n}$ values promote aseismic slip. Precursory activity before megathrust earthquakes that involve foreshock seismicity, require λ values below 0.85, or just aseismic slip will be observed otherwise (Chapter 3). This means that if a highly fractured slab is subducted, prompt to accumulate fluids that may be released with depth, then there should be a mechanism of fluid flow between the plate interface and the upper plate, to decrease λ values in the megathrust and allow foreshock and aftershock seismicity before and after a large or giant rupture. Moreover, λ perturbations generate rupture nucleation to be located towards the end of that perturbation, where λ returns to the assumed mean value (Fig. 4.7c, d). This will define a region where future ruptures can be propagated but not nucleated.

Notably, in both Northern Chile cases, there is few occurrence of large earthquakes (7.5 ≤ Mw ≤ 8.5) nucleated down-dip, which is a feature that can be observed in the small maximum coseismic slip of those events (< 2 m in both scenarios, Fig. 4.7c, d). Despite the differences in the geometry of the subducted plate, the Northern Chile subduction zone has hosted large earthquakes before (Mw > 7.5), where the 2007 Mw 7.7 Tocopilla earthquake is the most recent case. By looking at the results without a perturbation in λ (Fig. 4.3c-f and Fig. 4.5c-f), if the differences in $\overline{\sigma_n}$ between the up-dip and down-dip regions are increased, then the propagation of partial down-dip ruptures is limited. This scenario may justify the low λ values (< 0.85) needed in the whole

seismogenic zone to promote both, seismicity during the precursory phase of megathrust earthquakes, and the occurrence of large down-dip ruptures. One final striking feature is that giant ruptures, which are those that breaks from the down-dip limit of the seismogenic zone up to the trench, are more frequent in time at Southern Chile compared to the Northern case. If we look at the simulations with the most negative value of $a - b$ (Fig. 4.2f and Fig. 4.3f), then we will see that rock composition is not the parameter controlling this feature. The two major differences between the two cases are (1) the distribution of $\overline{\sigma_n}$ given by the vertical stress from the upper plate and fault geometry $\sigma_n = \rho g h cos(\alpha)$, where ρ is the average density of the upper plate and α is the dip angle of the subducted plate, and (2) the width of the seismogenic zone (W). Veedu & Barbot (2016) showed that recurrence times are directly proportional to $a - b$, $\overline{\sigma_n}$, and W. If we assume that crustal thickness is larger in the north and the continental Moho intersection with the megathrust controls the end of interplate seismicity, then by decreasing W we should expect giant ruptures to happen frequently, which is the case for Southern Chile. Moreover, by looking at the $\overline{\sigma_n}$ distribution driven by vertical stress at both, Southern and Northern Chile (Supplementary Material Fig. 6.9), is clear that there are higher values within the seismogenic zone in the Northern case, which may explain, along with a wider W, the lower frequency of giant ruptures.

By analyzing the seismic cycle of Southern and Northern Chile with these simple assumptions, the role of fault gouge composition at certain conditions of temperature and stress was studied. The first order features of the seismic cycle, meaning the slip mechanisms and its mechanical relationships, are mainly governed by the minerals at the plate interface and the potential generation of a subduction channel. Then, the hydraulic state at the megathrust, which is the consequence of a complex relationship between fluid release from the minerals due to prograde metamorphism and fluid flow linking the upper plate faults with the plate interface, will govern the rupture propagation and the seismicity prior or after a megathrust earthquake (Fig. 4.8).

5 Conclusions

After a large recompilation of geophysical and geological data used to constrain the initial setup of quasi-dynamic numerical models along key latitudes at Northern and Southern Chile, this work suggests that:

1. The mineral composition of the rocks and sediments that are being deformed at the plate interface will control the frictional behavior of the megathrust at seismic cycle timescales. This means that the tectonic setting of the subduction zone is a major factor modulating the composition of sediments that reach the trench to then being subducted, but also the temperature and stress conditions within the subduction system.
2. Fluids at the plate interface, which decrease the effective normal stress of the megathrust, will impact on the recurrence times of large and giant earthquakes, and will allow rupture propagation on areas where the background effective normal stress will prompt aftershock and foreshock sequences otherwise. The presence of active offshore upper plate faults may induce fluid flow at regimes in which a highly fractured slab transport fluids to the up-dip region of the plate interface. Nevertheless, the valving mechanism that may exist in this framework is still poorly understood and requires further studies.
3. Temperature and pressure acting on the megathrust is a major factor governing the rate strengthening or rate weakening behavior of the minerals that are interacting at the plate interface, and they will also impact on the stability of those minerals favoring the occurrence of prograde metamorphism that in this context, will generate mineral dehydration and fluid release.
4. The structure of the forearc wedge play a role on the seismogenic limit of the megathrust, defining the transition from rate weakening to rate strengthening behavior, marked by the frictional properties of serpentinites and by the depth of the 350°C isotherm that control the brittle to ductile deformation of some minerals at the subduction channel.

6 Appendix

6.1 Supplementary Material Chapter 2

Recurrence time and size of Chilean earthquakes influenced by geological structure.

Joaquín Julve [1,2], Sylvain Barbot[3], Marcos Moreno[4], Andrés Tassara[1,2], Rodolfo Araya[5], Nicole Catalán[1], Jorge G. F. Crempien[4] & Valeria Becerra-Carreño[4].

[1]Departamento Ciencias de la Tierra, Facultad de Ciencias Químicas, University of Concepción, Concepción, Chile.

[2]Millennium Nucleus: The Seismic Cycle Along Subduction Zones CYCLO, Valdivia, Chile.

[3]Department of Earth Sciences, University of Southern California, Los Angeles, CA, USA.

[4]Department of Structural and Geotechnical Engineering, Pontifical Catholic University of Chile, Santiago, Chile.

[5]Departamento de Ingeniería Matemática, University of Concepción, Concepción, Chile.

Submitted to *Nature Geoscience* on January 21st, 2023, and accepted on October 19th, 2023 (Published on December 15th, 2023).

Volume	A ($MPa^{-n}s^{-1}$(ppm H/Si)$^{-r}$)	r	C_{OH} (ppm H/Si)-	n	Ω (cm^3/mol)	Q (Kj/mol)
Oceanic Mantle	$10^{0.56}$	1.2	1000	3	1.30E-05	5.10E+05
Continental Mantle (dry conditions)	$10^{0.56}$	1.2	1000	3	1.10E-05	4.75E+05
Continental Mantle (wet conditions below the arc)	$10^{0.56}$	1.2	1200	3	1.10E-05	5.10E+05

Supplementary Material Table 6.1. **Power-creep law properties**. Initial values were obtained from reference (Karato and Jung, 2010; Masuti et al. 2016).

USZ		LSZ		CZ			
				MB		AB	
λ	σ (Mpa)	λ	σ (Mpa)	λ	σ (Mpa)	λ	σ (Mpa)
0.6	150	0.6	300	0.6	520	0.6	880
0.65	131	0.65	263	0.65	455	0.65	770
0.7	113	0.7	225	0.7	390	0.7	660
0.75	94	0.75	188	0.75	325	0.75	550
0.8	75	0.8	150	0.8	260	0.8	440
0.85	56	0.85	113	0.85	195	0.85	330
0.9	38	0.9	75	0.9	130	0.9	220
0.95	19	0.95	38	0.95	65	0.95	110

Supplementary Material Table 6.2. **Pore pressure ratio and effective normal stress variation**. USZ = Upper seismogenic zone, LSZ = Lower Seismogenic Zone, MB = Metamorphic Belt, AB = Ancud Basin, CZ = Creeping Zone.

Layer	Thermal conductivity (W/mK)	Radiogenic heat production ($\mu W/m^3$)	Density(kg/m^3)	Specific heat (J/kgK)
Upper continental Crust	2.9	1.3	2700	1000
Lower Continental Crust	2.9	0.4	3300	1000
Oceanic Crust	3.1	0.02	3300	1000
Oceanic and Continental Mantle	3.1	0.02	3300	1000

Supplementary Material Table 6.3. **Thermal properties of the temperature model.**

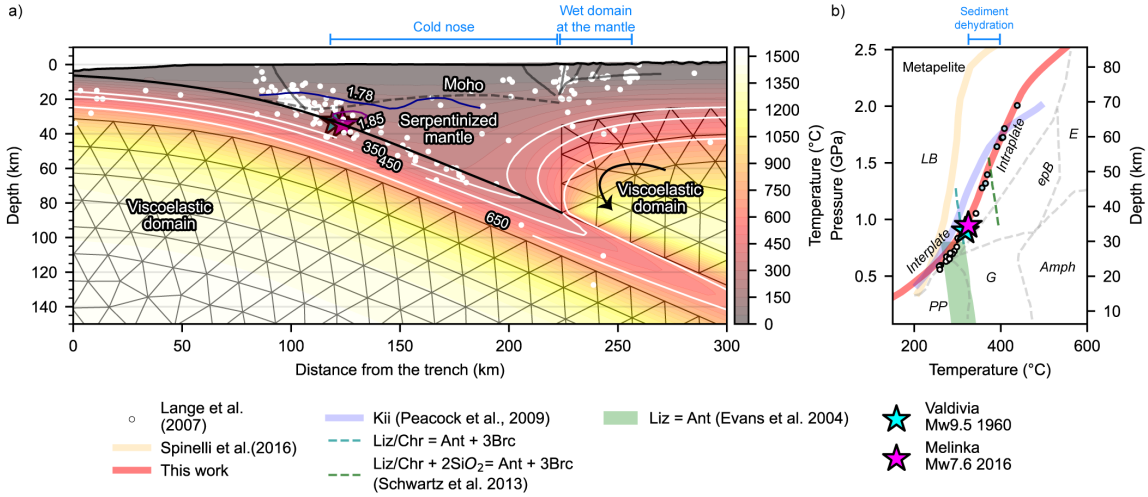

Supplementary Material Figure 6.1. **Temperature distribution, mesh, and pressure-temperature path**. a) black arrow denotes the convective asthenosphere flux. Purple curves are contours of the Vp/Vs value (Dzierma et al., 2012). Triangles are the mesh used for the continental and oceanic mantle. b) Gray dashed lines are the limits of metamorphic facies for a metapelite rock (Condit et al. 2020). LB = Lawsonite Blueschist, epB = Epidote Blueschist, Amph = Amphibolite, G = Greenschist, PP = Prehnite-Pumpellyite, E = Eclogite. Intraplate and Interplate refer to the location of the interseismic seismicity.

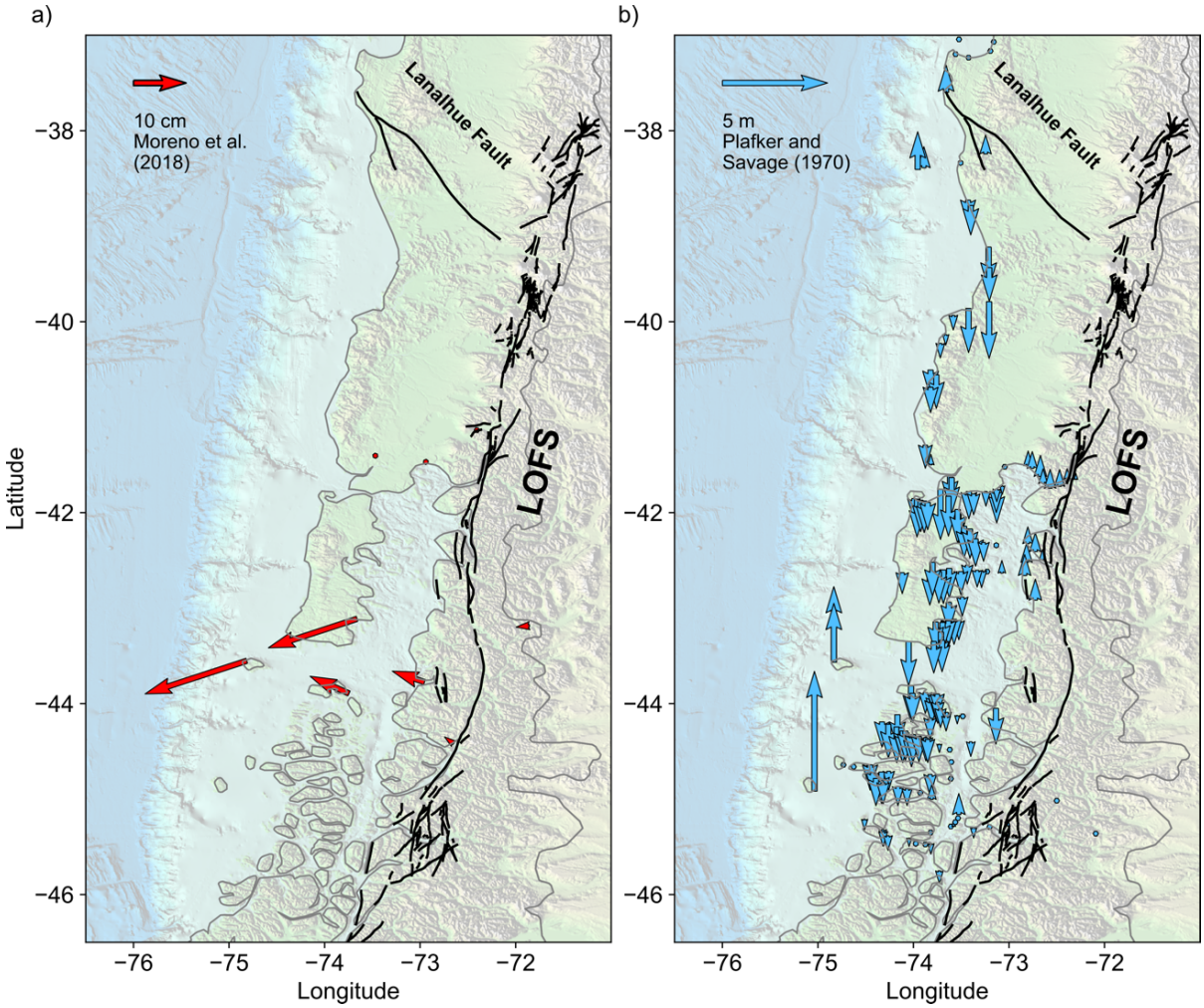

Supplementary Material Figure 6.2. **GNSS and intertidal biotic indicator data**. a) Velocity vectors from reference (Moreno et al. 2018) for the coseismic slip of the Melinka Mw7.6 2016 earthquake. b) Uplift data from reference (Plafker & Savage, 1970) measured after 8 years of the Valdivia Mw9.5 1960 earthquake.

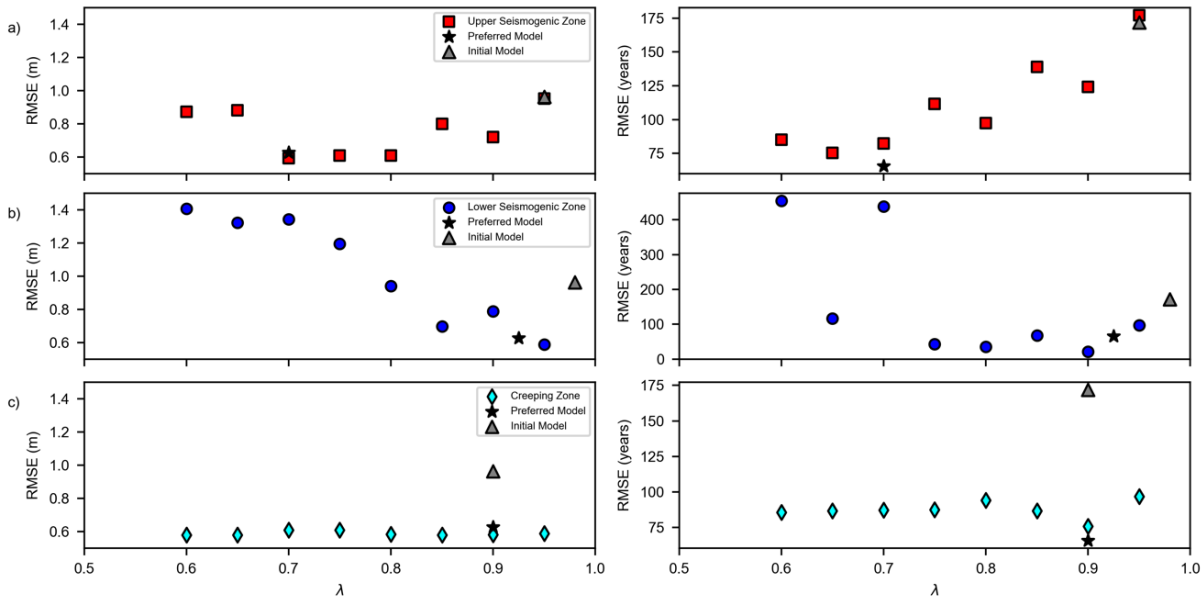

Supplementary Material Figure 3. Root mean squared error values for systematic variation on λ. In the left column are plotted RMSE values with respect to the surface deformation obtained from GNSS data of Melinka and Valdivia earthquakes. In the right column are plotted RMSE values with respect to the median value of great and large earthquakes obtained from the paleoseismic record. Creeping zone in c) refers to the Metamorphic Belt and Serpentinized Mantle Wedge segments.

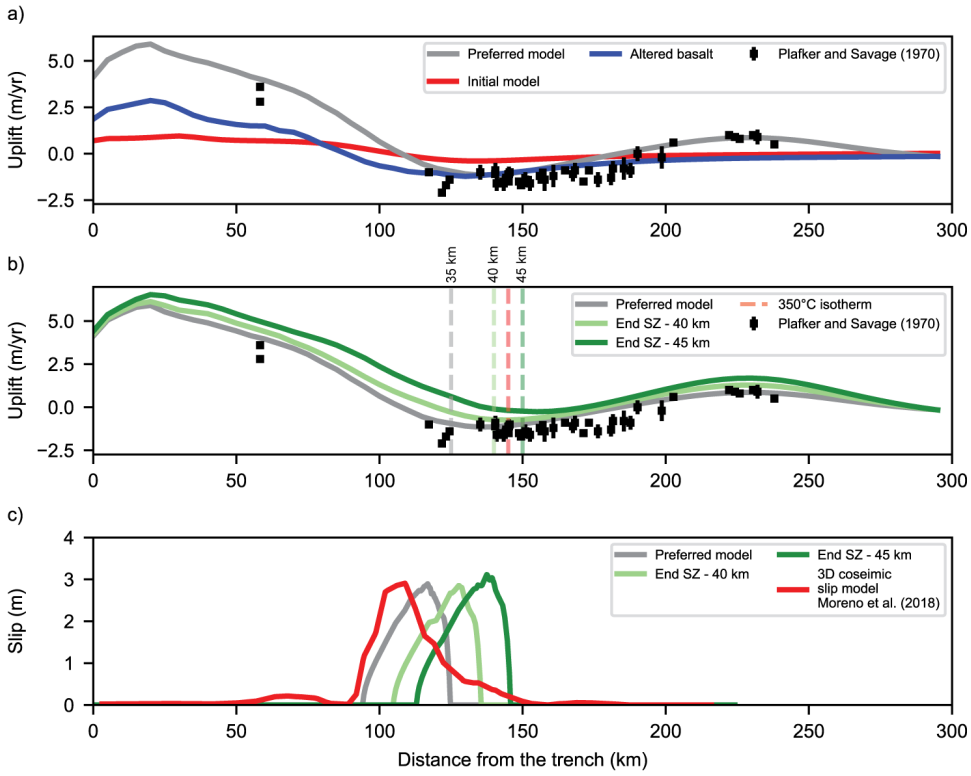

Supplementary Material Figure 6.4. **Effects of petrology and depth of the end of the seismogenic zone**. Isotherm in b) is obtained from our computed thermal distribution. Gray and green dashed curves mark the depth in which ends the seismogenic zone for each model. The red curve is the interpolation at 43°S of the 3D coseismic slip model from reference (Moreno et al. 2018) ends the seismogenic zone for each model. The red curve is the interpolation at 43°S of the 3D coseismic slip model from reference (Moreno et al. 2018). Frictional parameters for each non preferred model are described in Supplementary Material Table 1.

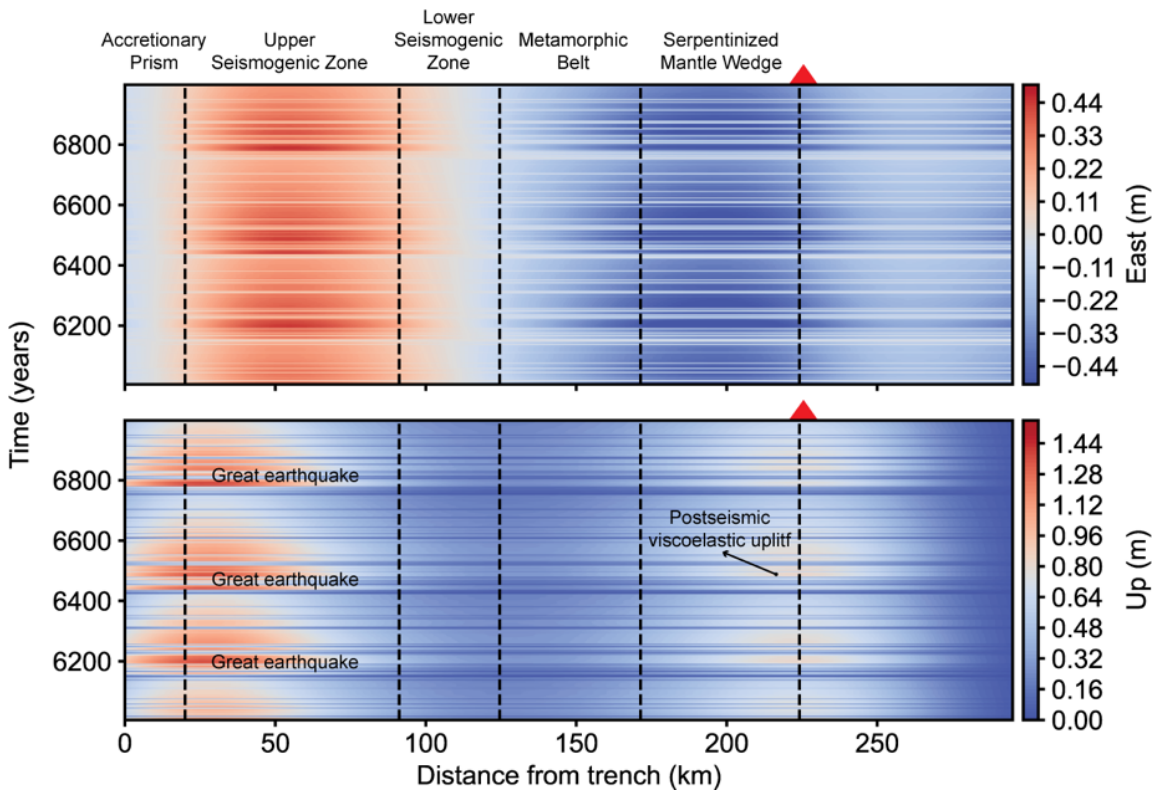

Supplementary Material Figure 6.5. **Time series of the east and vertical components of the synthetic GPS from our model**. We select the same time interval from Figure 3. Red triangles mark the position of the volcanic arc.

6.2 Supplementary Material Chapter 3

Impact of Upper-Plate Faulting on Foreshocks: Insights from the 2014 Iquique Earthquake

J. Julve[1], M. Moreno[2], S. Barbot[3], A. Tassara[1].

[1]Universidad de Concepción, Earth Science Department.

[2]Pontifical Catholic University, Structure and Geotechnical Engineer Department.

[3]University of Southern California, Earth Science Department.

Submitted to Geophysical Research Letters on June 26th, 2024. It is currently being reviewed.

Contents of this file

Text S1 to S5

Figures S1 to S3

Tables S1 to S2

Introduction

The Supplementary Material contains a detailed description of the model setup, parameters, and simulation bases. S1 covers modeling upper-plate fault and megathrust earthquake cycles, S2 includes geological and geophysical information, S3 addresses stress to strain interactions, S4 presents the thermal model, and S5 has the detail of the methodology to recover coseismic displacements from continuous GPS stations. The resulting temperature distribution is used as input for the quasi-dynamic simulations. Tables S1 and S2 summarize all parameters used in both models. The only difference between M1 and M2 is the inclusion of the offshore W-dipping upper-plate fault in the computations. After running the models, we filter out the first 3000 years of simulation to eliminate the influence of initial conditions. All processing to

compute the Mw of each rupture is done with the remaining time. Rheological parameters of dry and wet olivine are obtained from Hirth & Kohlstedt (2003) and Karato & Jung (2010).

6.2.1. Modeling upper-plate fault and megathrust earthquake cycles (S1)

We investigate the effect of an offshore upper-plate-crustal fault on the seismic cycle of megathrust earthquakes in Northern Chile. We utilize quasi-dynamic, two-dimensional numerical models to determine whether such a structure affects the rupture process and precursory activity during simulated subduction zone earthquakes. We estimate the evolution of slip-rate V over time using a slip-rate- and state-dependent friction law in isothermal, isobaric conditions (Barbot, 2019a)

$$\tau = \mu_0 \overline{\sigma_n} \left(\frac{V}{V_0}\right)^{\frac{a}{\mu_0}} \left(\frac{\theta V_0}{L}\right)^{\frac{b}{\mu_0}} \qquad \text{eq. 6.1 (1)}$$

where the shear stress τ depends on a reference coefficient of friction μ_0 at a reference velocity V_0, and on the background value of effective normal stress $\underline{\sigma_n}$ along the fault. The parameters a and b control the direct effect of velocity and the evolutionary phase, respectively, and are influenced by the composition of the fault gouge. The state variable θ represents the age of contact (Dieterich, 1979; Ruina, 1983) and follows an evolution law that allows healing at stationary contact. The characteristic slip distance L is associated with the representative contact age L/V_0. Fault segments associated with $a - b > 0$ are velocity strengthening, which inhibits rupture nucleation and propagation. Velocity-weakening frictional behavior is obtained for $a - b < 0$, which allows for unstable sliding and stick-slip instabilities.

The two faults are situated above a viscoelastic domain representing the continental and oceanic mantle (Fig. 3.1c). To ensure numerical convergence, we discretize the faults into points spaced 200 m apart along the megathrust and 180 m apart along the upper-plate fault. The viscoelastic domain is discretized using quasi-equilateral triangles with a size of 12.5 km (Fig. 3.1c and Supplementary Material Fig. S1). We employ the Slab2 model (Hayes et al., 2018) to constrain the megathrust geometry,

while delineating the offshore fault based on foreshock seismicity one month prior to the Mw 8.1 Iquique earthquake (Schurr et al., 2020), seismic line interpretations of the forearc structure (Storch et al., 2021), and the preferred orientation of nodal planes from the focal mechanism solution of the Mw 6.7 earthquake (Herman et al., 2016; Schurr et al., 2020) (Fig. 3.1c, d). Changes in traction and strain-rate over time are computed using the UniCyclE code (Barbot, 2018; Barbot, 2020). For the total anelastic strain rate $\dot{\varepsilon_T}$, we utilize a Burgers assembly such that $\dot{\varepsilon_T} = \dot{\varepsilon_M} + \dot{\varepsilon_K}$ where *M* and *K* denote the Maxwell and Kelvin components, respectively (Masuti et al., 2016; Masuti & Barbot, 2021) (Supplementary Material, S1). We assume a wet olivine rheology adjacent to the cold mantle wedge and a dry olivine rheology elsewhere (Hirth & Kohlstedt, 2003; Karato & Jung, 2010, Supplementary Material Table 6.1). The temperature distribution (Fig. 3.1c, Supplementary Material Fig. S2) is determined using a finite-element numerical method (Araya et al., 2023) that solves the steady-state heat advection-diffusion equation at 20°S (Supplementary Material S2). We consider a stratified continental plate where thermal conductivity and thermal diffusivity remain constant within each domain of the upper plate (Supplementary Material Table 6.1).

6.2.2. Geological and geophysical information (S2)

We infer the distribution of the frictional parameters in eq. 6.1(1) considering the expected lithology at the plate interface based on the interpretation of geological and geophysical data in Northern Chile. Our cross-section at 20°S (Fig. 3.1b-d) incorporates the major geological features of the subduction zone by integrating seismic tomography and seismic reflection profiles (Comte et al., 2016; Geersen et al., 2018; Petersen et al., 2021; Sallarès & Ranero, 2005; Storch et al., 2021), background and foreshock seismicity prior to the Mw 8.1 2014 Iquique earthquake (Schurr et al., 2020), geodetic locking models (Li et al., 2015; Jolivet et al. 2020), and a newly derived thermal model (Fig. 3.1b, Supplementary Material S2).

The Northern Chile subduction zone is distinguished by a notably thin layer of sediments entering the subduction channel (Geersen et al., 2018), as a result of low

surface erosion rates due to hyper-arid climatic conditions since the Upper Miocene (Carretier et al., 2018; Kober et al., 2007). This has been also related to a narrow frontal accretionary prism of 5 to 30 km km-wide in the outer wedge (Geersen et al., 2018; Maksymowicz et al., 2018) (Fig. 3.1c). Analysis of background and foreshock seismicity (Schurr et al., 2020; Sippl et al., 2023; Soto et al., 2019), alongside locking degree models (Li et al., 2015; Jolivet et al., 2020) before the Iquique earthquake, indicates frictional instability along the megathrust from 17 to 60 km depth, while the outer wedge displays intense faulting and a high compressional to shear velocity ratio (Vp/Vs, up to 2.1), suggestive of a high-fluid zone (Petersen et al., 2021, Fig. 3.1d).

Under the described conditions, we deduce that basaltic rocks from the incoming Nazca plate control the frictional behavior of the megathrust above the continental Moho delineated by the 3D density model of Tassara and Echaurren (2012) (Fig. 3.1b). We use the corresponding mean a and b values from laboratory experiments conducted on unaltered basalt gouge from the South China Sea (Zhang et al., 2017) (Fig. 3.1b). Considering the megathrust pressure and temperature conditions at 21°S, results in velocity-strengthening behavior below the outer wedge (< 100°C), and a velocity-weakening domain between the inner wedge and the Coastal Cordillera (100°C – 300°C, Fig. 3.1b-c). The resultant distribution of frictional properties delineates a seismogenic zone within the depth range illuminated by background seismicity, where the locking degree reaches 0.5 or less (Fig. 3.1b). At greater depth, the Vp/Vs ratios beneath the continental Moho are indicative of serpentinization within the cold mantle wedge (Comte et al., 2016). As no interplate seismicity occurs at these depths, we assume that serpentinites control the frictional behavior of a mélange fault core. Mean values of a and b derived from laboratory experiments conducted on lizardite and antigorite gouge (Moore & Lockner, 2011; Okazaki & Katayama, 2015; Takahashi et al., 2011) under the pressure-temperature conditions at the megathrust result in an $a - b$ distribution compatible with velocity-strengthening behavior below the Central

Depression (Fig. 3.1b-c). The frictional parameters are summarized in Supplementary Material Table 2.

To determine $\bar{\sigma}_n$ we calculate the normal stress at the plate interface $\sigma_n = \rho g h cos(\alpha)$, using a spatially-varying average forearc density ρ (Tassara & Echaurren, 2012) spanning from the surface of the continental plate down to the megathrust h, with constant gravitational acceleration g and projected to the megathrust using the dip angle α resulting from the Slab2 geometry (Hayes et al., 2018). We compute the effective normal stress $\bar{\sigma}_n = (1 - \lambda)\sigma_n$, assuming an average background pore fluid pressure ratio $\lambda = 0.825$. This value closely aligns with the mean value explaining strain rates observed in the fabric of rocks in paleo subduction zones, ranging between brittle creep and solution precipitation creep as deformation mechanisms (Oncken et al., 2021). This assumption is also consistent with values obtained from Coulomb wedge theory, considering that λ remains constant between the wedge and the megathrust (Adam & Reuther, 2000; Wang & Hu, 2006). With these assumptions, we get the continuous down-dip distribution of $\bar{\sigma}_n$ shown in Fig. 3.1b.

The outer and inner wedge regions exhibit background and foreshock seismicity, indicating a highly fractured environment (Herman et al., 2016; Soto et al., 2019; Storch et al., 2021, Fig. 3.1d), with densities consistent with a mafic composition (Sallarès & Ranero, 2005; Tassara and Echaurren, 2012). Sedimentary deposits are primarily confined to the poorly developed frontal accretionary prism and the slope of the forearc wedge (Geersen et al., 2018). Based on geophysical and geological data, we infer that the offshore crustal fault related to the foreshock sequence cut through mafic rocks of the upper crust. The minimum depth of foreshock and background seismicity indicates velocity weakening behavior below 5 km. We assume the same $a - b$ values as those used for the seismogenic megathrust (Fig. 3.1b), ignoring the sedimentary cover below

the middle and lower slopes. We choose a value of L (Fig. 3.1b) that allows to solve the nucleation size at both faults capturing the seismicity of the seismic cycle.

6.2.3. Stress to strain interactions (S3)

We assume that the oceanic and continental mantle elements are deformed as a viscoelastic medium, where the total anelastic strain-rate is $\dot{\varepsilon_T} = \dot{\varepsilon_M} + \dot{\varepsilon_K}$, in which *M* and *K* denote the Maxwell and Kelvin components (Masuti et al., 2016). To compute the Maxwell strain-rate, we use a power-creep law activated by the temperature distribution within each element in the mesh (Fig. S1), assuming pure dislocation creep over minerals with constant water concentration (Hirth & Kohlstedt, 2003; Karato & Jung, 2010):

$$\dot{\varepsilon_M} = A\sigma^n {C_{OH}}^r d^{-m} exp\left(\frac{-Q+p\Omega}{RT}\right) \qquad \text{eq. 6.2 (1)}$$

where *A* is a pre-exponential factor, σ is the deviatoric stress, C_{OH} is water concentration, *d* is grain size, *Q* is the activation energy, *p* is lithostatic pressure, Ω is activation volume, *R* is the constant of ideal gasses, *T* is the temperature, and *n*, *r*, and *m* are experimentally derived exponents. We assume that *m*=0 to yield an expression independent of the grain size, in which the rest of the parameters are assumed following a wet olivine rheology next to the cold mantle-wedge and a dry olivine rheology elsewhere (Hirth & Kohlstedt, 2003; Karato & Jung, 2010, Table S1 and Fig. S1). Then, we add the Kelvin strain component that describe strain-rate during transient creep:

$$\dot{\varepsilon_K} = A_K q \|q\|^{n-1} (C_{OH})^r d^{-p} exp\left(\frac{-E+p\Omega}{RT}\right) \qquad \text{eq. 6.3 (2)}$$

here A_k is a pre-exponential factor, $q = \sigma - 2G_K\varepsilon_K$ is the effective stress, and G_K is a strain-hardening coefficient. We assume the same values for each parameter on eq. (1) and (2) (Table S1).

Stress to strain interactions during the seismic cycle are obtained assuming a quasi-dynamic approximation, in which stress driven by wave propagation is neglected (Lapusta et al., 2000; Rice, 1993). To compute changes in shear traction and stress

with time, which are dependent on the velocity at the fault surface and on the anelastic strain-rate at each mantle element, we use the code UniCyclE (Barbot, 2018b, 2018a, 2019a, 2019b, 2020; Shi et al., 2020; Wang & Barbot, 2023) which relies on the integral method (Barbot, 2018b; Barbot et al., 2017) that discretize the fault into points while the ductile domain is meshed with surface elements in a cross-section (Fig. S1).

6.2.4. Thermal model (S4)

The thermal field is computed by using the steady-state heat advection-diffusion equation:

$$\rho c_p (v \cdot \nabla) T = \nabla \cdot (k \nabla T) + f \qquad \text{eq. 6.4 (3)}$$

solved in Araya et al. (2023). Here ρ is density, c_p is specific heat, k is thermal conductivity and f is a parameter that describes possible heat sources. Eq. (3) is solved within a 2D subduction framework using the lithospheric structure of Tassara & Echaurren (2012) and assuming the Slab2 model for the geometry of the oceanic plate (Hayes et al., 2018). The final mesh is shown in Fig. S2, where downgoing slab drives flow within the overlying viscous mantle wedge.

Velocity (v) and pressure at the mantle wedge are computed by solving the equations of conservations of mass and momentum. From van Keken et al. (2008) we solved conservation of mass:

$$\nabla \cdot v = 0 \qquad \text{eq. 6.5 (4)}$$

$$\nabla \cdot \tau - \nabla P = 0 \qquad \text{eq. 6.6 (5)}$$

in which τ is the deviatoric stress tensor and P is the dynamic pressure. $\tau = 2\eta\dot{\varepsilon}$, where η is the effective dynamic viscosity and the components of the strain-rate tensor are given by:

$$\dot{\varepsilon}_{ij} = \frac{1}{2}\left(\frac{\partial v_i}{\partial x_j} + \frac{\partial v_j}{\partial x_i}\right) \qquad \text{eq. 6.7 (6)}$$

and η is obtained by dislocation creep:

$$\eta = A\ exp\left(\frac{Q}{nRT}\right)\dot{\varepsilon}^{\frac{(1-n)}{n}} \qquad \text{eq. 6.8 (7)}$$

using the same rheological parameters as in eq. (1).

Solving the entire system requires the following assumptions: 1) constant temperature at the surface of the mesh (0°C), and at the bottom of the oceanic lithosphere (1450°C). On the slab inflow boundary, we prescribed a geotherm obtained using a half-space cooling model (Turcotte & Schubert, 2014) and considering an age of 48 Myr. At the right edge, we prescribe a geotherm obtained using an adiabatic gradient of 0.4 °C/km and a potential temperature at the mantle of 1300°C. The outflow boundary of the wedge is assumed to have zero heat flux. Finally, eq. (4), (5), and (6) are solved by Araya et al. (2023) using a stabilized finite element that allows the use of equal polynomial interpolation at each unknown point, resulting in the temperature distribution of Fig. S2. That we used as an input in eq. (1) and (2) to obtain the strain-rate in the quasi-dynamic simulations, implying that we interpolate the temperature on the center of each triangle forming the mesh of Fig. S1.

6.2.5 Compute of surface deformation (S5)

To validate our findings, we compare the coseismic surface deformation observed in our simulations with data obtained from the GNSS time series from the Nevada Geodetic Laboratory (Blewitt et al., 2018). We calculate the coseismic displacement (Fig. 3.1a) resulting from the Iquique mainshock using an extended trajectory model (Bevis et al., 2019; Bevis & Brown, 2014). During the precursory phase, we juxtapose previously published foreshock activity (Schurr et al., 2020; Sippl et al., 2018; Sippl et al. 2023) against model-generated seismicity preceding each earthquake that features similar rupture lengths and epicenter locations as the Iquique event. Furthermore, we investigate the influence of different mean background hydraulic states by systematically alternating λ resulting in varying $\overline{\sigma}_n$ distributions along the megathrust (Supplementary Material Fig. S3).

6.2.6 Supplementary Figures

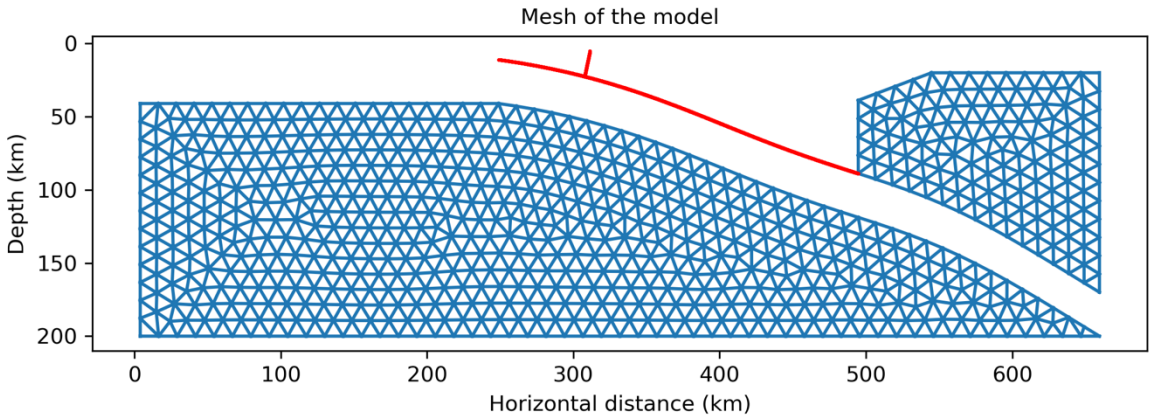

Figure 6.6 (S1). Mesh of the quasi-dynamic modeling.

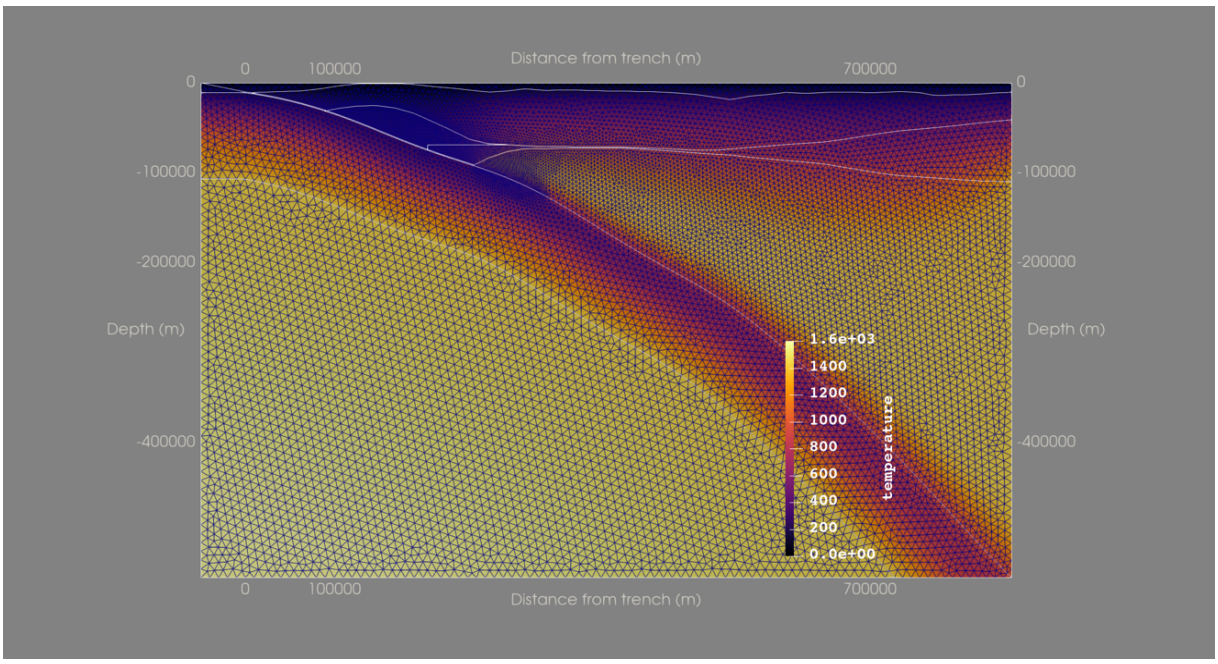

Figure 6.7 (S2). **Mesh of thermal model and temperature distribution at 20°S**. White lines denote the limits of the lithosphere following Tassara & Echaurren (2012), that were assumed to compute the model.

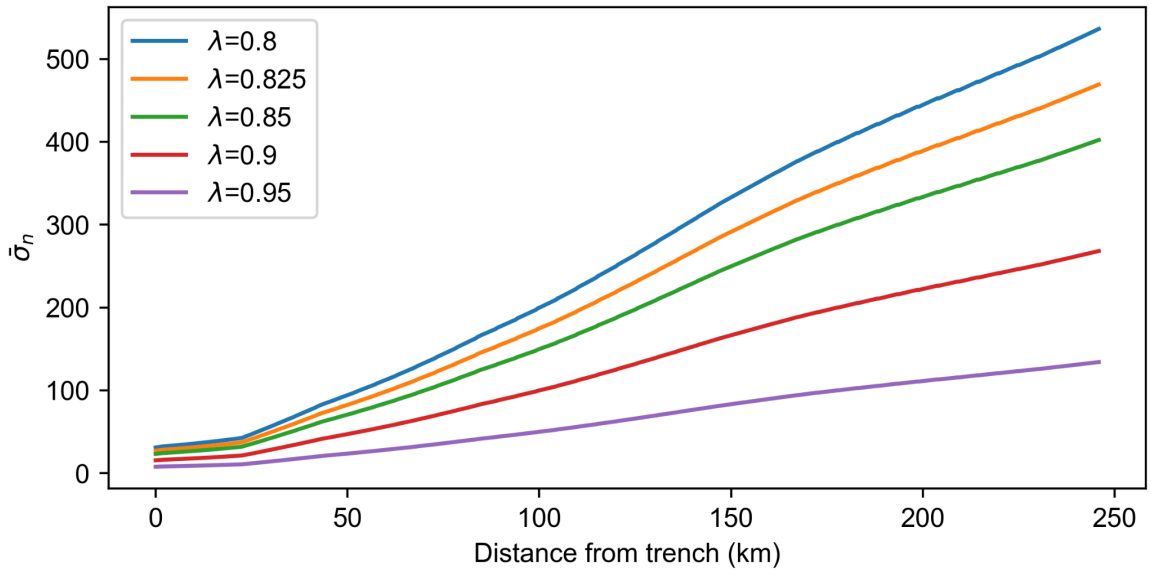

Figure 6.8 (S3). Distribution of effective normal stress along the dip of the megathrust as a result of changes in λ.

6.2.7 Supplementary tables

Power-law parameters							
Domain	***A*** **(Mpa-n s-1)**	C_{oh} **(ppm H/Si)**	***n***	***R***	***Ω***	***Q*** **(kJ/mol)**	***r***
Oceanic Mantle	3.631	1000	3	8.314	1.30E-05	5.10E+05	1.2
Continental Mantle (dry)	3.631	1000	3	8.314	1.30E-05	5.10E+05	1.2
Continental Mantle (wet)	3.631	1500	3	8.314	1.10E-05	4.75E+05	1.2
Thermal parameters							
Domain	***k*** **(W/mK)**	***ρ*** **(kg/m^3)**	c_p **(J/kg K)**		***f*** **(W/m^3)**		
Upper Crust	3	3300	1000		1.3.E-06		
Lower Crust	3	3300	1000		4.0.E-07		
Lithospheric Mantle	3	3300	1000		2.0.E-08		
Oceanic Crust	3	3300	1000		2.0.E-08		

Table 6.4 (S1). Power-creep law parameters for equations (1), (2) and (7). Thermal parameters for equation (3).

Domain	***μ***	***L*** **(m)**	**σ (MPa)**	***a***	***b***	***a-b***	***a/b***	***W*** **(km)**
Offshore UPF (VS)	0.6	1.00E-02	10	1.08E-02	8.45E-03	2.35E-03	1.28E+00	4
Offshore UPF (VW)	0.6	2.50E-03	10	2.41E-02	2.75E-02	-3.35E-03	8.78E-01	9
	μ	***L*** **(m)**	***λ***	***a***	***b***	***a-b***	***a/b***	***W*** **(km)**
VS (below outer wedge)	0.6	5.00E-02	0.825	1.08E-02	8.45E-03	2.35E-03	1.28E+00	38
VW	0.6	1.25E-02	0.825	2.41E-02	2.75E-02	-3.35E-03	8.78E-01	135
VS (below central depression)	0.4	5.00E-02	0.825	1.00E-02	5.00E-03	5.00E-03	2.00E+00	86

Table 6.5 (S2). Frictional properties of the slip-rate- and state- friction law at the megathrust and the offshore upper-plate fault (Offshore UPF). Transition from *a* and *b* at each segment is made using a linear interpolation.

6.2.7 Supplementary references

Adam, J., & Reuther, C.-D. (2000). Crustal dynamics and active fault mechanics during subduction erosion. Application of frictional wedge analysis on to the North Chilean Forearc. Tectonophysics, 321(3), 297–325. https://doi.org/10.1016/S0040-1951(00)00074-3

Araya, R., Cárcamo, C., & Poza, A. H. (2023). A stabilized finite element method for the Stokes–Temperature coupled problem. Applied Numerical Mathematics, 187, 24–49. https://doi.org/10.1016/j.apnum.2023.02.002

Barbot, S. (2018a). Asthenosphere Flow Modulated by Megathrust Earthquake Cycles. Geophysical Research Letters, 45(12), 6018–6031. https://doi.org/10.1029/2018GL078197

Barbot, S. (2018b). Deformation of a Half-Space from Anelastic Strain Confined in a Tetrahedral Volume. Bulletin of the Seismological Society of America, 108(5A), 2687–2712. https://doi.org/10.1785/0120180058

Barbot, S. (2019a). Modulation of fault strength during the seismic cycle by grain-size evolution around contact junctions. Tectonophysics, 765, 129–145. https://doi.org/10.1016/j.tecto.2019.05.004

Barbot, S. (2019b). Slow-slip, slow earthquakes, period-two cycles, full and partial ruptures, and deterministic chaos in a single asperity fault. Tectonophysics, 768, 228171. https://doi.org/10.1016/j.tecto.2019.228171

Barbot, S. (2020). Frictional and structural controls of seismic super-cycles at the Japan trench. Earth, Planets and Space, 72(1), 63. https://doi.org/10.1186/s40623-020-01185-3

Barbot, S., Moore, J. D. P., & Lambert, V. (2017). Displacement and Stress Associated with Distributed Anelastic Deformation in a Half-Space. Bulletin of the Seismological Society of America, 107(2), 821–855. https://doi.org/10.1785/0120160237

Bevis, M., & Brown, A. (2014). Trajectory models and reference frames for crustal motion geodesy. Journal of Geodesy, 88(3), 283–311. https://doi.org/10.1007/s00190-013-0685-5

Bevis, M., Bedford, J., & Caccamise II, D. J. (2019). The Art and Science of Trajectory Modelling (pp. 1–27). https://doi.org/10.1007/978-3-030-21718-1_1

Blewitt, G., Hammond, W., & Kreemer, C. (2018). Harnessing the GPS Data Explosion for Interdisciplinary Science. Eos, 99. https://doi.org/10.1029/2018EO104623

Carretier, S., Tolorza, V., Regard, V., Aguilar, G., Bermúdez, M. A., Martinod, J., et al. (2018). Review of erosion dynamics along the major N-S climatic gradient in Chile and perspectives. Geomorphology, 300, 45–68. https://doi.org/10.1016/j.geomorph.2017.10.016

Comte, D., Carrizo, D., Roecker, S., Ortega-Culaciati, F., & Peyrat, S. (2016). Three-dimensional elastic wave speeds in the northern Chile subduction zone: variations in hydration in the supraslab mantle. Geophysical Journal International, 207(2), 1080–1105. https://doi.org/10.1093/gji/ggw318

Dieterich, J. H. (1979), Modeling of rock friction: 2. Simulation of preseismic slip, J. Geophys. Res., 84(B5), 2169–2175, doi:10.1029/JB084iB05p02169.

Geersen, J., Ranero, C. R., Klaucke, I., Behrmann, J. H., Kopp, H., Tréhu, A. M., et al. (2018). Active Tectonics of the North Chilean Marine Forearc and Adjacent Oceanic Nazca Plate. Tectonics, 37(11), 4194–4211. https://doi.org/10.1029/2018TC005087

Hayes, G. P., Moore, G. L., Portner, D. E., Hearne, M., Flamme, H., Furtney, M., & Smoczyk, G. M. (2018). Slab2, a comprehensive subduction zone geometry model. Science, 362(6410), 58–61. https://doi.org/10.1126/SCIENCE.AAT4723/SUPPL_FILE/AAT4723-HAYES-SM.PDF

Herman, M. W., Furlong, K. P., Hayes, G. P., & Benz, H. M. (2016). Foreshock triggering of the 1 April 2014 Mw 8.2 Iquique, Chile, earthquake. Earth and Planetary Science Letters, 447, 119–129. https://doi.org/10.1016/j.epsl.2016.04.020

Hirth, G., & Kohlstedt, D. (2003). Rheology of the upper mantle and the mantle wedge: A view from the experimentalists (pp. 83–105). https://doi.org/10.1029/138GM06

Jolivet R., Simons, M., Duputel, Z., Olive, J.-A., Bhat, H. S., & Bletery, Q. (2020). Interseismic loading of subduction megathrust drives long-term uplift in Northern Chile. Geophysical Research Letters, 47, e2019GL085377. https://doi.org/10.1029/2019GL085377

Karato, S. I., & Jung, H. (2010). Effects of pressure on high-temperature dislocation creep in olivine. https://doi.org/10.1080/0141861021000025829, 83(3), 401–414. Retrieved from https://www.tandfonline.com/doi/abs/10.1080/0141861021000025829

van Keken, P. E., Currie, C., King, S. D., Behn, M. D., Cagnioncle, A., He, J., et al. (2008). A community benchmark for subduction zone modeling. Physics of the Earth and Planetary Interiors, 171(1–4), 187–197. https://doi.org/10.1016/j.pepi.2008.04.015

Kober, F., Ivy-Ochs, S., Schlunegger, F., Baur, H., Kubik, P. W., & Wieler, R. (2007). Denudation rates and a topography-driven rainfall threshold in northern Chile: Multiple cosmogenic nuclide data and sediment yield budgets. Geomorphology, 83(1–2), 97–120. https://doi.org/10.1016/j.geomorph.2006.06.029

Lapusta, N., Rice, J. R., Ben-Zion, Y., & Zheng, G. (2000). Elastodynamic analysis for slow tectonic loading with spontaneous rupture episodes on faults with rate- and state-dependent friction. Journal of Geophysical Research: Solid Earth, 105(B10), 23765–23789. https://doi.org/10.1029/2000JB900250

Li, S., Moreno, M., Bedford, J., Rosenau, M., & Oncken, O. (2015). Revisiting viscoelastic effects on interseismic deformation and locking degree: A case study of the Peru-North Chile subduction zone.

Journal of Geophysical Research: Solid Earth, 120(6), 4522–4538. https://doi.org/10.1002/2015JB011903

Maksymowicz, A., Ruiz, J., Vera, E., Contreras-Reyes, E., Ruiz, S., Arraigada, C., et al. (2018). Heterogeneous structure of the Northern Chile marine forearc and its implications for megathrust earthquakes. Geophysical Journal International, 215(2), 1080–1097. https://doi.org/10.1093/gji/ggy325

Masuti, S., Barbot, S. MCMC inversion of the transient and steady-state creep flow law parameters of dunite under dry and wet conditions. Earth Planets Space 73, 208 (2021). https://doi.org/10.1186/s40623-021-01543-9

Masuti, S., Barbot, S. D., Karato, S., Feng, L., & Banerjee, P. (2016). Upper-mantle water stratification inferred from observations of the 2012 Indian Ocean earthquake. Nature, 538(7625), 373–377. https://doi.org/10.1038/nature19783

Moore, D. E., & Lockner, D. A. (2011). Frictional strengths of talc-serpentine and talc-quartz mixtures. Journal of Geophysical Research, 116(B1), B01403. https://doi.org/10.1029/2010JB007881

Okazaki, K., & Katayama, I. (2015). Slow stick slip of antigorite serpentinite under hydrothermal conditions as a possible mechanism for slow earthquakes. Geophysical Research Letters, 42(4), 1099–1104. https://doi.org/10.1002/2014GL062735

Oncken, O., Angiboust, S., & Dresen, G. (2021). Slow slip in subduction zones: Reconciling deformation fabrics with instrumental observations and laboratory results. Geosphere, 18(1), 104–129. https://doi.org/10.1130/GES02382.1

Petersen, F., Lange, D., Ma, B., Grevemeyer, I., Geersen, J., Klaeschen, D., et al. (2021). Relationship Between Subduction Erosion and the Up-Dip Limit of the 2014 Mw 8.1 Iquique Earthquake. Geophysical Research Letters, 48(9). https://doi.org/10.1029/2020GL092207

Rice, J. R. (1993). Spatio-temporal complexity of slip on a fault. Journal of Geophysical Research: Solid Earth, 98(B6), 9885–9907. https://doi.org/10.1029/93JB00191

Ruina, A. (1983), Slip instability and state variable friction laws, J. Geophys. Res., 88(B12), 10359–10370, doi:10.1029/JB088iB12p10359.

Sallarès, V., & Ranero, C. R. (2005). Structure and tectonics of the erosional convergent margin off Antofagasta, north Chile (23°30′S). Journal of Geophysical Research: Solid Earth, 110(B6). https://doi.org/10.1029/2004JB003418

Schurr, B., Moreno, M., Tréhu, A. M., Bedford, J., Kummerow, J., Li, S., & Oncken, O. (2020). Forming a Mogi Doughnut in the Years Prior to and Immediately Before the 2014 M 8.1 Iquique, Northern Chile, Earthquake. Geophysical Research Letters, 47(16). https://doi.org/10.1029/2020GL088351

Shi, Q., Barbot, S., Wei, S., Tapponnier, P., Matsuzawa, T., & Shibazaki, B. (2020). Structural control and system-level behavior of the seismic cycle at the Nankai Trough. Earth, Planets and Space, 72(1), 27. https://doi.org/10.1186/s40623-020-1145-0

Sippl, C., Schurr, B., Asch, G., & Kummerow, J. (2018). Seismicity Structure of the Northern Chile Forearc From >100,000 Double-Difference Relocated Hypocenters. Journal of Geophysical Research: Solid Earth, 123(5), 4063–4087. https://doi.org/10.1002/2017JB015384

Sippl, C., Schurr, B., Münchmeyer, J., Barrientos, S., & Oncken, O. (2023). The Northern Chile forearc constrained by 15 years of permanent seismic monitoring. Journal of South American Earth Sciences, 104326. https://doi.org/10.1016/j.jsames.2023.104326

Soto, H., Sippl, C., Schurr, B., Kummerow, J., Asch, G., Tilmann, F., et al. (2019). Probing the Northern Chile Megathrust With Seismicity: The 2014 M8.1 Iquique Earthquake Sequence. Journal of Geophysical Research: Solid Earth, 124(12), 12935–12954. https://doi.org/10.1029/2019JB017794

Storch, I., Buske, S., Victor, P., & Oncken, O. (2021). Seismic images of the Northern Chilean subduction zone at 19°40′S, prior to the 2014 Iquique earthquake. Geophysical Journal International, 225(2), 1048–1061. https://doi.org/10.1093/gji/ggab035

Tassara, A., & Echaurren, A. (2012). Anatomy of the Andean subduction zone: three-dimensional density model upgraded and compared against global-scale models. Geophysical Journal International, 189(1), 161–168. https://doi.org/10.1111/j.1365-246X.2012.05397.x

Takahashi, M., Uehara, S.-I., Mizoguchi, K., Shimizu, I., Okazaki, K., & Masuda, K. (2011). On the transient response of serpentine (antigorite) gouge to stepwise changes in slip velocity under high-temperature conditions. Journal of Geophysical Research, 116(B10), B10405. https://doi.org/10.1029/2010JB008062

Turcotte, D., & Schubert, G. (2014). Geodynamics. Cambridge University Press. https://doi.org/10.1017/CBO9780511843877

Wang, B., & Barbot, S. (2023). Pulse-like ruptures, seismic swarms, and tremorgenic slow-slip events with thermally activated friction. Earth and Planetary Science Letters, 603, 117983. https://doi.org/10.1016/j.epsl.2022.117983

Wang, K., & Hu, Y. (2006). Accretionary prisms in subduction earthquake cycles: The theory of dynamic Coulomb wedge. Journal of Geophysical Research: Solid Earth, 111(B6). https://doi.org/10.1029/2005JB004094

Zhang, L., He, C., Liu, Y., & Lin, J. (2017). Frictional properties of the South China Sea oceanic basalt and implications for strength of the Manila subduction seismogenic zone. Marine Geology, 394, 16–29. https://doi.org/10.1016/j.margeo.2017.05.006

6.3 Supplementary Material of the Thesis

Here it is attached the supplementary material used in the rest of the chapters that were not submitted for publication.

Mineral or rock	a-b	μ	T(°C)	σ	Reference
alt-basalt	-4.00E-03	0.65	150	120	Phillips et al. (2020)
alt-basalt (<1μm/s)	-2.50E-03	0.65	25	25	Ikari et al. (2020)
alt-basalt (>10μm/s)	5.00E-03	0.65	25	25	Ikari et al. (2020)
alt-basalt	1.96E-03	0.6	100	100	Okuda et al. (2023)
alt-basalt	-1.97E-03	0.6	200	100	Okuda et al. (2023)
alt-basalt	-5.86E-03	0.6	250	100	Okuda et al. (2023)
alt-basalt	-4.45E-03	0.6	300	100	Okuda et al. (2023)
alt-basalt	-1.37E-02	0.6	350	100	Okuda et al. (2023)
alt-basalt	-9.08E-03	0.6	400	100	Okuda et al. (2023)
alt-basalt	-1.11E-02	0.6	450	100	Okuda et al. (2023)
alt-basalt	3.42E-03	0.55	500	100	Okuda et al. (2023)
alt-basalt	2.68E-02	0.45	550	100	Okuda et al. (2023)
blueschist	5.00E-03	0.7	100	75	Sawai et al. (2016)

blueschist	-7.50E-03	0.7	200	75	Sawai et al. (2016)
blueschist	5.00E-03	0.6	300	75	Sawai et al. (2016)
blueschist	-1.00E-03	0.6	400	75	Sawai et al. (2016)
blueschist	-5.00E-03	0.7	100	50	Sawai et al. (2016)
blueschist	-2.50E-03	0.7	200	50	Sawai et al. (2016)
blueschist	-5.00E-03	0.6	300	50	Sawai et al. (2016)
blueschist	-6.00E-03	0.6	400	50	Sawai et al. (2016)
blueschist	1.00E-03	0.7	100	100	Sawai et al. (2016)
blueschist	-2.50E-03	0.7	200	100	Sawai et al. (2016)
blueschist	1.15E-02	0.6	300	100	Sawai et al. (2016)
blueschist	1.00E-02	0.6	400	100	Sawai et al. (2016)
quartz-talc20%	-3.00E-04	0.5	200	100	Moore et al. (2011)
quartz-montmorillonite50%	1.50E-03	0.2	25	41	Tembe et al. (2010)
quartz-illite50%	3.50E-03	0.45	25	41	Tembe et al. (2010)
quartz-montmorillonite-illite50%	2.00E-03	0.3	25	41	Tembe et al. (2010)
quartz-wet	3.75E-03	0.625	100	150	Masuda et al. (2019)

quartz-wet	-3.00E-03	0.65	300	150	Masuda et al. (2019)
feldespar-wet	2.50E-03	0.7	100	150	Masuda et al. (2019)
feldespar-wet	-1.20E-02	0.65	300	150	Masuda et al. (2019)
granite	-1.00E-03	0.7	100	300	Liu and Rice (2009) Blanpied et al. (1995)
granite	-1.00E-02	0.7	200	300	Liu and Rice (2009) Blanpied et al. (1995)
granite	-1.00E-02	0.7	250	300	Liu and Rice (2009) Blanpied et al. (1995)
granite	-2.50E-03	0.7	300	300	Liu and Rice (2009) Blanpied et al. (1995)
lizardite-talc50%	8.00E-03	0.2	300	100	Moore et al. (2011)
antigorite-talc50%	5.00E-04	0.3	400	100	Moore et al. (2011)
antigorite	1.00E-02	0.5	25	70	Takahashi et al. (2011)
antigorite	3.00E-03	0.55	450	120	Okazaki & Katayama (2015)
antigorite	1.30E-03	0.55	500	120	Okazaki & Katayama (2015)
antigorite	-5.00E-03	0.65	500	180	Okazaki & Katayama (2015)
antigorite	1.00E-03	0.55	400	120	Okazaki & Katayama (2015)
antigorite	1.00E-03	0.55	400	180	Okazaki & Katayama (2015)

antigorite	-4.80E-03	0.55	550	180	Okazaki & Katayama (2015)
antigorite	-4.80E-03	0.55	550	120	Okazaki & Katayama (2015)
antigorite	-2.70E-03	0.55	600	180	Okazaki & Katayama (2015)
antigorite	-2.00E-03	0.55	650	120	Okazaki & Katayama (2015)
smectite (10 μm/s)	-1.40E-03	0.25	25	5	Saffer & Marone (2003)
smectite (10 μm/s)	-1.30E-03	0.25	25	10	Saffer & Marone (2003)
smectite (10 μm/s)	-1.30E-03	0.25	25	15	Saffer & Marone (2003)
smectite (10 μm/s)	-6.00E-04	0.25	25	25	Saffer & Marone (2003)
smectite (10 μm/s)	-7.00E-04	0.25	25	30	Saffer & Marone (2003)
smectite (10 μm/s)	-1.00E-04	0.25	25	35	Saffer & Marone (2003)
smectite (100 μm/s)	1.00E-03	0.25	25	5	Saffer & Marone (2003)
smectite (100 μm/s)	8.00E-04	0.25	25	10	Saffer & Marone (2003)
smectite (100 μm/s)	1.10E-03	0.25	25	15	Saffer & Marone (2003)
smectite (100 μm/s)	1.90E-03	0.25	25	25	Saffer & Marone (2003)
smectite (100 μm/s)	2.20E-03	0.25	25	30	Saffer & Marone (2003)
smectite (100 μm/s)	1.80E-03	0.25	25	35	Saffer & Marone (2003)

smectite-quartz50%	8.00E-04	0.4	25	25	Saffer & Marone (2003)
illite	2.70E-03	0.55	25	5	Saffer & Marone (2003)
illite	3.30E-03	0.55	25	10	Saffer & Marone (2003)
illite	2.40E-03	0.55	25	20	Saffer & Marone (2003)
illite	2.80E-03	0.55	25	25	Saffer & Marone (2003)
illite	2.50E-03	0.55	25	40	Saffer & Marone (2003)
illite	3.10E-03	0.55	25	50	Saffer & Marone (2003)
illite	3.10E-03	0.55	25	75	Saffer & Marone (2003)

Supplementary Material Table 6.6. Compilation of frictional properties on minerals.

model	**segment**	**a**	**b**	**a-b**	**a/b**	**μ**	**λ**	**L**	**W**	**Rock**
	VS	1.00E-02	8.00E-03	2.00E-03	1.25E+00	4.00E-01	0.825	5.00E-02	0.00E+00	quartz-montmorillonite-illite50%
	VW	1.00E-02	1.01E-02	-1.00E-04	9.90E-01	2.50E-01	0.825	1.00E-02	1.04E+05	smectite (10 μm/s)
SSE_m1	VS	1.00E-02	7.00E-03	3.00E-03	1.43E+00	5.50E-01	0.825	5.00E-02	0.00E+00	antigorite (450,180)
model	**segment**	**a**	**b**	**a-b**	**a/b**	**μ**	**λ**	**L**	**W**	**Rock**

	VS	1.00E-02	8.00E-03	2.00E-03	1.25E+00	4.00E-01	0.825	5.00E-02	0.00E+00	quartz-montmorillonite-illite50%
	VW	1.00E-02	1.03E-02	-3.00E-04	9.71E-01	5.00E-01	0.825	1.00E-02	1.04E+05	quartz-talc20%
SSE_m2	VS	1.00E-02	7.00E-03	3.00E-03	1.43E+00	5.50E-01	0.825	5.00E-02	0.00E+00	antigorite (450,180)
model	**segment**	**a**	**b**	**a-b**	**a/b**	**μ**	**λ**	**L**	**W**	**Rock**
	VS	1.00E-02	8.00E-03	2.00E-03	1.25E+00	4.00E-01	0.825	5.00E-02	0.00E+00	quartz-montmorillonite-illite50%
	VW	6.00E-03	8.50E-03	-2.50E-03	7.06E-01	7.00E-01	0.825	1.00E-02	1.04E+05	blueschist (200,100)
FULLRUP_m1	VS	1.00E-02	7.00E-03	3.00E-03	1.43E+00	5.50E-01	0.825	5.00E-02	0.00E+00	antigorite (450,180)
model	**segment**	**a**	**b**	**a-b**	**a/b**	**μ**	**λ**	**L**	**W**	**Rock**
	VS	1.00E-02	8.00E-03	2.00E-03	1.25E+00	4.00E-01	0.825	5.00E-02	0.00E+00	quartz-montmorillonite-illite50%
	VW	7.50E-03	1.50E-02	-7.50E-03	5.00E-01	7.00E-01	0.825	1.00E-02	1.04E+05	blueschist (200,75)
FULLRUP_m2	VS	1.00E-02	7.00E-03	3.00E-03	1.43E+00	5.50E-01	0.825	5.00E-02	0.00E+00	antigorite (450,180)
model	segment	a	b	a-b	a/b	μ	λ	L	W	Rock

	VS	1.00E-02	8.00E-03	2.00E-03	1.25E+00	4.00E-01	0.825	5.00E-02	0.00E+00	quartz-montmorillonite-illite50%
	VW	1.00E-02	1.30E-02	-3.00E-03	7.69E-01	6.25E-01	0.825	1.00E-02	1.04E+05	quartz wet (300,150)
FULLRUP_m3	VS	1.00E-02	7.00E-03	3.00E-03	1.43E+00	5.50E-01	0.825	5.00E-02	0.00E+00	antigorite (450,180)
model	**segment**	**a**	**b**	**a-b**	**a/b**	**μ**	**λ**	**L**	**W**	**Rock**
	VS	1.00E-02	8.00E-03	2.00E-03	1.25E+00	4.00E-01	0.825	5.00E-02	0.00E+00	quartz-montmorillonite-illite50%
	VW	1.00E-02	2.20E-02	-1.20E-02	4.55E-01	6.50E-01	0.825	1.00E-02	1.04E+05	feldspar wet (300,150)
FULLRUP_m4	VS	1.00E-02	7.00E-03	3.00E-03	1.43E+00	5.50E-01	0.825	5.00E-02	0.00E+00	antigorite (450,180)
model	**segment**	**a**	**b**	**a-b**	**a/b**	**μ**	**λ**	**L**	**W**	**Rock**
	VS	1.00E-02	8.00E-03	2.00E-03	1.25E+00	4.00E-01	0.825	5.00E-02	0.00E+00	quartz-montmorillonite-illite50%
	VW	1.00E-02	2.20E-02	-1.20E-02	4.55E-01	6.50E-01	0.985	1.00E-02	1.04E+05	feldspar wet (300,150)
FULLRUP_SIGMAVAR_m4	VS	1.00E-02	7.00E-03	3.00E-03	1.43E+00	5.50E-01	0.825	5.00E-02	0.00E+00	antigorite (450,180)
model	**segment**	**a**	**b**	**a-b**	**a/b**	**μ**	**λ**	**L**	**W**	**Rock**

	VS	1.00E-02	8.00E-03	2.00E-03	1.25E+00	4.00E-01	0.825	5.00E-02	0.00E+00	quartz-montmorillonite-illite50%
	VW	1.00E-02	1.30E-02	-3.00E-03	7.69E-01	6.25E-01	0.985	1.00E-02	1.04E+05	quartz wet (300,150)
FULLRUP_SIGMA VAR_m4	VS	1.00E-02	7.00E-03	3.00E-03	1.43E+00	5.50E-01	0.825	5.00E-02	0.00E+00	antigorite (450,180)

Supplementary Material Table 6.7. Frictional properties used on each simulation at Southern Chile.

model	**segment**	**a**	**b**	**a-b**	**a/b**	**μ**	**λ**	**L**	**W**	**Rock**
	VS	1.00E-02	5.00E-03	5.00E-03	2.00E+00	6.50E-01	0.825	5.00E-02	0.00E+00	altered basalt (25,25)
	VW	1.00E-02	1.01E-02	-1.00E-04	9.90E-01	2.50E-01	0.825	1.00E-02	1.04E+05	smectite (10 μm/s)
SSE_m1	VS	1.00E-02	7.00E-03	3.00E-03	1.43E+00	5.50E-01	0.825	5.00E-02	0.00E+00	antigorite (450,180)
model	**segment**	**a**	**b**	**a-b**	**a/b**	**μ**	**λ**	**L**	**W**	**Rock**
	VS	1.00E-02	5.00E-03	5.00E-03	2.00E+00	6.50E-01	0.825	5.00E-02	0.00E+00	altered basalt (25,25)
	VW	1.00E-02	1.14E-02	-1.40E-03	8.77E-01	2.50E-01	0.825	1.00E-02	1.04E+05	smectite (10 μm/s)
SSE_m3	VS	1.00E-02	7.00E-03	3.00E-03	1.43E+00	5.50E-01	0.825	5.00E-02	0.00E+00	antigorite (450,180)

model	segment	a	b	a-b	a/b	μ	λ	L	W	Rock
	VS	1.00 E-02	5.00 E-03	5.00 E-03	2.00 E+00	6.50 E-01	0.825	5.00 E-02	0.00 E+00	altered basalt (25,25)
	VW	1.00 E-02	1.20 E-02	-1.97 E-03	8.35 E-01	6.00 E-01	0.825	1.00 E-02	1.04 E+05	altered basalt (275,100) (average between 250 and 300 T)
SSE_m2	VS	1.00 E-02	7.00 E-03	3.00 E-03	1.43 E+00	5.50 E-01	0.825	5.00 E-02	0.00 E+00	antigorite (450,180)
model	**segment**	**a**	**b**	**a-b**	**a/b**	**μ**	**λ**	**L**	**W**	**Rock**
	VS	1.00 E-02	5.00 E-03	5.00 E-03	2.00 E+00	6.50 E-01	0.825	5.00 E-02	0.00 E+00	altered basalt (25,25)
	VW	1.00 E-02	1.59 E-02	-5.86 E-03	6.31 E-01	6.00 E-01	0.825	1.00 E-02	1.04 E+05	altered basalt (275,100) (average between 250 and 300 T)
FULLRUP_m1	VS	1.00 E-02	7.00 E-03	3.00 E-03	1.43 E+00	5.50 E-01	0.825	5.00 E-02	0.00 E+00	antigorite (450,180)
model	**segment**	**a**	**b**	**a-b**	**a/b**	**μ**	**λ**	**L**	**W**	**Rock**
	VS	1.00 E-02	5.00 E-03	5.00 E-03	2.00 E+00	6.50 E-01	0.825	5.00 E-02	0.00 E+00	altered basalt (25,25)
	VW	6.00 E-03	8.50 E-03	-2.50 E-03	7.06 E-01	7.00 E-01	0.825	1.00 E-02	1.04 E+05	blueschist (200,100)
FULLRUP_m2	VS	1.00 E-02	7.00 E-03	3.00 E-03	1.43 E+00	5.50 E-01	0.825	5.00 E-02	0.00 E+00	antigorite (450,180)

model	segment	a	b	a-b	a/b	μ	λ	L	W	Rock
	VS	1.00 E-02	5.00 E-03	5.00 E-03	2.00 E+00	6.50 E-01	0.825	5.00 E-02	0.00 E+00	altered basalt (25,25)
	VW	7.50 E-03	1.50 E-02	-7.50 E-03	5.00 E-01	7.00 E-01	0.825	1.00 E-02	1.04 E+05	blueschist (200,75)
FULLRUP_m3	VS	1.00 E-02	7.00 E-03	3.00 E-03	1.43 E+00	5.50 E-01	0.825	5.00 E-02	0.00 E+00	antigorite (450,180)
model	**segment**	**a**	**b**	**a-b**	**a/b**	**μ**	**λ**	**L**	**W**	**Rock**
	VS	1.00 E-02	5.00 E-03	5.00 E-03	2.00 E+00	6.50 E-01	0.825	5.00 E-02	0.00 E+00	altered basalt (25,25)
	VW	1.00 E-02	1.59 E-02	-5.86 E-03	6.31 E-01	6.00 E-01	0.985	1.00 E-02	1.04 E+05	altered basalt (275,100) (average between 250 and 300 T)
FULLRUP_SIGMAVAR_m1	VS	1.00 E-02	7.00 E-03	3.00 E-03	1.43 E+00	5.50 E-01	0.825	5.00 E-02	0.00 E+00	antigorite (450,180)
model	**segment**	**a**	**b**	**a-b**	**a/b**	**μ**	**λ**	**L**	**W**	**Rock**
	VS	1.00 E-02	5.00 E-03	5.00 E-03	2.00 E+00	6.50 E-01	0.825	5.00 E-02	0.00 E+00	altered basalt (25,25)
	VW	7.50 E-03	1.50 E-02	-7.50 E-03	5.00 E-01	7.00 E-01	0.985	1.00 E-02	1.04 E+05	blueschist (200,75)
FULLRUP_SIGMAVAR_m2	VS	1.00 E-02	7.00 E-03	3.00 E-03	1.43 E+00	5.50 E-01	0.825	5.00 E-02	0.00 E+00	antigorite (450,180)

Supplementary Material Table 6.8. Frictional properties used on each simulation at Southern Chile.

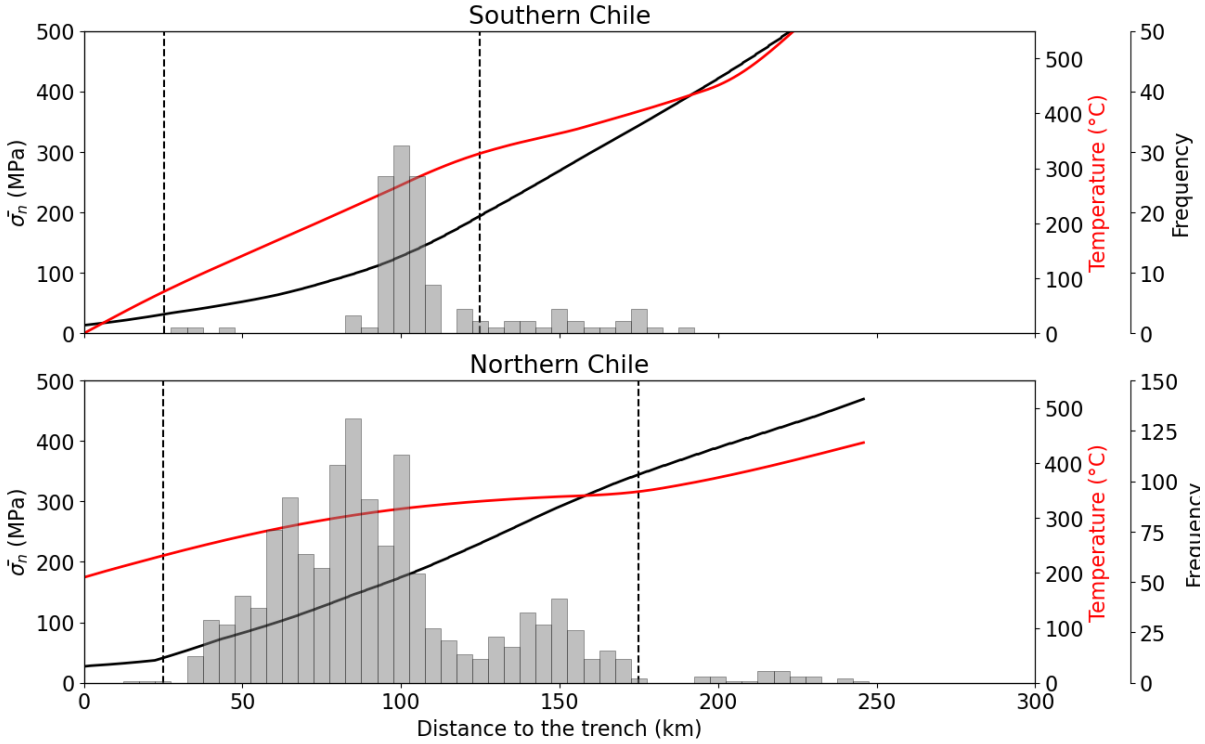

Supplementary Material Figure 6.9. Effective normal stress, temperature and seismicity distribution in Northern and Southern Chile.

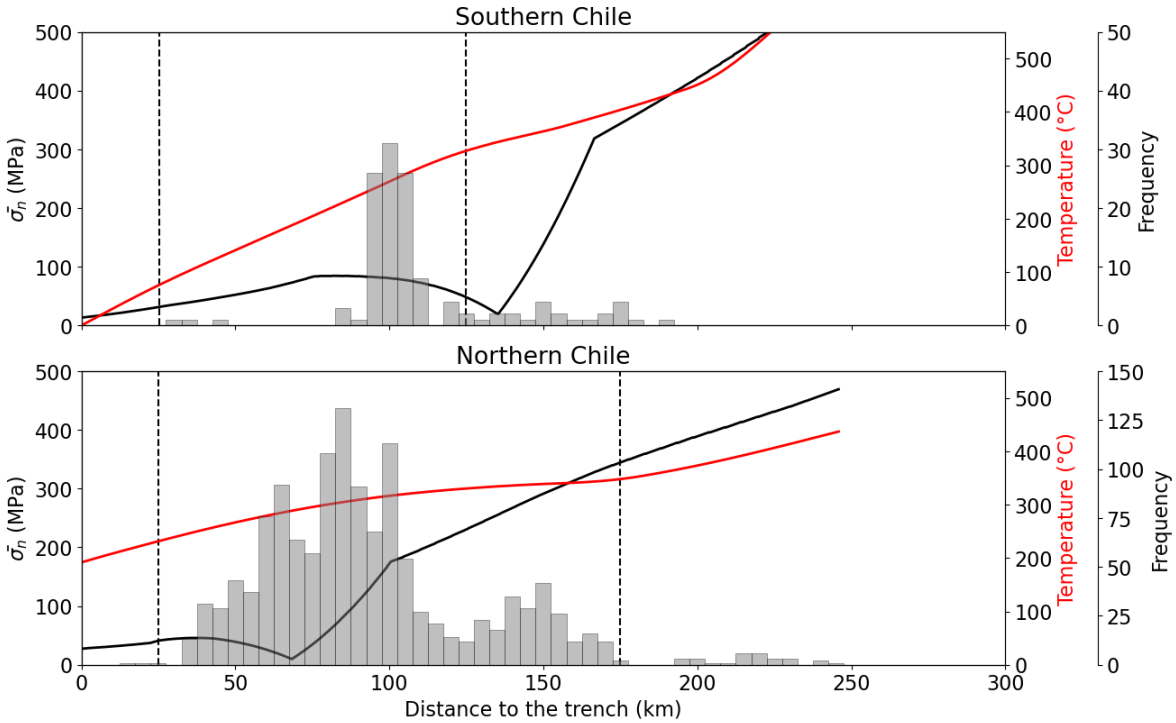

Supplementary Material Figure 6.10. Effective normal stress, temperature and seismicity distribution in Northern and Southern Chile as a result on λ pertubation. A λ perturbation has been induced going from a mean value of 0.825 up to 0.985, which is then manifested in the decrease of the effective normal stress at that region.

7 Main references

7.1 Thesis references

Andrews, D. J. (1978). Coupling of energy between tectonic processes and earthquakes. *Journal of Geophysical Research: Solid Earth*, *83*(B5), 2259–2264. https://doi.org/10.1029/JB083iB05p02259

Angiboust, S., Wolf, S., Burov, E., Agard, P., & Yamato, P. (2012). Effect of fluid circulation on subduction interface tectonic processes: Insights from thermo-mechanical numerical modelling. *Earth and Planetary Science Letters*, *357–358*, 238–248. https://doi.org/10.1016/j.epsl.2012.09.012

Araya, R., Cárcamo, C., & Poza, A. H. (2023). A stabilized finite element method for the Stokes–Temperature coupled problem. *Applied Numerical Mathematics*, *187*, 24–49. https://doi.org/10.1016/j.apnum.2023.02.002

Assumpção, M., Feng, M., Tassara, A., & Julià, J. (2013). Models of crustal thickness for South America from seismic refraction, receiver functions and surface wave tomography. *Tectonophysics*, *609*, 82–96. https://doi.org/10.1016/j.tecto.2012.11.014

Avouac, J. P. (2015). From geodetic imaging of seismic and aseismic fault slip to dynamic modeling of the seismic cycle. *Annual Review of Earth and Planetary Sciences*, *43*, 233–271. https://doi.org/10.1146/annurev-earth-060614-105302

Avouac, J.-P. (2015). From Geodetic Imaging of Seismic and Aseismic Fault Slip to Dynamic Modeling of the Seismic Cycle. *Annual Review of Earth and Planetary Sciences*, *43*(1), 233–271. https://doi.org/10.1146/annurev-earth-060614-105302

Barbot, S. (2018a). Asthenosphere Flow Modulated by Megathrust Earthquake Cycles. *Geophysical Research Letters*, *45*(12), 6018–6031. https://doi.org/10.1029/2018GL078197

Barbot, S. (2018b). Deformation of a Half-Space from Anelastic Strain Confined in a Tetrahedral Volume. *Bulletin of the Seismological Society of America*, *108*(5A), 2687–2712. https://doi.org/10.1785/0120180058

Barbot, S. (2019a). Modulation of fault strength during the seismic cycle by grain-size evolution around contact junctions. *Tectonophysics*, *765*, 129–145. https://doi.org/10.1016/j.tecto.2019.05.004

Barbot, S. (2019b). Slow-slip, slow earthquakes, period-two cycles, full and partial ruptures, and deterministic chaos in a single asperity fault. *Tectonophysics*, *768*, 228171. https://doi.org/10.1016/J.TECTO.2019.228171

Barbot, S. (2020). Frictional and structural controls of seismic super-cycles at the Japan trench. *Earth, Planets and Space*, *72*(1), 63. https://doi.org/10.1186/s40623-020-01185-3

Barbot, S. (2022). A Rate-, State-, and Temperature-Dependent Friction Law With Competing Healing Mechanisms. *Journal of Geophysical Research: Solid Earth*, *127*(11). https://doi.org/10.1029/2022JB025106

Barbot, S., Moore, J. D. P., & Lambert, V. (2017). Displacement and Stress Associated with Distributed Anelastic Deformation in a Half-Space. *Bulletin of the Seismological Society of America*, *107*(2), 821–855. https://doi.org/10.1785/0120160237

Beck, S. L., Zandt, G., Myers, S. C., Wallace, T. C., Silver, P. G., & Drake, L. (1996). Crustal-thickness variations in the central Andes. *Geology*, *24*(5), 407. https://doi.org/10.1130/0091-7613(1996)024<0407:CTVITC>2.3.CO;2

Bedford, J., Moreno, M., Schurr, B., Bartsch, M., & Oncken, O. (2015). Investigating the final seismic swarm before the Iquique-Pisagua 2014 M_w 8.1 by comparison of continuous GPS and seismic foreshock data. *Geophysical Research Letters*, *42*(10), 3820–3828. https://doi.org/10.1002/2015GL063953

Behr, W. M., & Bürgmann, R. (2021). What's down there? The structures, materials and environment of deep-seated slow slip and tremor. *Philosophical Transactions of the Royal Society A: Mathematical, Physical and Engineering Sciences*, *379*(2193), 20200218. https://doi.org/10.1098/rsta.2020.0218

Bonini, M. (2019). Seismic loading of fault-controlled fluid seepage systems by great subduction earthquakes. *Scientific Reports*, *9*(1), 11332. https://doi.org/10.1038/s41598-019-47686-4

Bürgmann, R. (2018). The geophysics, geology and mechanics of slow fault slip. *Earth and Planetary Science Letters*, *495*, 112–134. https://doi.org/10.1016/j.epsl.2018.04.062

Carretier, S., Tolorza, V., Regard, V., Aguilar, G., Bermúdez, M. A., Martinod, J., et al. (2018). Review of erosion dynamics along the major N-S climatic gradient in Chile and perspectives. *Geomorphology*, *300*, 45–68. https://doi.org/10.1016/j.geomorph.2017.10.016

Cerpa, N. G., Wada, I., & Wilson, C. R. (2017). Fluid migration in the mantle wedge: Influence of mineral grain size and mantle compaction. *Journal of Geophysical Research: Solid Earth*, *122*(8), 6247–6268. https://doi.org/10.1002/2017JB014046

Charrier, R., Pinto, L., & Rodríguez, M. P. (2007). Tectonostratigraphic evolution of the Andean Orogen in Chile. In *The Geology of Chile* (pp. 21–114). The Geological Society of London. https://doi.org/10.1144/GOCH.3

Collettini, C., Niemeijer, A., Viti, C., Smith, S. A. F., & Marone, C. (2011). Fault structure, frictional properties and mixed-mode fault slip behavior. *Earth and Planetary Science Letters*, *311*(3–4), 316–327. https://doi.org/10.1016/J.EPSL.2011.09.020

Condit, C. B., Guevara, V. E., Delph, J. R., & French, M. E. (2020). Slab dehydration in warm subduction zones at depths of episodic slip and tremor. *Earth and Planetary Science Letters*, *552*, 116601. https://doi.org/10.1016/j.epsl.2020.116601

Cortés-Aranda, J., González, J., Molina, D., Astudillo-Sotomayor, L., Tassara, A., Miller, M., et al. (2022). Linking Upper-Plate Fault Reactivation With the Megathrust Earthquake Cycle: The Case of the Northern Chile Outer Forearc (19°S–23°S). *Tectonics*, *41*(11). https://doi.org/10.1029/2021TC006956

Cubas, N., Agard, P., & Tissandier, R. (2022). Earthquake ruptures and topography of the Chilean margin controlled by plate interface deformation. *Solid Earth*, *13*(3), 779–792. https://doi.org/10.5194/se-13-779-2022

Dal Zilio, L., & Gerya, T. (2022). Subduction earthquake cycles controlled by episodic fluid pressure cycling. *Lithos*, *426–427*, 106800. https://doi.org/10.1016/j.lithos.2022.106800

Dal Zilio, L., Hegyi, B., Behr, W., & Gerya, T. (2022). Hydro-mechanical earthquake cycles in a poro-visco-elasto-plastic fluid-bearing fault structure. *Tectonophysics*, *838*, 229516. https://doi.org/10.1016/j.tecto.2022.229516

Dal Zilio, L., Lapusta, N., Avouac, J.-P., & Gerya, T. (2022). Subduction earthquake sequences in a non-linear visco-elasto-plastic megathrust. *Geophysical Journal International*, *229*(2), 1098–1121. https://doi.org/10.1093/gji/ggab521

Dieterich, J. H. (1979). Modeling of rock friction: 1. Experimental results and constitutive equations. *Journal of Geophysical Research: Solid Earth*, *84*(B5), 2161–2168. https://doi.org/10.1029/JB084iB05p02161

Echaurren, A., Encinas, A., Sagripanti, L., Gianni, G., Zambrano, P., Duhart, P., & Folguera, A. (2022). Fore-to-retroarc crustal structure of the north Patagonian margin: How is shortening distributed in Andean-type orogens? *Global and Planetary Change*, *209*, 103734. https://doi.org/10.1016/j.gloplacha.2022.103734

Erickson, B. A., Jiang, J., Barall, M., Lapusta, N., Dunham, E. M., Harris, R., et al. (2020). The Community Code Verification Exercise for Simulating Sequences of Earthquakes and Aseismic Slip (SEAS). *Seismological Research Letters*, *91*(2A), 874–890. https://doi.org/10.1785/0220190248

Folguera, A., Orts, D., Spagnuolo, M., Rojas Vera, E., Litvak, V., Sagripanti, L., et al. (2011). A review of Late Cretaceous to Quaternary palaeogeography of the southern Andes. *Biological Journal of the Linnean Society*, *103*(2), 250–268. https://doi.org/10.1111/j.1095-8312.2011.01687.x

Geersen, J., Ranero, C. R., Klaucke, I., Behrmann, J. H., Kopp, H., Tréhu, A. M., et al. (2018). Active Tectonics of the North Chilean Marine Forearc and Adjacent Oceanic Nazca Plate. *Tectonics*, *37*(11), 4194–4211. https://doi.org/10.1029/2018TC005087

Giambiagi, L. B., Tassara, A., Echaurren, A., Julve, J., Quiroga, R., Barrionuevo, M., et al. (2022). Crustal anatomy and evolution of a subduction-related orogenic system: Insights from the Southern Central Andes (22-35°S). *Earth-Science Reviews*, *232*. https://doi.org/10.1016/j.earscirev.2022.104138

Hainzl, S. (2004). Seismicity patterns of earthquake swarms due to fluid intrusion and stress triggering. *Geophysical Journal International*, *159*(3), 1090–1096. https://doi.org/10.1111/j.1365-246X.2004.02463.x

Hamilton, W. B. (1994). Subduction systems and magmatism. *Geological Society, London, Special Publications*, *81*(1), 3–28. https://doi.org/10.1144/GSL.SP.1994.081.01.02

den Hartog, S. A. M., Niemeijer, A. R., & Spiers, C. J. (2012). New constraints on megathrust slip stability under subduction zone P – T conditions. *Earth and Planetary Science Letters*, *353–354*, 240–252. https://doi.org/10.1016/j.epsl.2012.08.022

Hayes, G. P., Moore, G. L., Portner, D. E., Hearne, M., Flamme, H., Furtney, M., & Smoczyk, G. M. (2018). Slab2, a comprehensive subduction zone geometry model. *Science*, *362*(6410), 58–61. https://doi.org/10.1126/science.aat4723

Herrera, M. T., Crempien, J. G. F., & Cembrano, J. (2023). Complex Crustal Deformation Controlled by the 3D Geometry of the Chile Subduction Zone. *Bulletin of the Seismological Society of America*, *113*(6), 2479–2491. https://doi.org/10.1785/0120230062

Hervé, F., Faundez, V., Calderón, M., Massonne, H.-J., & Willner, A. P. (2007). Metamorphic and plutonic basement complexes. In *The Geology of Chile* (pp. 5–19). The Geological Society of London. https://doi.org/10.1144/GOCH.2

Hirth, G., & Kohlstedt, D. (2003). Rheology of the upper mantle and the mantle wedge: A view from the experimentalists (pp. 83–105). https://doi.org/10.1029/138GM06

Hu, Y., Wang, K., He, J., Klotz, J., & Khazaradze, G. (2004). Three-dimensional viscoelastic finite element model for postseismic deformation of the great 1960 Chile earthquake. *Journal of Geophysical Research: Solid Earth*, *109*(12), 1–14. https://doi.org/10.1029/2004JB003163

von Huene, R., & Scholl, D. W. (1991). Observations at convergent margins concerning sediment subduction, subduction erosion, and the growth of continental crust. *Reviews of Geophysics*, *29*(3), 279–316. https://doi.org/10.1029/91RG00969

von Huene, R., Ranero, C. R., & Vannucchi, P. (2004). Generic model of subduction erosion. *Geology*, *32*(10), 913. https://doi.org/10.1130/G20563.1

Jara-Muñoz, J., Melnick, D., Li, S., Socquet, A., Cortés-Aranda, J., Brill, D., & Strecker, M. R. (2022). The cryptic seismic potential of the Pichilemu blind fault in Chile revealed by off-fault geomorphology. *Nature Communications*, *13*(1), 3371. https://doi.org/10.1038/s41467-022-30754-1

Kaneko, Y., & Fialko, Y. (2011). Shallow slip deficit due to large strike-slip earthquakes in dynamic rupture simulations with elasto-plastic off-fault response. *Geophysical Journal International*, *186*(3), 1389–1403. https://doi.org/10.1111/j.1365-246X.2011.05117.x

Karato, S. I., & Jung, H. (2010). Effects of pressure on high-temperature dislocation creep in olivine. *Https://Doi.Org/10.1080/0141861021000025829*, *83*(3), 401–414. Retrieved from https://www.tandfonline.com/doi/abs/10.1080/0141861021000025829

Kodaira, S., Iidaka, T., Kato, A., Park, J.-O., Iwasaki, T., & Kaneda, Y. (2004). High Pore Fluid Pressure May Cause Silent Slip in the Nankai Trough. *Science*, *304*(5675), 1295–1298. https://doi.org/10.1126/science.1096535

Lapusta, N., & Liu, Y. (2009). Three-dimensional boundary integral modeling of spontaneous earthquake sequences and aseismic slip. *Journal of Geophysical Research: Solid Earth*, *114*(B9). https://doi.org/10.1029/2008JB005934

Lapusta, N., Rice, J. R., Ben-Zion, Y., & Zheng, G. (2000). Elastodynamic analysis for slow tectonic loading with spontaneous rupture episodes on faults with rate- and state-dependent friction. *Journal of Geophysical Research: Solid Earth*, *105*(B10), 23765–23789. https://doi.org/10.1029/2000JB900250

Lay, T., Kanamori, H., Ammon, C. J., Koper, K. D., Hutko, A. R., Ye, L., et al. (2012). Depth-varying rupture properties of subduction zone megathrust faults. *Journal of Geophysical Research: Solid Earth*, *117*(B4). https://doi.org/10.1029/2011JB009133

Lindsey, E. O., Mallick, R., Hubbard, J. A., Bradley, K. E., Almeida, R. V., Moore, J. D. P., et al. (2021). Slip rate deficit and earthquake potential on shallow megathrusts. *Nature Geoscience*, *14*(5), 321–326. https://doi.org/10.1038/s41561-021-00736-x

Liu, Y., & Rice, J. R. (2007). Spontaneous and triggered aseismic deformation transients in a subduction fault model. *Journal of Geophysical Research: Solid Earth*, *112*(B9). https://doi.org/10.1029/2007JB004930

Luo, H., & Wang, K. (2021). Postseismic geodetic signature of cold forearc mantle in subduction zones. *Nature Geoscience*, *14*(2), 104–109. https://doi.org/10.1038/s41561-020-00679-9

Luo, Y., & Liu, Z. (2021). Fault zone heterogeneities explain depth-dependent pattern and evolution of slow earthquakes in Cascadia. *Nature Communications*, *12*(1), 1959. https://doi.org/10.1038/s41467-021-22232-x

Marone, C. (1998). LABORATORY-DERIVED FRICTION LAWS AND THEIR APPLICATION TO SEISMIC FAULTING. *Annual Review of Earth and Planetary Sciences*, *26*(1), 643–696. https://doi.org/10.1146/annurev.earth.26.1.643

Marone, C., Raleigh, C. B., & Scholz, C. H. (1990). Frictional behavior and constitutive modeling of simulated fault gouge. *Journal of Geophysical Research: Solid Earth*, *95*(B5), 7007–7025. https://doi.org/10.1029/JB095iB05p07007

Massonnet, D., Thatcher, W., & Vadon, H. (1996). Detection of postseismic fault-zone collapse following the Landers earthquake. *Nature*, *382*(6592), 612–616. https://doi.org/10.1038/382612a0

Masuti, S., Barbot, S. D., Karato, S., Feng, L., & Banerjee, P. (2016). Upper-mantle water stratification inferred from observations of the 2012 Indian Ocean earthquake. *Nature*, *538*(7625), 373–377. https://doi.org/10.1038/nature19783

McKenzie, D. P., & Parker, R. L. (1967). The North Pacific: an Example of Tectonics on a Sphere. *Nature*, *216*(5122), 1276–1280. https://doi.org/10.1038/2161276a0

Menant, A., Angiboust, S., & Gerya, T. (2019). Stress-driven fluid flow controls long-term megathrust strength and deep accretionary dynamics. *Scientific Reports*, *9*(1), 9714. https://doi.org/10.1038/s41598-019-46191-y

Moernaut, J., Van Daele, M., Fontijn, K., Heirman, K., Kempf, P., Pino, M., et al. (2018). Larger earthquakes recur more periodically: New insights in the megathrust earthquake cycle from lacustrine turbidite records in south-central Chile. *Earth and Planetary Science Letters*, *481*, 9–19. https://doi.org/10.1016/j.epsl.2017.10.016

Molina, D., Tassara, A., Abarca, R., Melnick, D., & Madella, A. (2021). Frictional Segmentation of the Chilean Megathrust From a Multivariate Analysis of Geophysical, Geological, and Geodetic Data. *Journal of Geophysical Research: Solid Earth*, *126*(6). https://doi.org/10.1029/2020JB020647

Moore, D. E., & Lockner, D. A. (2008). Talc friction in the temperature range 25°–400 °C: Relevance for Fault-Zone Weakening. *Tectonophysics*, *449*(1–4), 120–132. https://doi.org/10.1016/j.tecto.2007.11.039

Moore, D. E., & Lockner, D. A. (2011). Frictional strengths of talc-serpentine and talc-quartz mixtures. *Journal of Geophysical Research: Solid Earth*, *116*(B1), 1403. https://doi.org/10.1029/2010JB007881

Moreno, M., Melnick, D., Rosenau, M., Bolte, J., Klotz, J., Echtler, H., et al. (2011). Heterogeneous plate locking in the South–Central Chile subduction zone: Building up the next great earthquake. *Earth and Planetary Science Letters*, *305*(3–4), 413–424. https://doi.org/10.1016/j.epsl.2011.03.025

Moreno, M., Haberland, C., Oncken, O., Rietbrock, A., Angiboust, S., & Heidbach, O. (2014). Locking of the Chile subduction zone controlled by fluid pressure before the 2010 earthquake. *Nature Geoscience*, *7*(4), 292–296. https://doi.org/10.1038/ngeo2102

Moreno, M., Li, S., Melnick, D., Bedford, J. R., Baez, J. C., Motagh, M., et al. (2018). Chilean megathrust earthquake recurrence linked to frictional contrast at depth. *Nature Geoscience*, *11*(4), 285–290. https://doi.org/10.1038/s41561-018-0089-5

Muto, J., Moore, J. D. P., Barbot, S., Iinuma, T., Ohta, Y., & Iwamori, H. (2019). Coupled afterslip and transient mantle flow after the 2011 Tohoku earthquake. *Science Advances*, *5*(9). https://doi.org/10.1126/SCIADV.AAW1164/SUPPL_FILE/AAW1164_SM.PDF

Okazaki, K., & Katayama, I. (2015). Slow stick slip of antigorite serpentinite under hydrothermal conditions as a possible mechanism for slow earthquakes. *Geophysical Research Letters*, *42*(4), 1099–1104. https://doi.org/10.1002/2014GL062735

Quiero, F., Tassara, A., Iaffaldano, G., & Rabbia, O. (2022). Growth of Neogene Andes linked to changes in plate convergence using high-resolution kinematic models. *Nature Communications*, *13*(1), 1339. https://doi.org/10.1038/s41467-022-29055-4

Rice, J. R. (1993). Spatio-temporal complexity of slip on a fault. *Journal of Geophysical Research: Solid Earth*, *98*(B6), 9885–9907. https://doi.org/10.1029/93JB00191

Rubin, A. M., & Ampuero, J. -P. (2005). Earthquake nucleation on (aging) rate and state faults. *Journal of Geophysical Research: Solid Earth*, *110*(B11). https://doi.org/10.1029/2005JB003686

Ruina, A. (1983). Slip instability and state variable friction laws. *Journal of Geophysical Research: Solid Earth*, *88*(B12), 10359–10370. https://doi.org/10.1029/JB088iB12p10359

Ruiz, S., & Madariaga, R. (2018). Historical and recent large megathrust earthquakes in Chile. *Tectonophysics*, *733*, 37–56. https://doi.org/10.1016/j.tecto.2018.01.015

Saffer, D. M., & Marone, C. (2003). Comparison of smectite- and illite-rich gouge frictional properties: application to the updip limit of the seismogenic zone along subduction megathrusts. *Earth and Planetary Science Letters*, *215*(1–2), 219–235. https://doi.org/10.1016/S0012-821X(03)00424-2

Saffer, D. M., & Tobin, H. J. (2011). Hydrogeology and Mechanics of Subduction Zone Forearcs: Fluid Flow and Pore Pressure. *Annual Review of Earth and Planetary Sciences*, *39*(1), 157–186. https://doi.org/10.1146/annurev-earth-040610-133408

Saffer, D. M., & Wallace, L. M. (2015). The frictional, hydrologic, metamorphic and thermal habitat of shallow slow earthquakes. *Nature Geoscience*, *8*(8), 594–600. https://doi.org/10.1038/ngeo2490

Saito, T., & Noda, A. (2023). Mechanically Coupled Areas on the Plate Interface in the Kanto Region, Central Japan, Generating Great Earthquakes and Slow-Slip Events. *Bulletin of the Seismological Society of America*, *113*(5), 1842–1855. https://doi.org/10.1785/0120230073

Sawai, M., Niemeijer, A. R., Plümper, O., Hirose, T., & Spiers, C. J. (2016). Nucleation of frictional instability caused by fluid pressurization in subducted blueschist. *Geophysical Research Letters*, *43*(6), 2543–2551. https://doi.org/10.1002/2015GL067569

Sawai, M., Niemeijer, A. R., Hirose, T., & Spiers, C. J. (2017). Frictional properties of JFAST core samples and implications for slow earthquakes at the Tohoku subduction zone. *Geophysical Research Letters*, *44*(17), 8822–8831. https://doi.org/10.1002/2017GL073460

Scholz, C. H. (1998). Earthquakes and friction laws. *Nature*, *391*(6662), 37–42. https://doi.org/10.1038/34097

Scholz, C. H., & Campos, J. (2012). The seismic coupling of subduction zones revisited. *Journal of Geophysical Research: Solid Earth*, *117*(B5). https://doi.org/10.1029/2011JB009003

Schurr, B., Asch, G., Rosenau, M., Wang, R., Oncken, O., Barrientos, S., et al. (2012). The 2007 M7.7 Tocopilla northern Chile earthquake sequence: Implications for along-strike and downdip rupture segmentation and megathrust frictional behavior. *Journal of Geophysical Research: Solid Earth*, *117*(B5). https://doi.org/10.1029/2011JB009030

Schurr, B., Moreno, M., Tréhu, A. M., Bedford, J., Kummerow, J., Li, S., & Oncken, O. (2020). Forming a Mogi Doughnut in the Years Prior to and Immediately Before the 2014 *M* 8.1 Iquique, Northern Chile, Earthquake. *Geophysical Research Letters*, *47*(16). https://doi.org/10.1029/2020GL088351

Seton, M., Müller, R. D., Zahirovic, S., Williams, S., Wright, N. M., Cannon, J., et al. (2020). A Global Data Set of Present-Day Oceanic Crustal Age and Seafloor Spreading Parameters. *Geochemistry, Geophysics, Geosystems*, *21*(10). https://doi.org/10.1029/2020GC009214

Shi, Q., Barbot, S., Wei, S., Tapponnier, P., Matsuzawa, T., & Shibazaki, B. (2020). Structural control and system-level behavior of the seismic cycle at the Nankai Trough. *Earth, Planets and Space*, *72*(1), 27. https://doi.org/10.1186/s40623-020-1145-0

Shirzaei, M., Bürgmann, R., Oncken, O., Walter, T. R., Victor, P., & Ewiak, O. (2012). Response of forearc crustal faults to the megathrust earthquake cycle: InSAR evidence from Mejillones Peninsula, Northern Chile. *Earth and Planetary Science Letters*, *333–334*, 157–164. https://doi.org/10.1016/j.epsl.2012.04.001

Soto, H., Sippl, C., Schurr, B., Kummerow, J., Asch, G., Tilmann, F., et al. (2019). Probing the Northern Chile Megathrust With Seismicity: The 2014 M8.1 Iquique Earthquake Sequence. *Journal of Geophysical Research: Solid Earth*, *124*(12), 12935–12954. https://doi.org/10.1029/2019JB017794

Spinelli, G. A., Wada, I., He, J., & Perry, M. (2016). The thermal effect of fluid circulation in the subducting crust on slab melting in the Chile subduction zone. *Earth and Planetary Science Letters*, *434*, 101–111. https://doi.org/10.1016/j.epsl.2015.11.031

Straume, E. O., Gaina, C., Medvedev, S., Hochmuth, K., Gohl, K., Whittaker, J. M., et al. (2019). GlobSed: Updated Total Sediment Thickness in the World's Oceans. *Geochemistry, Geophysics, Geosystems*, *20*(4), 1756–1772. https://doi.org/10.1029/2018GC008115

Syracuse, E. M., van Keken, P. E., & Abers, G. A. (2010). The global range of subduction zone thermal models. *Physics of the Earth and Planetary Interiors*, *183*(1–2), 73–90. https://doi.org/10.1016/j.pepi.2010.02.004

Takahashi, M., Uehara, S.-I., Mizoguchi, K., Shimizu, I., Okazaki, K., & Masuda, K. (2011). On the transient response of serpentine (antigorite) gouge to stepwise changes in slip velocity under high-temperature conditions. *Journal of Geophysical Research*, *116*(B10), B10405. https://doi.org/10.1029/2010JB008062

Tassara, A. (2010). Control of forearc density structure on megathrust shear strength along the Chilean subduction zone. *Tectonophysics*, *495*(1–2), 34–47. https://doi.org/10.1016/j.tecto.2010.06.004

Tassara, A., & Echaurren, A. (2012). Anatomy of the Andean subduction zone: three-dimensional density model upgraded and compared against global-scale models. *Geophysical Journal International*, *189*(1), 161–168. https://doi.org/10.1111/j.1365-246X.2012.05397.x

Tassara, A., Götze, H., Schmidt, S., & Hackney, R. (2006). Three-dimensional density model of the Nazca plate and the Andean continental margin. *Journal of Geophysical Research: Solid Earth*, *111*(B9). https://doi.org/10.1029/2005JB003976

Tembe, S., Lockner, D. A., & Wong, T. (2010). Effect of clay content and mineralogy on frictional sliding behavior of simulated gouges: Binary and ternary mixtures of quartz, illite, and montmorillonite. *Journal of Geophysical Research: Solid Earth*, *115*(B3). https://doi.org/10.1029/2009JB006383

Tong, X., & Lavier, L. L. (2018). Simulation of slip transients and earthquakes in finite thickness shear zones with a plastic formulation. *Nature Communications*, *9*(1), 3893. https://doi.org/10.1038/s41467-018-06390-z

Veedu, D. M., & Barbot, S. (2016). The Parkfield tremors reveal slow and fast ruptures on the same asperity. *Nature*, *532*(7599), 361–365. https://doi.org/10.1038/nature17190

Vigny, C., & Klein, E. (2022). The 1877 megathrust earthquake of North Chile two times smaller than thought? A review of ancient articles. *Journal of South American Earth Sciences*, *117*, 103878. https://doi.org/10.1016/j.jsames.2022.103878

Völker, D., Grevemeyer, I., Stipp, M., Wang, K., & He, J. (2011). Thermal control of the seismogenic zone of southern central Chile. *Journal of Geophysical Research*, *116*(B10), B10305. https://doi.org/10.1029/2011JB008247

Wada, I., Wang, K., He, J., & Hyndman, R. D. (2008). Weakening of the subduction interface and its effects on surface heat flow, slab dehydration, and mantle wedge serpentinization. *Journal of Geophysical Research: Solid Earth*, *113*(B4). https://doi.org/10.1029/2007JB005190

Wallace, L. M. (2020). Slow Slip Events in New Zealand. *Annual Review of Earth and Planetary Sciences*, *48*(1), 175–203. https://doi.org/10.1146/annurev-earth-071719-055104

Wang, K., & Hu, Y. (2006). Accretionary prisms in subduction earthquake cycles: The theory of dynamic Coulomb wedge. *Journal of Geophysical Research: Solid Earth*, *111*(B6). https://doi.org/10.1029/2005JB004094

Wang, K., Hu, Y., Bevis, M., Kendrick, E., Smalley, R., Vargas, R. B., & Lauría, E. (2007). Crustal motion in the zone of the 1960 Chile earthquake: Detangling earthquake-cycle deformation and forearc-sliver translation. *Geochemistry, Geophysics, Geosystems*, *8*(10). https://doi.org/10.1029/2007GC001721

Wang, K., Brown, L., Hu, Y., Yoshida, K., He, J., & Sun, T. (2019). Stable Forearc Stressed by a Weak Megathrust: Mechanical and Geodynamic Implications of Stress Changes Caused by the M = 9 Tohoku-Oki Earthquake. *Journal of Geophysical Research: Solid Earth*, *124*(6), 6179–6194. https://doi.org/10.1029/2018JB017043

Wils, K., Van Daele, M., Kissel, C., Moernaut, J., Schmidt, S., Siani, G., & Lastras, G. (2020). Seismo-Turbidites in Aysén Fjord (Southern Chile) Reveal a Complex Pattern of Rupture Modes Along the 1960 Megathrust Earthquake Segment. *Journal of Geophysical Research: Solid Earth*, *125*(9). https://doi.org/10.1029/2020JB019405

Wilson, C. R., Spiegelman, M., van Keken, P. E., & Hacker, B. R. (2014). Fluid flow in subduction zones: The role of solid rheology and compaction pressure. *Earth and Planetary Science Letters*, *401*, 261–274. https://doi.org/10.1016/j.epsl.2014.05.052

7.2 References of Chapter 2 (Main article)

1. Lay, T. et al. Depth-varying rupture properties of subduction zone megathrust faults. J Geophys Res Solid Earth 117, (2012).

2. Scholz, C. H. Earthquakes and friction laws. Nature 391, 37–42 (1998).

3. Saffer, D. M. & Tobin, H. J. Hydrogeology and Mechanics of Subduction Zone Forearcs: Fluid Flow and Pore Pressure. Annu Rev Earth Planet Sci 39, 157–186 (2011).

4. Qiu, Q. & Barbot, S. Tsunami excitation in the outer wedge of global subduction zones. Earth-Science Reviews vol. 230 Preprint at https://doi.org/10.1016/j.earscirev.2022.104054 (2022).

5. Barbot, S. Frictional and structural controls of seismic super-cycles at the Japan trench. Earth, Planets and Space 72, (2020).

6. Lay, T. The surge of great earthquakes from 2004 to 2014. Earth Planet Sci Lett 409, 133–146 (2015).

7. Ye, L., Lay, T., Kanamori, H., Yamazaki, Y. & Cheung, K. F. The 22 July 2020 MW 7.8 Shumagin seismic gap earthquake: Partial rupture of a weakly coupled megathrust. Earth Planet Sci Lett 562, (2021).

8. Moreno, M. S., Bolte, J., Klotz, J. & Melnick, D. Impact of megathrust geometry on inversion of coseismic slip from geodetic data: Application to the 1960 Chile earthquake. Geophys Res Lett 36, 16310 (2009).

9. Moreno, M. et al. Chilean megathrust earthquake recurrence linked to frictional contrast at depth. Nat Geosci 11, 285–290 (2018).

10. Maldonado, V., Contreras, M. & Melnick, D. A comprehensive database of active and potentially-active continental faults in Chile at 1:25,000 scale. Sci Data 8, (2021).

11. Melnick, D., Bookhagen, B., Strecker, M. R. & Echtler, H. P. Segmentation of megathrust rupture zones from fore-arc deformation patterns over hundreds to millions of years, Arauco peninsula, Chile. J Geophys Res Solid Earth 114, 1407 (2009).

12. Plafker, G. & Savage, J. C. Mechanism of the Chilean Earthquakes of May 21 and 22, 1960. Geol Soc Am Bull 81, 1001–1030 (1970).

13. Ruiz, S. et al. Reawakening of large earthquakes in south central Chile: The 2016 Mw 7.6 Chiloé event. Geophys Res Lett 44, 6633–6640 (2017).

14. Quiero, F., Tassara, A., Iaffaldano, G. & Rabbia, O. Growth of Neogene Andes linked to changes in plate convergence using high-resolution kinematic models. Nat Commun 13, 1339 (2022).

15. Hayes, G. P. et al. Slab2, a comprehensive subduction zone geometry model. Science (1979) 362, 58–61 (2018).

16. Lange, D. et al. Seismicity and geometry of the south Chilean subduction zone (41.5°S-43.5°S): Implications for controlling parameters. Geophys Res Lett 34, (2007).

17. Bohm, M. et al. The Southern Andes between 36° and 40°S latitude: seismicity and average seismic velocities. Tectonophysics 356, 275–289 (2002).

18. Contreras-Reyes, E., Flueh, E. R. & Grevemeyer, I. Tectonic control on sediment accretion and subduction off south central Chile: Implications for coseismic rupture processes of the 1960 and 2010 megathrust earthquakes. Tectonics 29, (2010).

19. Bangs, N. L. et al. Basal Accretion Along the South Central Chilean Margin and Its Relationship to Great Earthquakes. J Geophys Res Solid Earth 125, (2020).

20. Maksymowicz, A., Montecinos-Cuadros, D., Díaz, D., Segovia, M. J. & Reyes, T. Forearc density structure of the overriding plate in the northern area of the giant 1960 Valdivia earthquake. Solid Earth 13, 117–136 (2022).

21. Maksymowicz, A. et al. Deep Structure of the Continental Plate in the South-Central Chilean Margin: Metamorphic Wedge and Implications for Megathrust Earthquakes. J Geophys Res Solid Earth 126, (2021).

22. Scherwath, M. et al. Deep lithospheric structures along the southern central Chile margin from wide-angle P-wave modelling. Geophys J Int 179, 579–600 (2009).

23. Tassara, A. & Echaurren, A. Anatomy of the Andean subduction zone: three-dimensional density model upgraded and compared against global-scale models. Geophys J Int 189, 161–168 (2012).

24. Qiu, Q. & Barbot, S. Tsunami excitation in the outer wedge of global subduction zones. doi:10.1016/j.earscirev.2022.104054.

25. Krawczyk, C. M. et al. Geophysical Signatures and Active Tectonics at the South-Central Chilean Margin. in The Andes 171–192 (Springer Berlin Heidelberg). doi:10.1007/978-3-540-48684-8_8.

26. Dzierma, Y. et al. Seismic velocity structure of the slab and continental plate in the region of the 1960 Valdivia (Chile) slip maximum — Insights into fluid release and plate coupling. doi:10.1016/j.epsl.2012.02.006.

27. Echaurren, A. et al. Fore-to-retroarc crustal structure of the north Patagonian margin: How is shortening distributed in Andean-type orogens? Glob Planet Change 209, (2022).

28. Cembrano, J., Hervé, F. & Lavenu, A. The Liquiñe Ofqui fault zone: a long-lived intra-arc fault system in southern Chile. Tectonophysics 259, 55–66 (1996).

29. Barbot, S. Slow-slip, slow earthquakes, period-two cycles, full and partial ruptures, and deterministic chaos in a single asperity fault. Tectonophysics 768, (2019).

30. Kukowski, N. & Oncken, O. Subduction Erosion — the “Normal” Mode of Fore-Arc Material Transfer along the Chilean Margin? in The Andes 217–236 (Springer Berlin Heidelberg). doi:10.1007/978-3-540-48684-8_10.

31. Genge, M. C. et al. The role of slab geometry in the exhumation of cordilleran-type orogens and their forelands: Insights from northern Patagonia. GSA Bulletin 133, 2535–2548 (2021).

32. Adriasola, A. C., Thomson, S. N., Brix, M. R., Hervé, F. & Stöckhert, B. Postmagmatic cooling and late Cenozoic denudation of the North Patagonian Batholith in the Los Lagos region of Chile, 41°-42°15′S. International Journal of Earth Sciences 95, 504–528 (2006).

33. Melnick, D. & Echtler, H. P. Inversion of forearc basins in south-central Chile caused by rapid glacial age trench fill. Geology 34, 709–712 (2006).

34. Tembe, S., A. Lockner, D. & Wong, T. Effect of clay content and mineralogy on frictional sliding behavior of simulated gouges: Binary and ternary mixtures of quartz, illite, and montmorillonite. doi:10.1029/2009jb006383.

35. den Hartog, S. A. M., Niemeijer, A. R. & Spiers, C. J. New constraints on megathrust slip stability under subduction zone P–T conditions. doi:10.1016/j.epsl.2012.08.022.

36. Behrmann, J. H. & Kopf, A. Balance of tectonically accreted and subducted sediment at the Chile triple junction. International Journal of Earth Sciences 90, 753–768 (2001).

37. Liu, Y. & R. Rice, J. Slow slip predictions based on granite and gabbro friction data compared to GPS measurements in northern Cascadia. doi:10.1029/2008jb006142.

38. Melnick, D. et al. Back to full interseismic plate locking decades after the giant 1960 Chile earthquake. Nature Communications 2018 9:1 9, 1–10 (2018).

39. Angiboust, S., Wolf, S., Burov, E., Agard, P. & Yamato, P. Effect of fluid circulation on subduction interface tectonic processes: Insights from thermo-mechanical numerical modelling. doi:10.1016/j.epsl.2012.09.012.

40. Okazaki, K. & Katayama, I. Slow stick slip of antigorite serpentinite under hydrothermal conditions as a possible mechanism for slow earthquakes. Geophys Res Lett 42, 1099–1104 (2015).

41. Takahashi, M. et al. On the transient response of serpentine (antigorite) gouge to stepwise changes in slip velocity under high-temperature conditions. doi:10.1029/2010jb008062.

42. E. Moore, D. & A. Lockner, D. Frictional strengths of talc-serpentine and talc-quartz mixtures. doi:10.1029/2010jb007881.

43. Schwartz, S. et al. Pressure–temperature estimates of the lizardite/antigorite transition in high pressure serpentinites. doi:10.1016/j.lithos.2012.11.023.

44. Saffer, D. M. & Wallace, L. M. The frictional, hydrologic, metamorphic and thermal habitat of shallow slow earthquakes. Nat Geosci 8, 594–600 (2015).

45. Araya, R., Cárcamo, C., Poza, A. & Poza, A. H. A stabilized finite element method for the Stokes-Temperature coupled problem. (2022).

46. Spinelli, G. A., Wada, I., He, J. & Perry, M. The thermal effect of fluid circulation in the subducting crust on slab melting in the Chile subduction zone. Earth Planet Sci Lett 434, 101–111 (2016).

47. Völker, D., Grevemeyer, I., Stipp, M., Wang, K. & He, J. Thermal control of the seismogenic zone of southern central Chile. J Geophys Res Solid Earth 116, (2011).

48. Karato, S. I. & Jung, H. Effects of pressure on high-temperature dislocation creep in olivine. https://doi.org/10.1080/0141861021000025829 83, 401–414 (2010).

49. Masuti, S., Barbot, S. D., Karato, S. I., Feng, L. & Banerjee, P. Upper-mantle water stratification inferred from observations of the 2012 Indian Ocean earthquake. Nature 2016 538:7625 538, 373–377 (2016).

50. Wada, I., Rychert, C. A. & Wang, K. Sharp thermal transition in the forearc mantle wedge as a consequence of nonlinear mantle wedge flow. Geophys Res Lett 38, n/a-n/a (2011).

51. Erickson, B. A. et al. The community code verification exercise for Simulating Sequences of Earthquakes and Aseismic Slip (SEAS). Seismological Research Letters 91, 874–890 (2020).

52. Weiss, J. R. et al. Illuminating subduction zone rheological properties in the wake of a giant earthquake. Sci Adv 5, (2019).

53. Luo, H. & Wang, K. Postseismic geodetic signature of cold forearc mantle in subduction zones. Nat Geosci 14, 104–109 (2021).

54. Garrett, E., Brader, M., Melnick, D., Bedford, J. & Aedo, D. First field evidence of coseismic land-level change associated with the 25 december 2016 M w 7.6 Chiloé, Chile, earthquake. Bulletin of the Seismological Society of America 109, 87–98 (2019).

55. Wils, K. et al. Seismo-Turbidites in Aysén Fjord (Southern Chile) Reveal a Complex Pattern of Rupture Modes Along the 1960 Megathrust Earthquake Segment. J Geophys Res Solid Earth 125, (2020).

56. Moernaut, J. et al. Larger earthquakes recur more periodically: New insights in the megathrust earthquake cycle from lacustrine turbidite records in south-central Chile. Earth Planet Sci Lett 481, 9–19 (2018).

57. Cifuentes, I. L. The 1960 Chilean earthquakes. J Geophys Res Solid Earth 94, 665–680 (1989).

58. Krawczyk, C. Amphibious seismic survey images plate interface at 1960 Chile Earthquake. Eos, Transactions American Geophysical Union 84, 301–305 (2003).

59. Ho, T. C., Satake, K., Watada, S. & Fujii, Y. Source Estimate for the 1960 Chile Earthquake From Joint Inversion of Geodetic and Transoceanic Tsunami Data. J Geophys Res Solid Earth 124, 2812–2828 (2019).

60. Hocking, E. P., Garrett, E., Aedo, D., Carvajal, M. & Melnick, D. Geological evidence of an unreported historical Chilean tsunami reveals more frequent inundation. Commun Earth Environ 2, (2021).

61. Kempf, P., Moernaut, J. & De Batist, M. Bimodal recurrence pattern of tsunamis in south-central Chile: A statistical exploration of paleotsunami data. Seismological Research Letters 90, 194–202 (2019).

62. Luo, H. & Wang, K. Finding Simplicity in the Complexity of Postseismic Coastal Uplift and Subsidence Following Great Subduction Earthquakes. doi:10.1029/2022jb024471.

63. Becerra-Carreño, V., Crempien, J. G. F., Benavente, R. & Moreno, M. Plate-Locking, Uncertainty Estimation and Spatial Correlations Revealed With a Bayesian Model Selection Method: Application to the Central Chile Subduction Zone. J Geophys Res Solid Earth 127, e2021JB023939 (2022).

64. Yu, H., Liu, Y., Yang, H. & Ning, J. Modeling earthquake sequences along the Manila subduction zone: Effects of three-dimensional fault geometry. Tectonophysics 733, 73–84 (2018).

65. B. Condit, C., E. Guevara, V., R. Delph, J. & E. French, M. Slab dehydration in warm subduction zones at depths of episodic slip and tremor. doi:10.1016/j.epsl.2020.116601.

66. Hernández-Uribe, D., Palin, R. M., Cone, K. A. & Cao, W. Petrological Implications of Seafloor Hydrothermal Alteration of Subducted Mid-Ocean Ridge Basalt. Journal of Petrology 61, (2021).

7.3 References of Chapter 2 (Methods)

67. Lapusta, N. & Rice, J. R. Nucleation and early seismic propagation of small and large events in a crustal earthquake model. J Geophys Res Solid Earth 108, (2003).

68. Barbot, S. Modulation of fault strength during the seismic cycle by grain-size evolution around contact junctions. Tectonophysics 765, 129–145 (2019).

69. Dieterich, J. H. & Kilgore, B. Implications of fault constitutive properties for earthquake prediction. Proceedings of the National Academy of Sciences 93, 3787–3794 (1996).

70. Dieterich, J. H. Modeling of rock friction 1. Experimental results and constitutive equations. in Journal of Geophysical Research: Solid Earth vol. 84 2161–2168 (Blackwell Publishing Ltd, 1979).

71. Marone, C. Laboratory-derived friction laws and their application to seismic faulting. Annu Rev Earth Planet Sci 26, 643–696 (1998).

72. Bürgmann, R. The geophysics, geology and mechanics of slow fault slip. Earth Planet Sci Lett 495, 112–134 (2018).

73. Kozdon, J. E. & Dunham, E. M. Rupture to the Trench: Dynamic rupture simulations of the 11 march 2011 Tohoku earthquake. Bulletin of the Seismological Society of America 103, 1275–1289 (2013).

74. Rubin, A. M. & Ampuero, J. P. Earthquake nucleation on (aging) rate and state faults. J Geophys Res Solid Earth 110, 1–24 (2005).

75. Hirth, G. & Kohlstedt, D. Rheology of the Upper Mantle and the Mantle Wedge: A View from the Experimentalists. Geophysical Monograph Series 138, 83–105 (2004).

76. Barbot, S., Moore, J. D. P. & Lambert, V. Displacement and stress associated with distributed anelastic deformation in a half-space. Bulletin of the Seismological Society of America 107, 821–855 (2017).

77. Muto, J. et al. Coupled afterslip and transient mantle flow after the 2011 Tohoku earthquake. Sci Adv 5, (2019).

78. Marotta, G. S. A., França, G. S., Galera Monico, J. F., Fuck, R. A. & Oswaldo de Araújo Filho, J. Strain rate of the South American lithospheric plate by SIRGAS-CON geodetic observations. J South Am Earth Sci 47, 136–141 (2013).

79. van Keken, P. E. et al. A community benchmark for subduction zone modeling. Physics of the Earth and Planetary Interiors 171, 187–197 (2008).

80. Peacock, S. M. & Wang, K. On the Stability of Talc in Subduction Zones: A Possible Control on the Maximum Depth of Decoupling Between the Subducting Plate and Mantle Wedge. Geophys Res Lett 48, (2021).

81. Turcotte, D. & Schubert, G. Geodynamics. (Cambridge University Press, 2014). doi:10.1017/CBO9780511843877.

82. Tebbens, S. F. & Cande, S. C. Southeast Pacific tectonic evolution from Early Oligocene to Present. J Geophys Res Solid Earth 102, 12061–12084 (1997).

83. Tassara, A. Control of forearc density structure on megathrust shear strength along the Chilean subduction zone. Tectonophysics 495, 34–47 (2010).

7.3 References of Chapter 3

Adam, J., & Reuther, C.-D. (2000). Crustal dynamics and active fault mechanics during subduction erosion. Application of frictional wedge analysis on to the North Chilean Forearc. *Tectonophysics*, *321*(3), 297–325. https://doi.org/10.1016/S0040-1951(00)00074-3

Araya, R., Cárcamo, C., & Poza, A. H. (2023). A stabilized finite element method for the Stokes–Temperature coupled problem. *Applied Numerical Mathematics*, *187*, 24–49. https://doi.org/10.1016/j.apnum.2023.02.002

Barbot, S. (2018). Asthenosphere flow modulated by megathrust earthquake cycles. Geophysical Research Letters, 45, 6018–6031. https://doi.org/10.1029/2018GL078197

Barbot, S. (2019a). Modulation of fault strength during the seismic cycle by grain-size evolution around contact junctions. *Tectonophysics*, *765*, 129–145. https://doi.org/10.1016/j.tecto.2019.05.004

Barbot, S. (2019b). Slow-slip, slow earthquakes, period-two cycles, full and partial ruptures, and deterministic chaos in a single asperity fault. *Tectonophysics*, *768*, 228171. https://doi.org/10.1016/j.tecto.2019.228171

Barbot, S. (2020). Frictional and structural controls of seismic super-cycles at the Japan trench. *Earth, Planets and Space*, *72*(1), 63. https://doi.org/10.1186/s40623-020-01185-3

Barker, D. H. N., R. Sutherland, S. Henrys, and S. Bannister (2009), Geometry of the Hikurangi subduction thrust and upper plate, North Island, New Zealand, Geochem. Geophys. Geosyst., 10, Q02007, doi:10.1029/2008GC002153.

Barnes P. M., Nicol A., Harrison T.; Late Cenozoic evolution and earthquake potential of an active listric thrust complex above the Hikurangi subduction zone, New Zealand. GSA Bulletin 2002;; 114 (11): 1379–1405. doi: https://doi.org/10.1130/0016-7606(2002)114<1379:LCEAEP>2.0.CO;2

Bedford, J., Moreno, M., Schurr, B., Bartsch, M., & Oncken, O. (2015). Investigating the final seismic swarm before the Iquique-Pisagua 2014 M_w 8.1 by comparison of continuous GPS and seismic foreshock data. *Geophysical Research Letters*, *42*(10), 3820–3828. https://doi.org/10.1002/2015GL063953

Brengman, C. M. J., Barnhart, W. D., Mankin, E. H., & Miller, C. N. (2019). Earthquake-Scaling Relationships from Geodetically Derived Slip Distributions. *Bulletin of the Seismological Society of America*, *109*(5), 1701–1715. https://doi.org/10.1785/0120190048

Carretier, S., Tolorza, V., Regard, V., Aguilar, G., Bermúdez, M. A., Martinod, J., et al. (2018). Review of erosion dynamics along the major N-S climatic gradient in Chile and perspectives. *Geomorphology*, *300*, 45–68. https://doi.org/10.1016/j.geomorph.2017.10.016

Comte, D., Carrizo, D., Roecker, S., Ortega-Culaciati, F., & Peyrat, S. (2016). Three-dimensional elastic wave speeds in the northern Chile subduction zone: variations in hydration in the supraslab mantle. *Geophysical Journal International*, *207*(2), 1080–1105. https://doi.org/10.1093/gji/ggw318

Dielforder, A., Vollstaedt, H., Vennemann, T., Berger, A., & Herwegh, M. (2015). Linking megathrust earthquakes to brittle deformation in a fossil accretionary complex. *Nature Communications*, *6*(1), 7504. https://doi.org/10.1038/ncomms8504

van Dinther, Y., Mai, P. M., Dalguer, L. A., & Gerya, T. V. (2014). Modeling the seismic cycle in subduction zones: The role and spatiotemporal occurrence of off-megathrust earthquakes. *Geophysical Research Letters*, *41*(4), 1194–1201. https://doi.org/10.1002/2013GL058886

Duputel, Z., J. Jiang, R. Jolivet, M. Simons, L. Rivera, J.-P. Ampuero, B. Riel, S. E. Owen, A. W. Moore, S. V. Samsonov, et al. (2015), The Iquique earthquake sequence of April 2014: Bayesian modeling accounting for prediction uncertainty, Geophys. Res. Lett., 42, 7949–7957, doi:10.1002/2015GL065402.

Farías, M., D. Comte, S. Roecker, D. Carrizo, and M. Pardo (2011), Crustal extensional faulting triggered by the 2010 Chilean earthquake: The Pichilemu Seismic Sequence, Tectonics, 30, TC6010, doi:10.1029/2011TC002888.

Fukushima, Y., Toda, S., Miura, S. et al. Extremely early recurrence of intraplate fault rupture following the Tohoku-Oki earthquake. Nature Geosci 11, 777–781 (2018). https://doi.org/10.1038/s41561-018-0201-x

Geersen, J., Ranero, C. R., Klaucke, I., Behrmann, J. H., Kopp, H., Tréhu, A. M., et al. (2018). Active Tectonics of the North Chilean Marine Forearc and Adjacent Oceanic Nazca Plate. *Tectonics*, *37*(11), 4194–4211. https://doi.org/10.1029/2018TC005087

Giambiagi, L., Tassara, A., Echaurren, A., Julve, J., Quiroga, R., Barrionuevo, M., et al.. (2022). Crustal anatomy and evolution of a subduction-related orogenic system: Insights from the Southern Central Andes (22-35 S). Earth-Science Reviews, 232, 104138. https://doi.org/10.1016/j.earscirev.2022.104138

González, G., Salazar, P., Loveless, J. P., Allmendinger, R. W., Aron, F., & Shrivastava, M. (2015). Upper plate reverse fault reactivation and the unclamping of the megathrust during the 2014 northern Chile earthquake sequence. *Geology*, *43*(8), 671–674. https://doi.org/10.1130/G36703.1

Hananto, N. D., Leclerc, F., Li, L., Etchebes, M., Carton, H., Tapponnier, P., et al. (2020). Tsunami earthquakes: Vertical pop-up expulsion at the forefront of subduction megathrust. *Earth and Planetary Science Letters*, 538, 116197.

Hayes, G. P., Moore, G. L., Portner, D. E., Hearne, M., Flamme, H., Furtney, M., & Smoczyk, G. M. (2018). Slab2, a comprehensive subduction zone geometry model. *Science*, *362*(6410), 58–61. https://doi.org/10.1126/SCIENCE.AAT4723/SUPPL_FILE/AAT4723-HAYES-SM.PDF

Hayes, G., Herman, M., Barnhart, W. et al. Continuing megathrust earthquake potential in Chile after the 2014 Iquique earthquake. Nature 512, 295–298 (2014). https://doi.org/10.1038/nature13677

Herman, M. W., Furlong, K. P., & Benz, H. M. (2023). Substantial upper plate faulting above a shallow subduction megathrust earthquake: Mechanics and implications of the surface faulting during the 2016 Kaikoura, New Zealand, earthquake. Tectonics, 42, e2022TC007645. https://doi.org/10.1029/2022TC007645

Herman, M. W., Furlong, K. P., Hayes, G. P., & Benz, H. M. (2016). Foreshock triggering of the 1 April 2014 Mw 8.2 Iquique, Chile, earthquake. *Earth and Planetary Science Letters*, *447*, 119–129. https://doi.org/10.1016/j.epsl.2016.04.020

Herrera, M. T., Crempien, J. G. F., & Cembrano, J. (2023). Complex Crustal Deformation Controlled by the 3D Geometry of the Chile Subduction Zone. *Bulletin of the Seismological Society of America*, *113*(6), 2479–2491. https://doi.org/10.1785/0120230062

von Huene, R., Miller, J.J., Klaeschen, D., Dartnell, P. (2016). A Possible Source Mechanism of the 1946 Unimak Alaska Far-Field Tsunami: Uplift of the Mid-Slope Terrace Above a Splay Fault Zone. In: Geist, E.L., Fritz, H.M., Rabinovich, A.B., Tanioka, Y. (eds) Global Tsunami Science: Past and Future, Volume I. Pageoph Topical Volumes. Birkhäuser, Cham. https://doi.org/10.1007/978-3-319-55480-8_26

Jolivet R., Simons, M., Duputel, Z., Olive, J.-A., Bhat, H. S., & Bletery, Q. (2020). Interseismic loading of subduction megathrust drives long-term uplift in Northern Chile. Geophysical Research Letters, 47, e2019GL085377. https://doi.org/10.1029/2019GL085377

Julve, J., Barbot, S., Moreno, M. et al. Recurrence time and size of Chilean earthquakes influenced by geological structure. Nat. Geosci. 17, 79–87 (2024). https://doi.org/10.1038/s41561-023-01327-8

Kamei, R., Pratt, R. G., & Tsuji, T. (2012). Waveform tomography imaging of a megasplay fault system in the seismogenic Nankai subduction zone. Earth and Planetary Science Letters, 317, 343-353.

Kato, A., Sakai, S. & Obara, K. A normal-faulting seismic sequence triggered by the 2011 off the Pacific coast of Tohoku Earthquake: Wholesale stress regime changes in the upper plate. Earth Planet Sp 63, 745–748 (2011). https://doi.org/10.5047/eps.2011.06.014

Kober, F., Ivy-Ochs, S., Schlunegger, F., Baur, H., Kubik, P. W., & Wieler, R. (2007). Denudation rates and a topography-driven rainfall threshold in northern Chile: Multiple cosmogenic nuclide data and sediment yield budgets. *Geomorphology*, *83*(1–2), 97–120. https://doi.org/10.1016/j.geomorph.2006.06.029

Kodaira, S., Nakamura, Y., Yamamoto, Y., Obana, K., Fujie, G., No, T., et al. (2017). Depth-varying structural characters in the rupture zone of the 2011 Tohoku-oki earthquake. Geosphere, 13(5), 1408-1424.

Kopp, H., Hindle, D., Klaeschen, D., Oncken, O., Reichert, C., & Scholl, D. (2009). Anatomy of the western Java plate interface from depth-migrated seismic images. *Earth and Planetary Science Letters*, 288(3-4), 399-407.

Lapusta, N., & Liu, Y. (2009). Three-dimensional boundary integral modeling of spontaneous earthquake sequences and aseismic slip. *Journal of Geophysical Research: Solid Earth*, *114*(B9). https://doi.org/10.1029/2008JB005934

Li, D., and Y. Liu (2017), Modeling slow-slip segmentation in Cascadia subduction zone constrained by tremor locations and gravity anomalies, J. Geophys. Res. Solid Earth, 122, 3138–3157, doi:10.1002/2016JB013778.

Li, D., and Y. Liu (2016), Spatiotemporal evolution of slow slip events in a nonplanar fault model for northern Cascadia subduction zone, J. Geophys. Res. Solid Earth, 121, 6828–6845, doi:10.1002/2016JB012857.

Li, S., Moreno, M., Bedford, J., Rosenau, M., & Oncken, O. (2015). Revisiting viscoelastic effects on interseismic deformation and locking degree: A case study of the Peru-North Chile subduction

zone. *Journal of Geophysical Research: Solid Earth*, *120*(6), 4522–4538. https://doi.org/10.1002/2015JB011903

Lüschen, E., Müller, C., Kopp, H., Engels, M., Lutz, R., Planert, L., et al. (2011). Structure, evolution and tectonic activity of the eastern Sunda forearc, Indonesia, from marine seismic investigations. Tectonophysics, 508(1-4), 6-21. https://doi.org/10.1016/j.tecto.2010.06.008

Maksymowicz, A., Ruiz, J., Vera, E., Contreras-Reyes, E., Ruiz, S., Arraigada, C., et al. (2018). Heterogeneous structure of the Northern Chile marine forearc and its implications for megathrust earthquakes. *Geophysical Journal International*, *215*(2), 1080–1097. https://doi.org/10.1093/gji/ggy325

Meng, L., Huang, H., Bürgmann, R., Ampuero, J. P., & Strader, A. (2015). Dual megathrust slip behaviors of the 2014 Iquique earthquake sequence. *Earth and Planetary Science Letters*, *411*, 177–187. https://doi.org/10.1016/j.epsl.2014.11.041

Melnick, D., B. Bookhagen, M. R. Strecker, and H. P. Echtler (2009), Segmentation of megathrust rupture zones from fore-arc deformation patterns over hundreds to millions of years, Arauco peninsula, Chile, J. Geophys. Res., 114, B01407, doi:10.1029/2008JB005788.

Melnick D., Moreno M., Motagh M., Cisternas M., Wesson R. L.; Splay fault slip during the Mw 8.8 2010 Maule Chile earthquake. Geology 2012;; 40 (3): 251–254. doi: https://doi.org/10.1130/G32712.1

Miller, J. J., von Huene, R. E., & Ryan, H. F. (2014). The 1946 Unimak Tsunami Earthquake Area: Revised tectonic structure in reprocessed seismic images and a suspect near field tsunami source (No. 2014-1024). *US Geological Survey*.

Moore, D. E., & Lockner, D. A. (2011). Frictional strengths of talc-serpentine and talc-quartz mixtures. *Journal of Geophysical Research*, *116*(B1), B01403. https://doi.org/10.1029/2010JB007881

Moore, G. F., Bangs, N. L., Taira, A., Kuramoto, S., Pangborn, E., & Tobin, H. J. (2007). Three-Dimensional Splay Fault Geometry and Implications for Tsunami Generation. *Science*, *318*(5853), 1128–1131. https://doi.org/10.1126/science.1147195

Nie, S., & Barbot, S. (2022). Rupture styles linked to recurrence patterns in seismic cycles with a compliant fault zone. Earth and Planetary Science Letters, 591, 117593. https://doi.org/10.1016/j.epsl.2022.117593

Okazaki, K., & Katayama, I. (2015). Slow stick slip of antigorite serpentinite under hydrothermal conditions as a possible mechanism for slow earthquakes. *Geophysical Research Letters*, *42*(4), 1099–1104. https://doi.org/10.1002/2014GL062735

Oncken, O., Angiboust, S., & Dresen, G. (2021). Slow slip in subduction zones: Reconciling deformation fabrics with instrumental observations and laboratory results. *Geosphere*, *18*(1), 104–129. https://doi.org/10.1130/GES02382.1

Park, J.-O., T. Tsuru, N. Takahashi, T. Hori, S. Kodaira, A. Nakanishi, S. Miura, and Y. Kaneda, A deep strong reflector in the Nankai accretionary wedge from multichannel seismic data: Implications for underplating and interseismic shear stress release, J. Geophys. Res., 107(B4), doi:10.1029/2001JB000262, 2002.

Petersen, F., Lange, D., Ma, B., Grevemeyer, I., Geersen, J., Klaeschen, D., et al. (2021). Relationship Between Subduction Erosion and the Up-Dip Limit of the 2014 Mw 8.1 Iquique Earthquake. *Geophysical Research Letters*, *48*(9). https://doi.org/10.1029/2020GL092207

Qiu, Q., & Barbot, S. (2022). Tsunami excitation in the outer wedge of global subduction zones. Earth-science reviews, 230, 104054. https://doi.org/10.1016/j.earscirev.2022.104054

Rubin, A. M., & Ampuero, J. -P. (2005). Earthquake nucleation on (aging) rate and state faults. *Journal of Geophysical Research: Solid Earth*, *110*(B11). https://doi.org/10.1029/2005JB003686

Ruiz, S., Metois, M., Fuenzalida, A., Ruiz, J., Leyton, F., Grandin, R., et al. (2014). Intense foreshocks and a slow slip event preceded the 2014 Iquique M_w 8.1 earthquake. *Science*, *345*(6201), 1165–1169. https://doi.org/10.1126/science.1256074

Sallarès, V., & Ranero, C. R. (2005). Structure and tectonics of the erosional convergent margin off Antofagasta, north Chile (23°30′S). *Journal of Geophysical Research: Solid Earth*, *110*(B6). https://doi.org/10.1029/2004JB003418

Sathiakumar, S., Barbot S., & Hubbard J. The role of fault structural evolution on long-term slip rates and seismic cycles in the Himalayan orogenic wedge. *Earth and Planetary Science Letters* 630 (2024): 118599. https://doi.org/10.1016/j.epsl.2024.118599

Sathiakumar, S., Barbot, S., & Hubbard, J. (2020). Earthquake cycles in fault-bend folds. Journal of Geophysical Research: Solid Earth, 125, e2019JB018557. https://doi.org/10.1029/2019JB018557

Schurr, B., Moreno, M., Tréhu, A. M., Bedford, J., Kummerow, J., Li, S., & Oncken, O. (2020). Forming a Mogi Doughnut in the Years Prior to and Immediately Before the 2014 *M* 8.1 Iquique, Northern Chile, Earthquake. *Geophysical Research Letters*, *47*(16). https://doi.org/10.1029/2020GL088351

Schurr, Bernd, Asch, G., Hainzl, S., Bedford, J., Hoechner, A., Palo, M., et al. (2014). Gradual unlocking of plate boundary controlled initiation of the 2014 Iquique earthquake. *Nature*, *512*(7514), 299–302. https://doi.org/10.1038/nature13681

Shi, P., Wei, M., & Barbot, S. (2022). Contribution of viscoelastic stress to the synchronization of earthquake cycles on oceanic transform faults. Journal of Geophysical Research: Solid Earth, 127, e2022JB024069. https://doi.org/10.1029/2022JB024069

Singh, S., Carton, H., Tapponnier, P. et al. Seismic evidence for broken oceanic crust in the 2004 Sumatra earthquake epicentral region. Nature Geosci 1, 777–781 (2008). https://doi.org/10.1038/ngeo336

Sippl, C., Schurr, B., Münchmeyer, J., Barrientos, S., & Oncken, O. (2023). The Northern Chile forearc constrained by 15 years of permanent seismic monitoring. Journal of South American Earth Sciences, 104326. https://doi.org/10.1016/j.jsames.2023.104326

Socquet, A., Valdes, J. P., Jara, J., Cotton, F., Walpersdorf, A., Cotte, N., et al. (2017). An 8 month slow slip event triggers progressive nucleation of the 2014 Chile megathrust. *Geophysical Research Letters*, *44*(9), 4046–4053. https://doi.org/10.1002/2017GL073023

Soto, H., Sippl, C., Schurr, B., Kummerow, J., Asch, G., Tilmann, F., et al. (2019). Probing the Northern Chile Megathrust With Seismicity: The 2014 M8.1 Iquique Earthquake Sequence. *Journal of Geophysical Research: Solid Earth*, *124*(12), 12935–12954. https://doi.org/10.1029/2019JB017794

Storch, I., Buske, S., Victor, P., & Oncken, O. (2021). Seismic images of the Northern Chilean subduction zone at 19°40′S, prior to the 2014 Iquique earthquake. *Geophysical Journal International*, *225*(2), 1048–1061. https://doi.org/10.1093/gji/ggab035

Takahashi, M., Uehara, S.-I., Mizoguchi, K., Shimizu, I., Okazaki, K., & Masuda, K. (2011). On the transient response of serpentine (antigorite) gouge to stepwise changes in slip velocity under high-temperature conditions. *Journal of Geophysical Research*, *116*(B10), B10405. https://doi.org/10.1029/2010JB008062

Tassara, A., & Echaurren, A. (2012). Anatomy of the Andean subduction zone: three-dimensional density model upgraded and compared against global-scale models. *Geophysical Journal International*, *189*(1), 161–168. https://doi.org/10.1111/j.1365-246X.2012.05397.x

van Zelst, I., Rannabauer, L., Gabriel, A.-A., & van Dinther, Y. (2022). Earthquake rupture on multiple splay faults and its effect on tsunamis. Journal of Geophysical Research: Solid Earth, 127, e2022JB024300. https://doi.org/10.1029/2022JB024300

Vigny, C., & Klein, E. (2022). The 1877 megathrust earthquake of North Chile two times smaller than thought? A review of ancient articles. *Journal of South American Earth Sciences*, *117*, 103878. https://doi.org/10.1016/j.jsames.2022.103878

Wang, K., & Hu, Y. (2006). Accretionary prisms in subduction earthquake cycles: The theory of dynamic Coulomb wedge. *Journal of Geophysical Research: Solid Earth*, *111*(B6). https://doi.org/10.1029/2005JB004094

Wang, K., Brown, L., Hu, Y., Yoshida, K., He, J., & Sun, T. (2019). Stable Forearc Stressed by a Weak Megathrust: Mechanical and Geodynamic Implications of Stress Changes Caused by the M = 9 Tohoku-Oki Earthquake. *Journal of Geophysical Research: Solid Earth*, *124*(6), 6179–6194. https://doi.org/10.1029/2018JB017043

Watt J. T., Brothers D. S.; Systematic characterization of morphotectonic variability along the Cascadia convergent margin: Implications for shallow megathrust behavior and tsunami hazards. Geosphere 2020;; 17 (1): 95–117. doi: https://doi.org/10.1130/GES02178.1

Wilson, K., Berryman, K., Litchfield, N., & Little, T. (2006). A revision of mid-late Holocene marine terrace distribution and chronology at the Pakarae River mouth, North Island, New Zealand. New Zealand Journal of Geology and Geophysics, 49(4), 477–489. https://doi.org/10.1080/00288306.2006.9515182

Zhang, L., He, C., Liu, Y., & Lin, J. (2017). Frictional properties of the South China Sea oceanic basalt and implications for strength of the Manila subduction seismogenic zone. *Marine Geology*, *394*, 16–29. https://doi.org/10.1016/j.margeo.2017.05.006

Zhu, J., Sun, Z., Kopp, H. et al. Segmentation of the Manila subduction system from migrated multichannel seismics and wedge taper analysis. *Mar Geophys Res* 34, 379–391 (2013). https://doi.org/10.1007/s11001-013-9175-7